ILLINOIS CENTER FOR TRANSPORTATION

CIVIL ENGINEERING STUDIES
Illinois Center for Transportation Series No. 21-031
UILU-ENG-2021-2031
ISSN: 0197-9191

Early-age Properties of High-volume Fly Ash Concrete Mixes for Pavement: Volume 2

Prepared By
Aniruddha Baral
Jeffery R. Roesler
Junryu Fu
University of Illinois at Urbana-Champaign

Research Report No. FHWA-ICT-21-026

A report of the findings of

ICT PROJECT R27-180
Concrete Pavement Mixtures with High Supplementary Cementitious Materials (SCM) Content

https://doi.org/10.36501/0197-9191/21-031

Illinois Center for Transportation

September 2021

TECHNICAL REPORT DOCUMENTATION PAGE

1. Report No. FHWA-ICT-21-026	**2. Government Accession No.** N/A	**3. Recipient's Catalog No.** N/A
4. Title and Subtitle Early-age Properties of High-volume Fly Ash Concrete Mixes for Pavement: Volume 2		**5. Report Date** September 2021 **6. Performing Organization Code** N/A
7. Authors Aniruddha Baral (https://orcid.org/0000-0003-0810-5475), Jeffery R. Roesler (https://orcid.org/0000-0001-6194-269X), Junryu Fu		**8. Performing Organization Report No.** ICT-21-031 UILU-2021-2031
9. Performing Organization Name and Address Illinois Center for Transportation Department of Civil and Environmental Engineering University of Illinois at Urbana-Champaign 205 North Mathews Avenue, MC-250 Urbana, IL 61801		**10. Work Unit No.** N/A **11. Contract or Grant No.** R27-180
12. Sponsoring Agency Name and Address Illinois Department of Transportation (SPR) Bureau of Research 126 East Ash Street Springfield, IL 62704		**13. Type of Report and Period Covered** Final Report 10/1/17–9/30/21 **14. Sponsoring Agency Code**

15. Supplementary Notes
Conducted in cooperation with the U.S. Department of Transportation, Federal Highway Administration.
https://doi.org/10.36501/0197-9191/21-031

16. Abstract
High-volume fly ash concrete (HVFAC) is more cost-efficient, sustainable, and durable than conventional concrete. This report presents a state-of-the-art review of HVFAC properties and different fly ash characterization methods. The main challenges identified for HVFAC for pavements are its early-age properties such as air entrainment, setting time, and strength gain, which are the focus of this research. Five fly ash sources in Illinois have been repeatedly characterized through x-ray diffraction, x-ray fluorescence, and laser diffraction over time. The fly ash oxide compositions from the same source but different quarterly samples were overall consistent with most variations observed in SO_3 and MgO content. The minerals present in various fly ash sources were similar over multiple quarters, with the mineral content varying. The types of carbon present in the fly ash were also characterized through x-ray photoelectron spectroscopy, loss on ignition, and foam index tests. A new computer vision–based digital foam index test was developed to automatically capture and quantify a video of the foam layer for better operator and laboratory reliability. The heat of hydration and setting times of HVFAC mixes for different cement and fly ash sources as well as chemical admixtures were investigated using an isothermal calorimeter. Class C HVFAC mixes had a higher sulfate imbalance than Class F mixes. The addition of chemical admixtures (both PCE- and lignosulfonate-based) delayed the hydration, with the delay higher for the PCE-based admixture. Both micro- and nano-limestone replacement were successful in accelerating the setting times, with nano-limestone being more effective than micro-limestone. A field test section constructed of HVFAC showed the feasibility and importance of using the noncontact ultrasound device to measure the final setting time as well as determine the saw-cutting time. Moreover, field implementation of the maturity method based on wireless thermal sensors demonstrated its viability for early opening strength, and only a few sensors with pavement depth are needed to estimate the field maturity.

17. Key Words Fly Ash, Limestone, Maturity, Noncontact Ultrasound, Setting Time, Hydration, Foam Index, Concrete	**18. Distribution Statement** No restrictions. This document is available through the National Technical Information Service, Springfield, VA 22161.

19. Security Classif. (of this report) Unclassified	**20. Security Classif. (of this page)** Unclassified	**21. No. of Pages** 70 + appendices	**22. Price** N/A

ACKNOWLEDGMENT, DISCLAIMER, MANUFACTURERS' NAMES

This publication is based on the results of **ICT-R27-180: Concrete Pavement Mixtures with High Supplementary Cementitious Materials (SCM) Content**. ICT-R27-180 was conducted in cooperation with the Illinois Center for Transportation; the Illinois Department of Transportation; and the U.S. Department of Transportation, Federal Highway Administration.

The authors acknowledge Sachindra Dahal for his help with the noncontact ultrasound device and the thermal sensor field placement. The authors also thank Dr. Quang Tran for his guidance in using the noncontact ultrasound device as well as the computer vision technique used for the foam index test. Collaboration with Prof. Tyler Ley was essential and very helpful to this research effort and outcomes.

Members of the Technical Review Panel were the following:

- James Krstulovich, TRP Chair, Illinois Department of Transportation
- Dennis Bachman, Federal Highway Administration
- Darrin Davis, Illinois Department of Transportation
- Kevin Finn, Illinois Department of Transportation
- Dan Gancarz, Applied Research Associates, Inc.
- Stephen Jones, Illinois Department of Transportation
- Kelly Morse, Illinois Department of Transportation
- Chad Pink, Illinois Department of Transportation
- Megan Swanson, Illinois Department of Transportation
- Dan Tobias, Illinois Department of Transportation
- Melinda Winkelman, Illinois Department of Transportation
- Steve Worsfold, Illinois Department of Transportation

EXECUTIVE SUMMARY

Replacing cement with supplementary cementitious materials (SCMs) reduces the concrete material unit cost and increases durability. Illinois Department of Transportation (IDOT) currently allows a maximum 25%, 30%, and 35% cement replacement with Class F fly ash, Class C fly ash, and ground granulated blast furnace slag (GGBFS), respectively. With more emphasis on further improving the sustainability of concrete, there is discussion on even higher replacement levels of cement with fly ash or slag, which are the most common replacements in Illinois.

An extensive literature review of both high-volume fly ash and slag concretes was conducted with the aim to increase the permissible GGBFS and fly ash replacement (by mass) in concrete to 50% and 40%, respectively. Several agencies such as the Federal Aviation Administration, US Army Corps, and California Department of Transportation already allow up to 50% cement replacement with slag. The primary focus of this study was moved to investigate high-volume fly ash concrete (HVFAC) for pavements. Existing literature demonstrated that a high rate of replacement by fly ash (40% to 65%) is possible while still meeting the long-term strength criteria. Although many advantages exist for higher volume fly ash concrete mixtures, early-age properties such as air content, setting times, and strength gain rates can be affected, which can limit the permissible replacement levels.

To solve the challenges associated with HVFAC pavements, this project focused on four major themes: 1) fly ash oxide and mineral characterization, 2) fly ash carbon characterization and development of methods for improving HVFA air entrainment and quality control, 3) effect of different mixture constituents and interactions on HVFAC hydration and setting time, and 4) tools for implementing HVFAC pavements in the field. The major findings from each of these four research tasks are detailed next.

Fly ash oxide and mineral characterization: Various fly ash sources in Illinois, sourced at different times, have been characterized through x-ray diffraction (XRD), x-ray fluorescence (XRF), and laser diffraction to evaluate the variability of ashes. Fly ash oxide compositions from the same source but different quarterly samples were overall consistent with most variations observed in SO_3 and MgO content. The minerals present in various fly ash sources were similar over multiple quarters; however, the amount of these minerals varied over time.

Fly ash carbon characterization and improving quality control test: Foam index, x-ray photoelectron spectroscopy (XPS), loss on ignition (LOI) tests were performed to characterize the carbon present in the fly ashes. The foam index of the different fly ash from Illinois varied over a wide range—from 1 μL air-entraining agent (AEA) per gm fly ash (0.015 oz AEA/lb fly ash) to 10 μL AEA per gm fly ash (0.15 oz AEA/lb fly ash). XPS was performed to evaluate different carbon chemical environments of five fly ash sources, and a positive correlation among LOI, foam index, and C-C, C-H species percentage was found. A new computer vision–based foam index test, the digital foam index test (D-FIT), was also developed, which can reduce the sources of error between labs and operators.

Effect of different mixture variables on HVFAC hydration and setting time: An isothermal calorimeter test method was used to evaluate the setting time and heat flow of HVFAC mixes. The

setting times of fly ashes from different quarters did not vary by more than 30 minutes. The addition of chemical admixture (both PCE- and lignosulfonate-based) delayed the hydration, but the delay was higher in mixes using PCE-based admixtures. To accelerate the setting times of HVFAC, micro- and nano-limestone replacement of cement was explored. Limestone replacement accelerated the setting times with nano-limestone being more effective than micro-limestone to accelerate the setting times. Five percent micro-limestone replacement accelerated setting times of HVFAC mixes with chemical admixtures by 2–3 hours. The setting time acceleration with 5% micro-limestone replacement was similar for Class F HVFAC mixes with PCE- and lignosulfonate-based admixtures. However, for Class C HVFAC mixes, the acceleration was much higher in PCE-based admixture mixes. Micro-limestone replacement at a relatively low rate can be a great large-scale implementable tool to accelerate the setting times without sacrificing long-term strength given the wide availability of limestone in the United States.

Tools for field implementation of HVFAC pavements: Because the major problems with HVFAC are delayed setting time and early age strength gain, methods to measure in-place setting time and compressive strength are extremely important for field implementation. In this project, we successfully implemented the maturity method for in-place strength prediction of HVFAC. The in-place compressive strength calculated using the maturity method also did not depend on the pavement depth from which the temperature data is collected and thus a limited number of wireless thermal sensors are needed on a project. A noncontact ultrasonic device was also employed to determine the final setting time of the HVFAC pavement. The final setting time can be used to estimate the time to initiate the saw cutting of the joints with limited joint raveling.

TABLE OF CONTENTS

LIST OF FIGURES

LIST OF TABLES

CHAPTER 1: INTRODUCTION

Replacing cement with supplementary cementitious materials (SCMs) has been practiced for decades, with the primary objectives being to reduce the concrete material unit cost and increase material durability. SCMs include multiple products such as fly ash, slag, calcined clay, and different natural pozzolans, but fly ash and slags are most used and will be investigated in this project. Illinois Department of Transportation (IDOT) currently allows a maximum 25%, 30%, and 35% cement replacement with Class F fly ash, Class C fly ash, and ground granulated blast furnace slag (GGBFS), respectively. Recently, improving the sustainability of concrete has encouraged discussion on even higher replacement levels of cement with SCMs.

Replacing cement with GGBFS up to 50% is currently allowed in multiple federal agencies. The Federal Aviation Administration (2018) allows 25%–55% replacement of cement with 100 or 120 grade GGBFS in P-501 Portland cement concrete (PCC) pavement. The US Army Corps allows up to 50% replacement of cement with GGBFS for cast-in-place concrete in severe exposure conditions with both freeze-thaw and deicing salt exposure (USACE 2019). California Department of Transportation (2013) currently allows up to 60% cement replacement with GGBFS but limits the replacement rate to 50% in projects with high strength requirements. ACI 301 and 318 committees on structural concrete allow up to 50% replacement in high exposure conditions. Some laboratory studies have shown that concrete with 50% GGBFS can have higher salt scaling than conventional concrete potentially due to its higher sorptivity or different carbonation mechanisms (Amini et al. 2019; Valenza and Scherer 2005), but field studies have shown that GGBFS concrete with curing compound application shows satisfactory salt-scaling performance (Boyd and Hooton 2007). As application up to 50% GGBFS is allowed by many agencies in the United States, the focus of this study was moved to investigate high-volume fly ash concrete (HVFAC).

Some of the specific performance benefits of partial replacement of cement with fly ash are mitigating the alkali-silica reaction (Detwiler 1997), decreasing ion permeability (Yurdakul et al. 2014), improving joint deterioration susceptibility (Farnam, Zhang, and Weiss 2017; Suraneni et al. 2017), and lowering the heat of hydration of mass concrete (Bamforth 1980). The Federal Highway Administration and several state transportation agencies (e.g., Caltrans, INDOT, etc.) have already initiated research on this topic (Nassif and Suksawang 2003; Tanikella and Olek 2017). Existing literature demonstrates that a high rate of replacement by fly ash (40% to 65%) is possible while still meeting the long-term strength criteria. Although many advantages exist for higher volume fly ash concrete mixtures, early-age properties such as air content, setting times, and strength gain rates can be affected (Taylor et al. 2006a), which can limit the permissible replacement levels.

The influence of fly ash on concrete's early-age properties depends on the chemical composition of the crystalline and amorphous phases, volume replacement level, and particle size. Restrictions on fly ash use based on broad oxide contents or arbitrary replacement levels can lead to missed opportunities, which can improve both the cost and durability of concrete pavements. Furthermore, the discussion of noncompliance fly ash applications in concrete is gaining attention in the United States (Wirth et al. 2019), with many agencies seeking solutions to reclaim old fly ash ponds and stockpiles that are contributing to downstream pollution or health risks. Duke Energy, one of the

largest global electric utility companies, was fined $100 million in 2015 for a coal ash spill in a North Carolina river (Chatterjee 2015). Duke Energy recently agreed to excavate 72.5 million metric tons of coal fly ash at six facilities, with the total closure cost of the Carolinas estimated to be $8–$9 billion (Duke Energy 2020). In comparison, the total coal fly ash market is less than $5 billion, which shows the tremendous opportunity in using fly ash in higher volume for concrete production.

With the urgency to apply higher replacement levels of fly ash in concrete pavements, rapid advanced characterization techniques of fly ash coupled with mineral and chemical admixtures can provide the appropriate testing protocols and mixture modifications to enable the use of HVFAC, i.e., cement replacement rates of 40% or higher. The use of HVFAC is particularly challenging in cold climates because of lower set times, lower strength gains, and a higher risk of plastic shrinkage. Additionally, the variability of fly ash obtained from the same source over time generally requires diligent quality control.

In order to tackle challenges with HVFAC pavements, this report mostly focuses on early-age properties. This report is divided into three major parts. Chapter 2 characterizes various fly ash sources in Illinois through XRD, XRF, and laser diffraction. Moreover, foam index, XPS, and LOI tests were performed to characterize the carbon present in the fly ash. Chapter 3 presents the results of the hydration mechanism of HVFAC using a calorimeter. Sulfate imbalance, the effect of different water reducers, and the effect of limestone addition are studied in this chapter. Chapter 4 examines the implementation of HVFAC pavement in the field using a test section and evaluates in-place strength gain estimation using the maturity method as well as setting time using a recently developed noncontact ultrasonic device. Moreover, a literature review on HVFAC concrete, data obtained from HVFAC trial batching, and cumulative heat flow data obtained from calorimeter experiments on HVFAC containing limestone are attached in the appendix. Finally, conclusions obtained from this research are discussed in Chapter 5.

CHAPTER 2: FLY ASH CHARACTERIZATION

Five fly ash samples obtained from different sources in the Midwest were characterized using different techniques. Particle size distribution was measured using laser diffraction and bulk oxide was measured using EDXRF. The minerals present in the fly ash were identified using XRD. The carbon present in the fly ash was characterized using both LOI and XPS. Finally, foam index test was performed on the fly ash samples. Results of the suite of fly ash characterization tests are presented in this chapter.

PARTICLE SIZE DISTRIBUTION

The particle size distribution of the fly ash samples was measured using a Mastersizer 3000 laser diffraction particle size analyzer. The fly ash particles need to be uniformly dispersed in a dispersing medium for an accurate particle size analysis using a laser diffraction particle size analyzer. Fly ash was added to approximately 30 mL (1.014 oz) of isopropanol and ultrasonicated at room temperature for 30 minutes. According to National Institute of Standards and Technology (NIST) report 7097 (Hackley et al. 2004), 5 minutes of ultrasonication is sufficient; however, it was ultrasonicated for 30 minutes to make sure the fly ash particles are separated. Next, part of the 30 mL (1.014 oz) solution was added to 580 mL (19.61 oz) of isopropanol till the obscuration level is 14% to 16%.

Mie scattering theory was used instead of Fraunhofer diffraction, as most of the particles were below 50 microns in size. Mie scattering requires three parameters of fly ash: density, absorption index, and refractive index. Density was measured according to ASTM C188. The refractive index was obtained from Figure 4 in Jewell and Rathbone (2009), which relates the CaO content in fly ash with the refractive index. The refractive index for blue light (470 nm) and red light (633 nm) was assumed to be equal. The absorption index was changed till the volume fraction measured by Mastersizer 3000 through Beer-Lambert's law is within 15% of the true volume fraction of fly ash in the sample. If the absorption index was at 0.01, then it was not further changed, as it does not change the particle size distribution significantly. Table 1 shows details of the fly ash used in the laser diffraction instrument.

Table 1. Parameters of the Fly Ash in the Laser Diffraction Experiment

Name of Fly Ash	Class of Fly Ash	Density (gm/cc)	Reflective Index	Volume Fraction in Sample (%)	Absorption Index
Fly Ash 1	C	2.74	1.66	0.012	0.01
Fly Ash 2	C	2.74	1.66	0.009	0.01
Fly Ash 3	C	2.47	1.65	0.010	0.01
Fly Ash 4	F	2.29	1.56	0.019	0.01
Fly Ash 5	C	2.44	1.65	0.012	0.01

The results were expressed both in terms of cumulative volume fraction and differential volume fraction percentage. As laser diffraction technique is a volumetric method, representation of the particle size distribution in terms of frequency is not preferred as it may increase the error, especially for small particles.

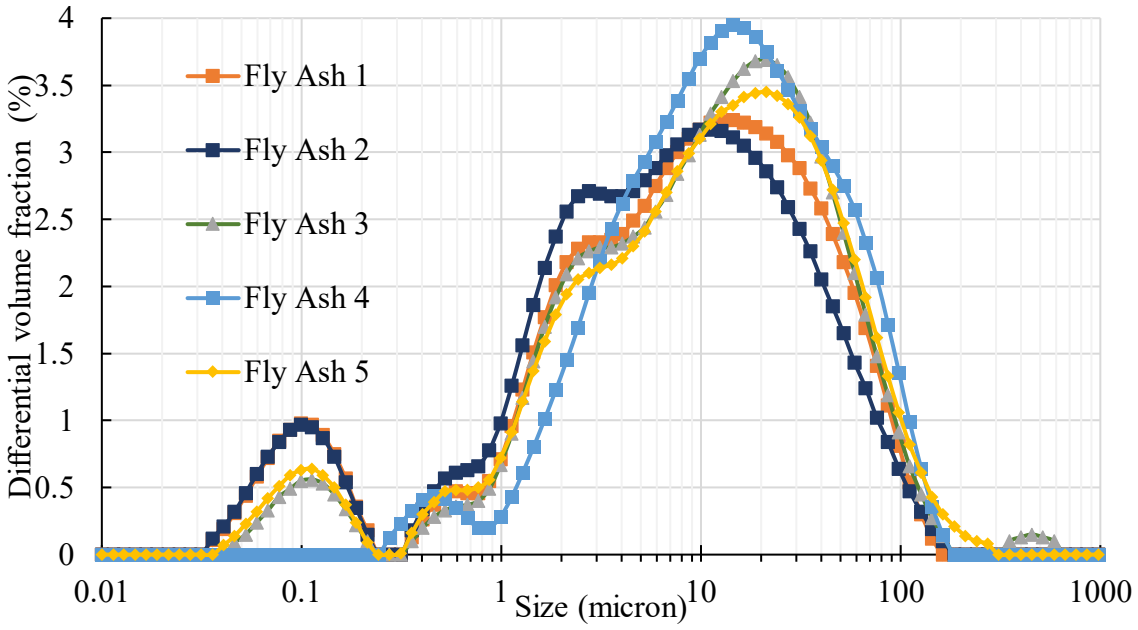

A. Differential volume fraction

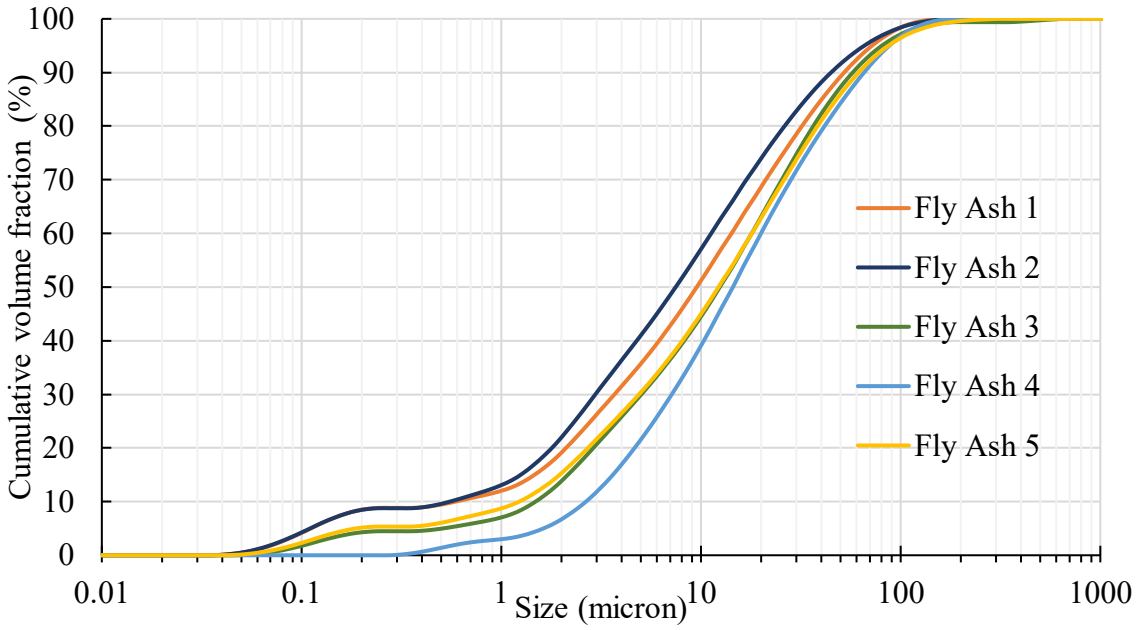

B. Cumulative volume fraction

Figure 1. Graphs. Differential volume fraction (a) and cumulative volume fraction (b) of the fly ash particle sizes obtained using a laser diffraction particle size analyzer.

All five fly ash sources had mostly particles with a diameter less than 100 micron. Among the five fly ash sources tested, Fly Ash 4 was the coarsest, as it had almost no particles below 0.2 micron diameter. Fly Ash 3 and Fly Ash 5 had very similar particle size distributions.

The differential volume fraction distribution was converted to a single number, called specific surface area (Klobes, Meyer, and Munro 2006), to understand how coarse/fine each fly ash was, as shown in Figure 2.

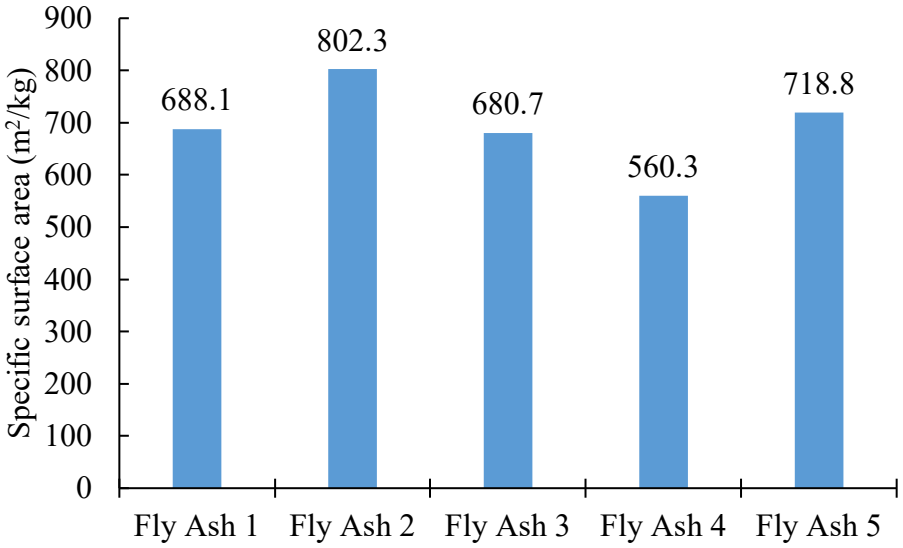

Figure 2. Graph. Specific surface area of the five fly ash sources.

OXIDE COMPOSITION

The oxide composition of the fly ash was measured using both EDXRF and XPS. As discussed previously, EDXRF provides the bulk elemental composition, whereas XPS measures the surface elemental composition.

EDXRF

The EDXRF of the fly ash samples was performed using a Shimadzu EDX-7000 in a helium environment in powder form without any sample preparation. This EDXRF system can detect atoms heavier than sodium. Table 2 shows the major bulk oxide compositions of the two different cement samples used in this study. Both Cement A and B had SO_3 higher than 3%, which is the maximum allowable SO_3 content per ASTM C150. Figure 3 shows the quarterly variations of oxide contents of four fly ash sources. For Fly Ash 1, the 2018 sample had significantly high MgO and CaO content and a low SiO_2 content compared to the other quarters. The SO_3 content also decreased over time for this ash. In terms of Fly Ash 2, the MgO and Fe_2O_3 content were significantly higher for the 2018 sample and the Q1 2019 sample, respectively. The SO_3 and MgO content of Fly Ash 3 increased over time significantly—the SO_3 content in the Q2 2019 sample was about double of that in the 2018 sample. Fly Ash 4 was a Class F ash, and it had a very consistent oxide content over two years of sample collection. This ash also had significantly higher K_2O content compared to other ashes. Overall, MgO, SO_3, and K_2O had higher coefficient of variations compared to the other oxides.

Table 2. Oxide Compositions (%) of Two Type I/II Cements

	Cement A	Cement B
SiO_2	19.61	20.36
CaO	64.97	64.37
Al_2O_3	3.75	3.76
Fe_2O_3	3.20	4.31
MgO	1.48	1.66
SO_3	5.30	4.17
TiO_2	0.29	0.30
K_2O	1.04	0.78
MnO	0.20	0.16

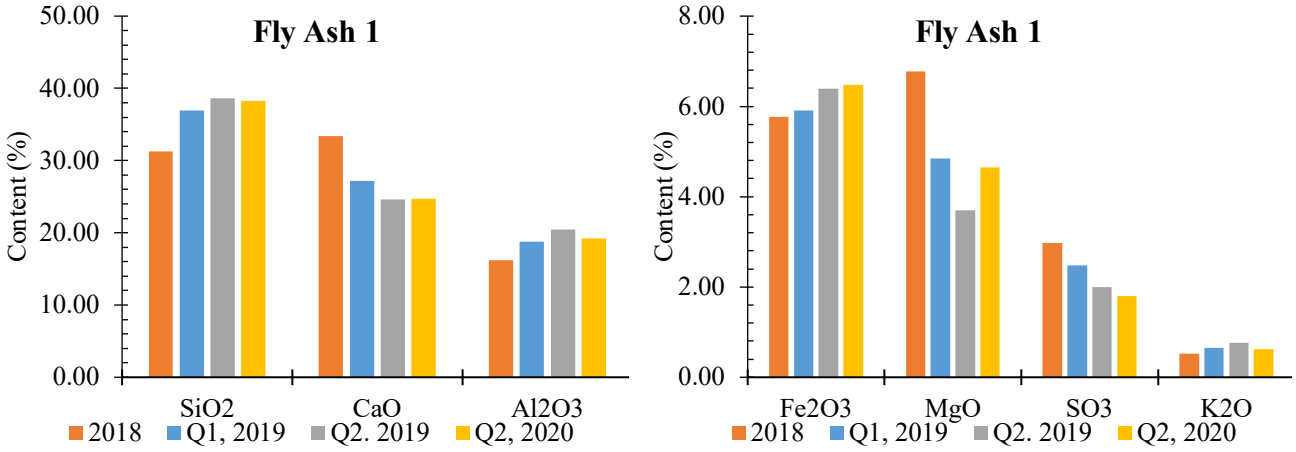

A. Fly Ash 1

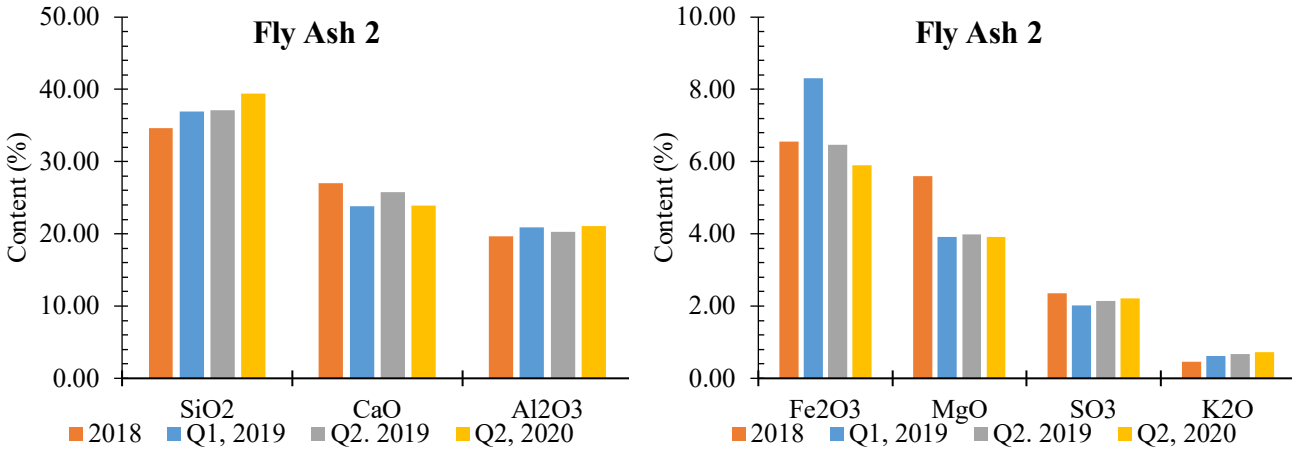

B. Fly Ash 2

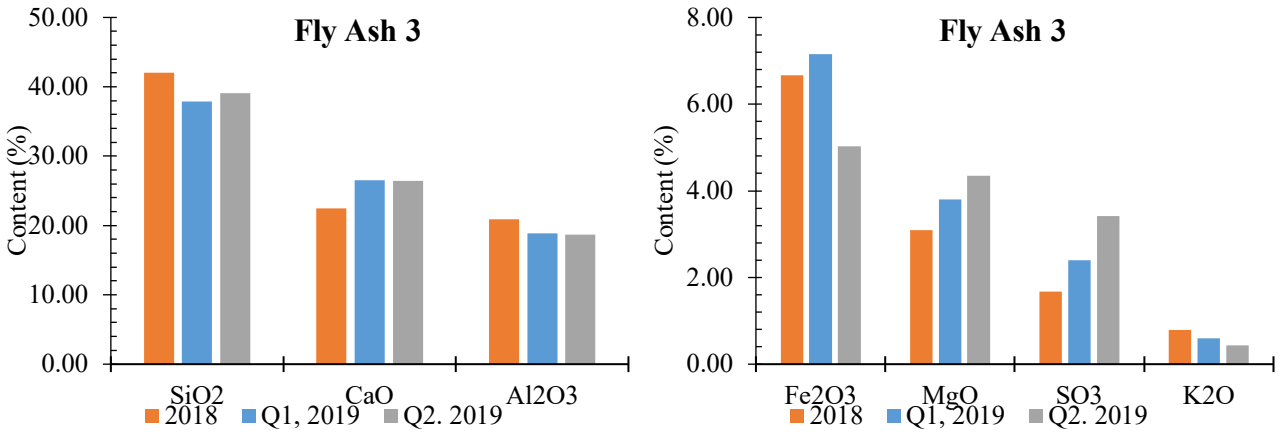

C. Fly Ash 3

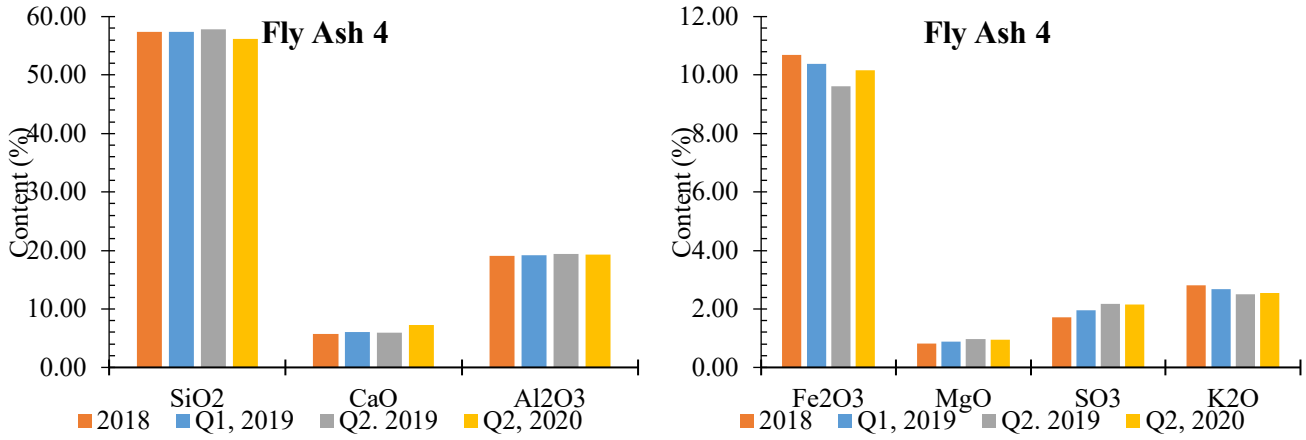

D. Fly Ash 4

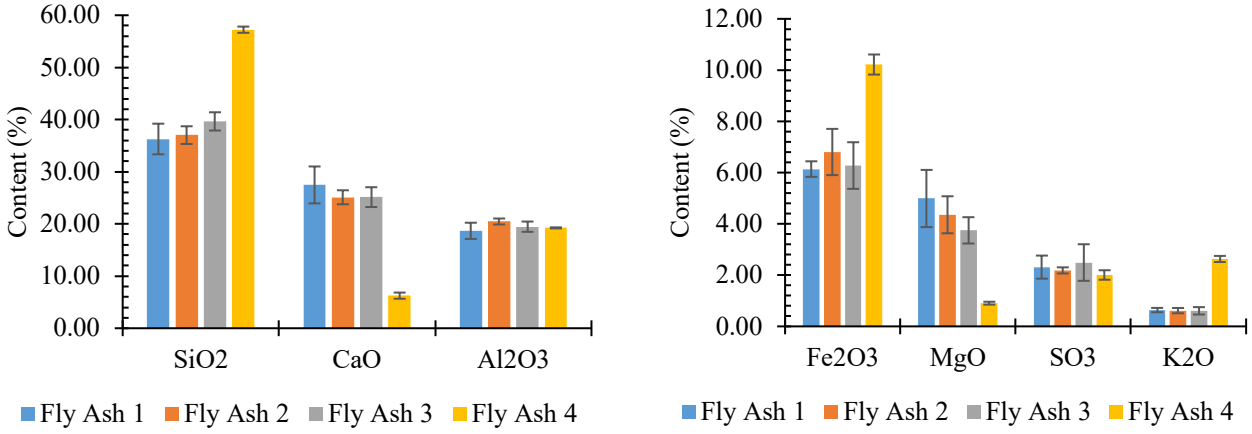

E. Mean composition and variation of quarterly samples

Figure 3. Graphs. Major oxide compositions of (a) Fly Ash 1, (b) Fly Ash 2, (c) Fly Ash 3, (d) Fly Ash 4, and (e) overall average over different quarterly samples (standard deviation = error bars).

XPS

The XPS spectrum of the fly ash samples was collected using a Kratos Axis Ultra machine with an aluminum source. The fly ash powder was put on a copper tape instead of a carbon tape, as fly ash contains carbon. The energy of the photoelectron was collected at an energy resolution of 1 eV and Scofield RSF (relative sensitivity factor) was used. Next, the data was fitted using a Monte-Carlo simulation, using CasaXPS software. Figure 4 presents a typical survey spectrum obtained using XPS. Table 3 shows the atomic concentrations observed in the fly ash samples. The atomic concentrations were then converted to oxide percentage (Table 4). The surface was more enriched in carbon, sodium, potassium, and sulfur and less enriched in calcium, silicon, and aluminum than the bulk.

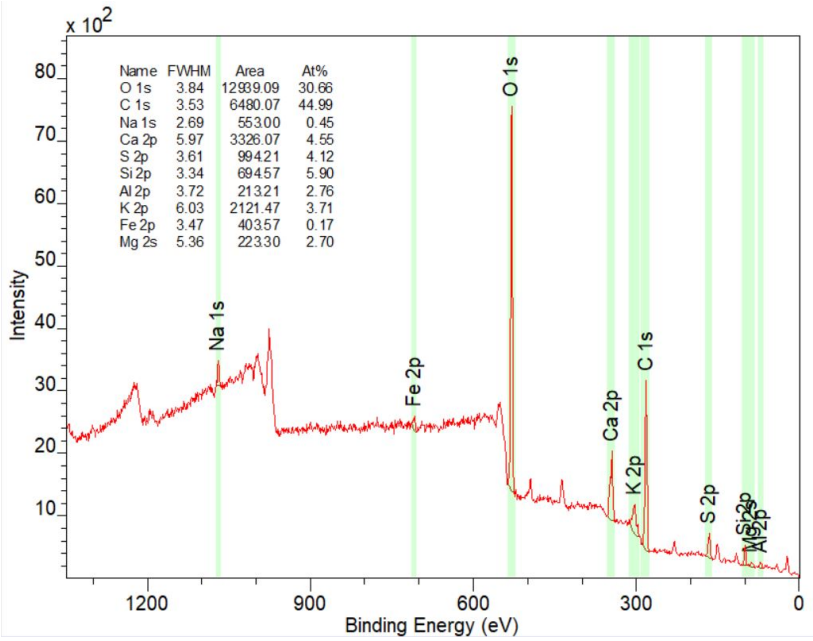

Figure 4. Graph. XPS survey spectrum and atomic concentration of Fly Ash 2.

Table 3. XPS Atom Concentration for the Fly Ash Samples

	Fly Ash 1	Fly Ash 2	Fly Ash 3	Fly Ash 4	Fly Ash 5
	Atom (%)				
O 1s	27.29	30.66	35.53	37.76	34.12
C 1s	49.29	44.99	37.88	38.09	38.83
Na 1s	0.92	0.45	1.57	0.79	1.15
Ca 2p	5.2	4.55	5.9	3.22	5.12
S 2p	3.76	4.12	4.23	5.61	6.94
Si 2p	4.69	5.9	5.72	9.0	6.37
Al 2p	2.33	2.76	3.19	3.19	1.37
K 2p	4.43	3.71	4.14	1.95	2.93
Fe 2p		0.17		0.39	
Mg 2s	2.1	2.70	1.85		3.18

Table 4. XPS Oxide Concentration (weight %) for the Fly Ash Samples

	Molecular Weight (g/mol)	Fly Ash 1	Fly Ash 2	Fly Ash 3	Fly Ash 4	Fly Ash 5
C	12.01	26.14	23.74	19.30	20.34	20.20
Na2O	61.98	2.52	1.23	4.13	2.18	3.09
CaO	56.07	12.89	11.22	14.05	8.03	12.45
SO3	80.07	13.31	14.51	14.38	19.98	24.09
SiO2	60.08	12.45	15.59	14.59	24.06	16.59
Al2O3	101.96	10.50	12.37	13.81	14.47	6.06
K2O	94.20	18.45	15.37	16.56	8.17	11.97
Fe2O3	159.69	0.00	1.19	0.00	2.77	0.00
MgO	40.30	3.74	4.79	3.17	0.00	5.56

MINERAL COMPOSITION

A Bruker D8 Advance XRD machine with a Cu Kα source was used to obtain the XRD spectrum. The XRD was performed in the range of 2θ of 10° to 80°, with a step size of 0.02° and 0.2 seconds per step. Each sample took ~15 minutes to collect the XRD data. A knife's edge was used to reduce the background scattering at low angles.

Figure 5 presents the quarterly variation of the fly ash sources. Fly Ash 1 had multiple crystalline phases present—quartz, anhydrite, Gehlenite, periclase, hematite, tricalcium aluminate, mullite, calcite, and free lime. The XRF data showed that Fly Ash 1 had higher calcium, magnesium, and sulfur in the 2018 sample compared to the other samples, and in XRD data, the lime, tricalcium aluminate, periclase, and anhydrite peaks also have much higher intensity in the 2018 sample compared to the other sample. Fly Ash 2 had only quartz, anhydrite, Gehlenite, periclase, hematite, and tricalcium aluminate present in the sample. The 2018 Fly Ash 2 sample had high MgO content from the XRF data, and the intensity of periclase is higher here as well. Fly Ash 4 had quartz, anhydrite, Gehlenite, periclase, hematite, tricalcium aluminate, mullite, and calcite present. Fly Ash 4 is a Class F ash, and in general, a high intensity mullite peak is observed in XRD data, but not in Fly Ash 4. The XRF data of Fly Ash 4 was consistent over different quarters, and in general, the peak intensities of the different minerals were consistent as well.

Figure 6 presents the XRD spectrum of five ash samples collected in 2018 for comparison. Fly Ash 1 and 2 had significantly high periclase content compared to other fly ash sources, whereas Fly Ash 1 had very high free lime content. Fly Ash 4 was a Class F ash, and it did not contain a significant amount of tricalcium aluminate. Moreover, the amorphous hump of Fly Ash 4 was at a lower 2θ angle than other Class C ashes, as it had a higher silica content in the amorphous phase.

In general, the XRD and XRF data were consistent with each other; the major variations in the oxide contents were also reflected in the XRD data.

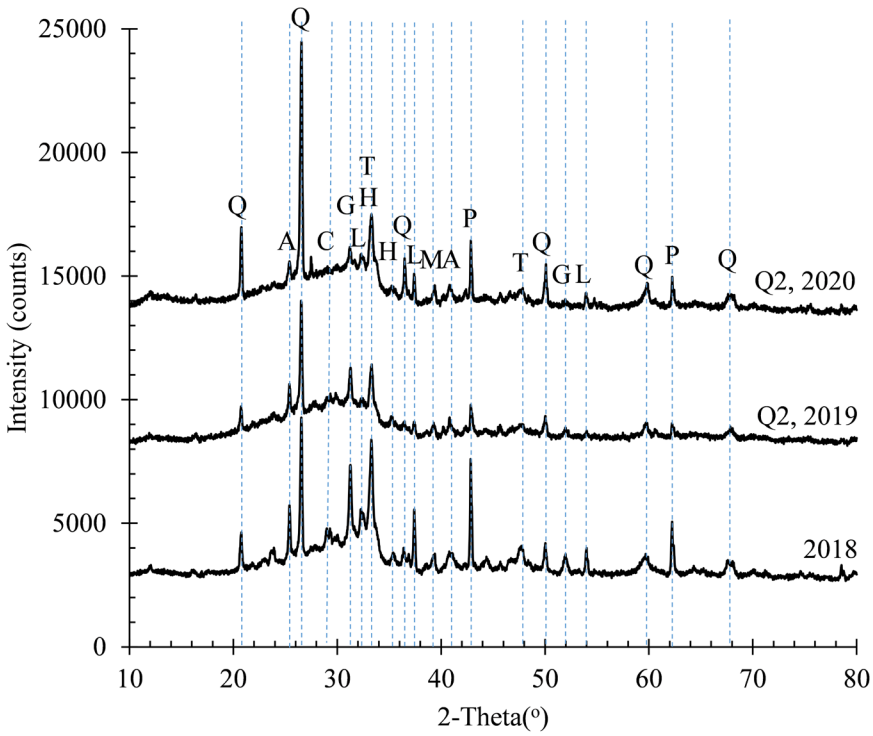

A. Fly Ash 1

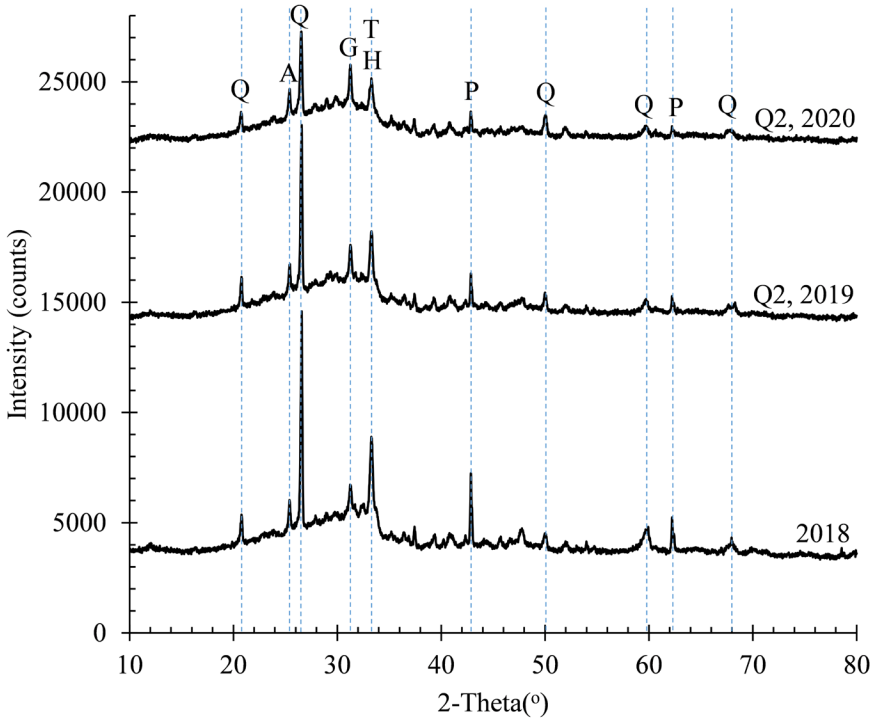

B. Fly Ash 2

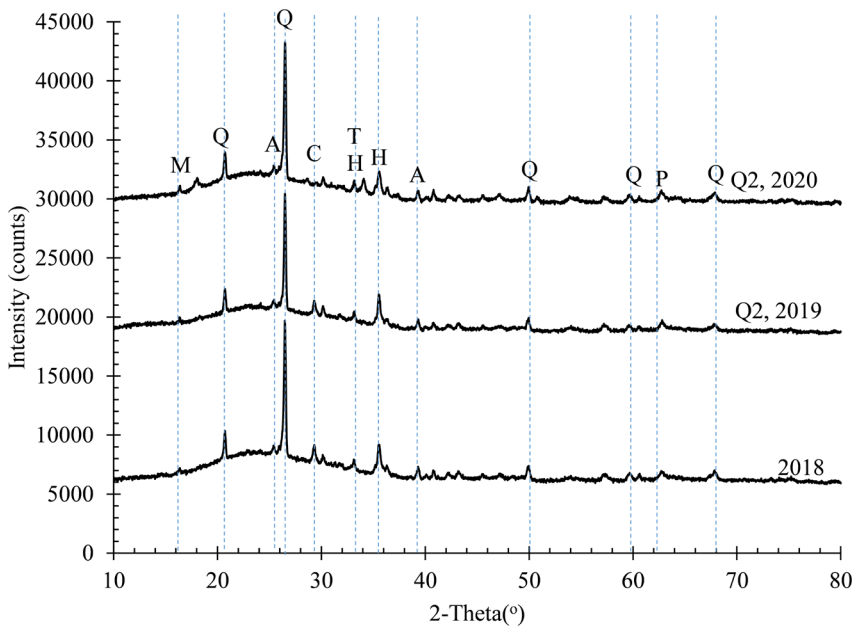

C. Fly Ash 4

Figure 5. Graphs. XRD spectrum of fly ash samples collected in different quarters.

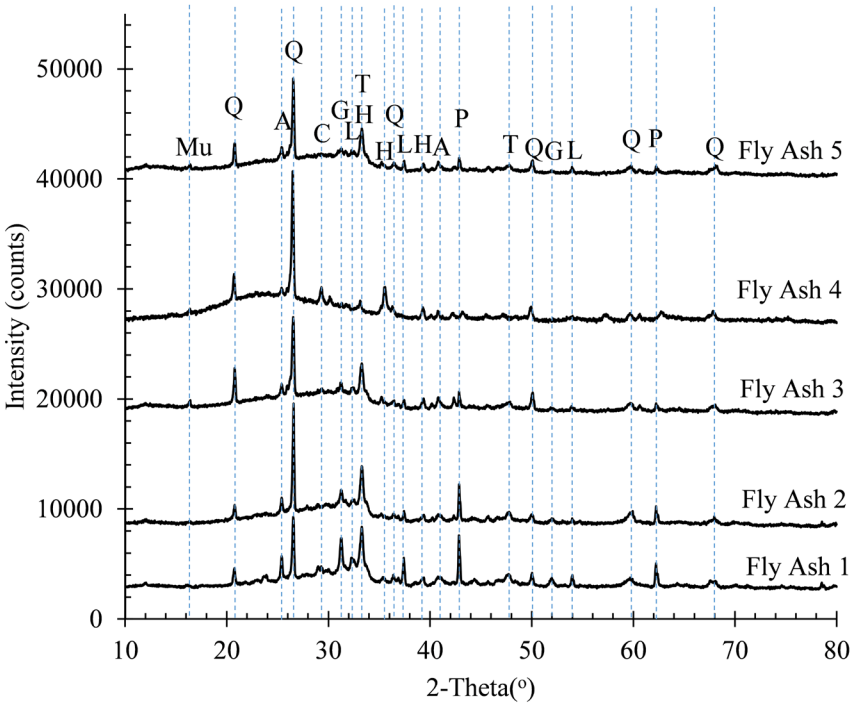

Figure 6. Graph. XRD spectrum of five fly ash samples from 2018. The labels represent the following minerals—Q: Quartz, A: Anhydrite, G: Gehlenite, P: Periclase, H: Hematite, T: Tricalcium Aluminate, M: Mullite, C: Calcite, and L: Lime.

FLY ASH AIR ENTRAINMENT AND CARBON CHARACTERIZATION

Air entrainment of concrete is important because of durability issues in freezing temperature, specifically, freeze-thaw durability and salt scaling. Most specifications require a 6% air content and a spacing factor less than 0.2 mm (7.87 mil) to ensure proper freeze-thaw durability. Even though stable and well-distributed air void systems can improve both workability and durability of concrete, excessive air content causes strength loss. Thus, it is important to control the air content within a narrow range. Many variables control the air entrainment of concrete such as the water-to-cementitious materials ratio, aggregate gradation, dosage, types of chemical admixtures (both water reducers and air-entraining agents [AEA]), chemical composition and particle size distribution of cement, and other supplementary cementitious materials.

One of the major supplementary materials used in concrete is fly ash, which tremendously affects the air-entraining performance of concrete. Fly ash contains carbon that may adsorb air-entraining admixtures, reducing the air content of the concrete. The increasing usage of low NO_x emission burners in coal power plants to comply with the new US Environmental Protection Agency (EPA) regulations (Environmental Protection Agency 2020) also increases the unburnt carbon content in fly ash (Veranth et al. 1998). In addition, the usage of activated carbon for NO_x absorption from flue gas may also contaminate the fly ash with a small amount of activated carbon, which may affect the air-entraining performance severely (Diaz-Loya et al. 2019) due to its high specific surface area. Apart from the presence of carbon in fly ash, usage of fly ash in concrete also affects the Ca^{2+} and Mg^{2+} ion concentration in the pore solution. The Ca^{2+} and Mg^{2+} ions are known to precipitate AEA, which may, in turn, affect the air-entraining performance.

Air entrainment of fly ash concrete is a very complex procedure, and even state-of-the-art characterization tools fail to predict the air-entraining performance in some cases (Tunstall, Scherer, and Prud'homme 2021). Many fly ash quality control tests have been developed to predict air-entraining performance, such as the iodine number, direct absorption, and foam index tests. The foam index test is a rapid test that generally involves adding a diluted AEA to a fly ash cement mix sequentially and shaking it till the surface is covered by a stable layer of foam. In this section, this foam index test was performed on different Illinois fly ash along with carbon characterization using XPS and LOI. Moreover, a computer vision–based foam index test called the digital foam index test (D-FIT) has been developed to reduce the sources of error between different operators and labs.

Foam Index Test

The foam index test was performed according to Harris et al. (2008c) with some small modifications. Recently, the foam index test has been incorporated into ASTM C1827 (2020). The test procedure used for this report is slightly different from ASTM C1827 and is written below:

- Step 1: Put 25 mL (0.845 oz) water, 5 gm (0.176 oz) cement, and 5 gm (0.176 oz) fly ash into a 120 mL (4.06 oz) glass vial (as seen in Figure 7).
- Step 2: Close the vial and shake it for 20 seconds. Shake it at a rate of about twice a second with a vertical distance of about 30 cm (1 ft).

- Step 3: After shaking, add 0.10 mL (3.38×10^{-3} oz) of 2.5% wood resin AEA.
- Step 4: Shake the glass vial vertically and vigorously for 10 seconds (~30 shakes).
- Step 5: Observe the top layer of the glass vial for 20 seconds and conclude the test if stable foam forms (Figure 8).
- Repeat steps 3–5 till stable foam forms. Each cycle of steps 3–5 should be completed in about 1 minute to improve consistency of this test, as the fly ash continues to absorb the AEA even without shaking.

Figure 7. Photo. Container for the foam index test.

Foam index tests were carried out on 27 different fly ash sources available in Illinois, and the test was carried out by both UIUC and IDOT (Figure 9). At that time, IDOT was following a slightly different test protocol than mentioned above. IDOT was shaking the bottle horizontally and relatively slower compared to UIUC shaking the bottle vertically and more frequently. Additionally, IDOT stopped adding AEA after reaching 1 µL AEA/gm of fly ash (6.387×10^{-3} oz AEA/lb. of fly ash) dosage. The IDOT foam index was consistently higher than the UIUC foam index, except when the UIUC foam index was greater than 1, as IDOT stopped the test after reaching 1 µL AEA/gm of fly ash (6.387×10^{-3} oz AEA/lb of fly ash) dosage.

Figure 10 presents the variation in the foam index test for five fly ash sources with two independent test operators (UIUC and IDOT) and between two quarterly samples (Q1 and Q2) from the same power plant. The foam index test demonstrated that the required dosage would depend on the type of Illinois fly ash and could be as high as 3 µL AEA/gm fly ash (1.916×10^{-2} oz AEA/lb fly ash). For different operators or the same operator but the different quarterly samples in 2019, the foam index results were within ±1 µL AEA/gm fly ash (6.387×10^{-3} oz AEA/lb of fly ash).

A. Unstable foam

B. Foam covering the entire container surface

Figure 8. Photos. Images of (a) unstable foam and (b) foam covering the entire container surface.

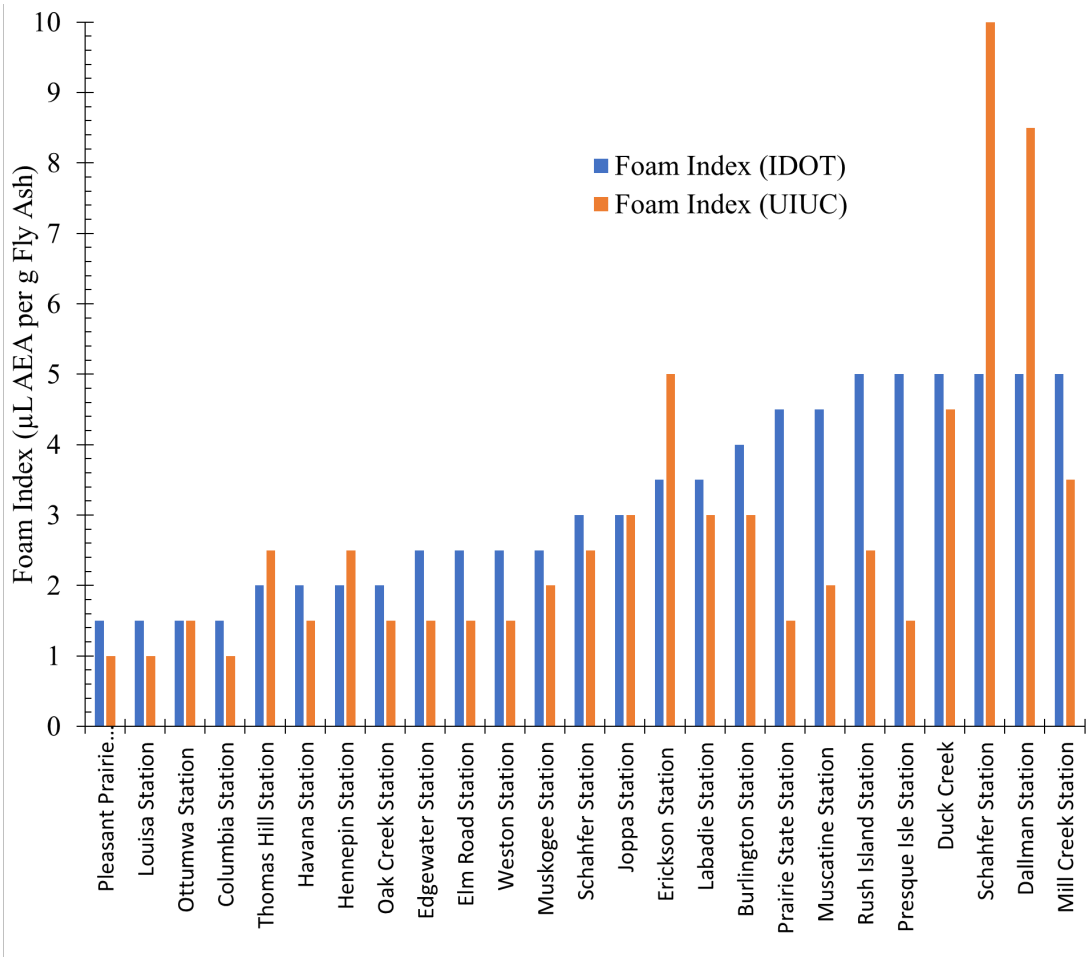

Figure 9. Graph. IDOT and UIUC variations in foam index of fly ash sources in Illinois.

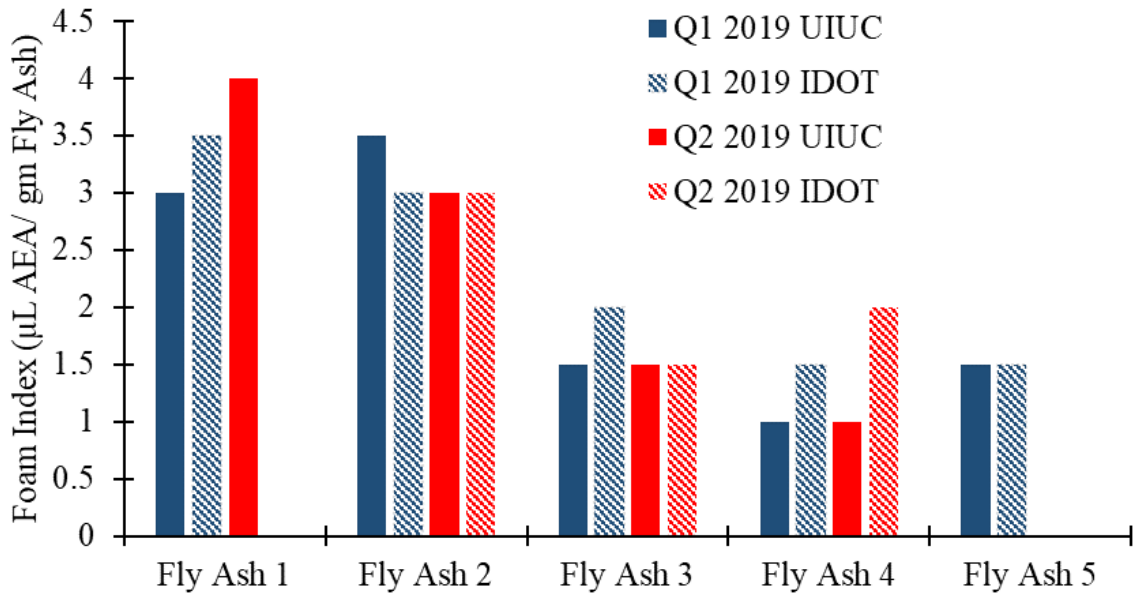

Figure 10. Graph. Quarterly foam index test results with vinsol resin–based air-entraining admixture for five fly ash sourced from Midwest power plants (Q1 2019 and Q2 2019). Foam index tests were run by the authors (UIUC) and the Illinois Department of Transportation (IDOT).

XPS

The XPS spectrum for carbon was obtained at an energy resolution of 0.1 eV. Five components of carbon were considered, and their peak positions are shown in Table 5. Other carbon components such as metal carbides and carbon halides were not considered, as they were not observed in the fly ash samples. Figure 11 presents a typical fit of C 1s XPS spectra, and Table 6 shows the relative concentration of the five carbon components in different fly ash. The full width at half maximum (FWHM) of all five components were kept fixed, and the goodness of fit was obtained from a Monte-Carlo simulation with 200 iterations (Table 7).

Table 5. Component Analysis of Carbon Using XPS

Carbon Type	C-C, C-H	C-OH, C-O-C	R2-C=O	O=C-O	CO_3
Peak Position (eV)	285.0	286.5	288.0	289.0	289.5

Table 6. Carbon Components Present (in atom %) in Fly Ash and Their Corresponding FWHM (in eV)

	C-C, C-H	C-OH, C-O-C	R2-C=O	O=C-O	CO_3	FWHM
Fly Ash 1	81.69	10.2	0.31	7.81	0	1.29
Fly Ash 2	82.56	9.97	0.88	6.59	0	1.32
Fly Ash 3	81.78	9.96	0.91	7.35	0	1.29
Fly Ash 4	83.08	8.99	0.79	6.75	0.39	1.3
Fly Ash 5	84.16	9.08	0.35	6.41	0	1.29

Table 7. Standard Deviation in Carbon Component Fitting (in eV) Using Monte-Carlo Simulation

	C-C, C-H	C-OH, C-O-C	R2-C=O	O=C-O	CO3
Fly Ash 1	0.73	0.6	0.31	0.57	0
Fly Ash 2	0.93	0.72	0.58	0.72	0
Fly Ash 3	0.84	0.67	0.47	0.53	0
Fly Ash 4	1.04	0.7	0.61	0.83	0.64
Fly Ash 5	0.8	0.71	0.37	0.54	0

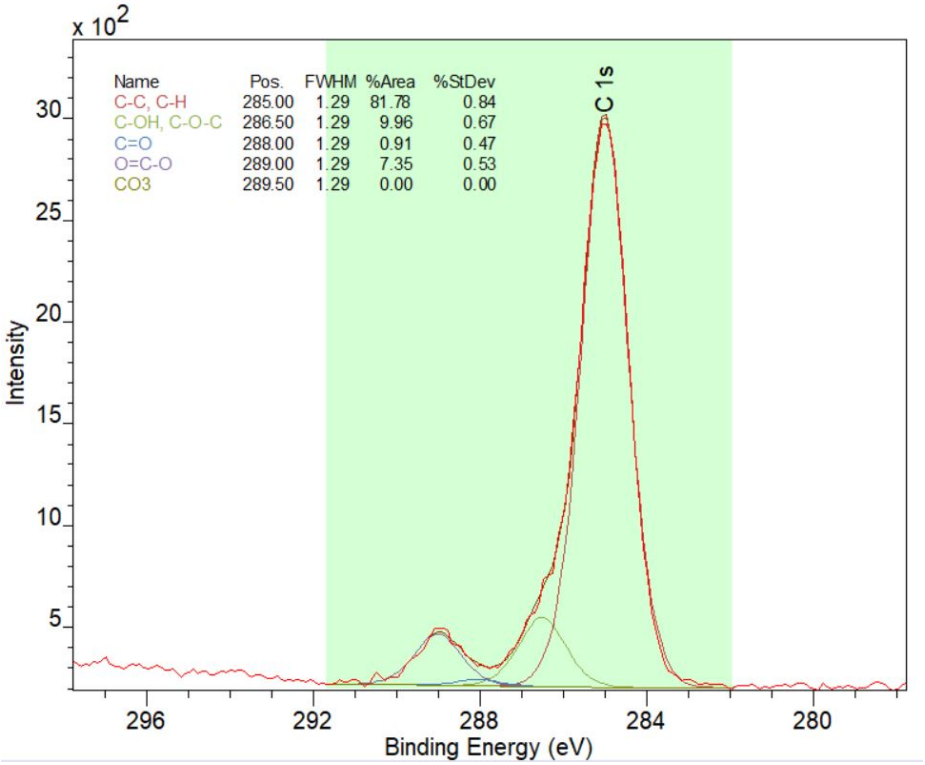

Figure 11. Graph. C 1s spectra of Fly Ash 2.

The C 1s XPS data was fitted reasonably well, as the standard deviations in fitting were mostly below 1%. Most of the carbon present on the surface of the fly ash were of C-C or C-H types, which are known to adsorb AEAs, increasing the AEA dosage requirement to achieve desirable air-entraining performance. Deng et al. (2016) also performed XPS of fly ash samples and found that the C-C and C-H groups generally dominate different carbon components. For Deng et al. (2016), the amount of C-C and C-H groups was around 55%–60% for most of the ashes investigated compared to 81%–84% observed in the fly ash investigated in this report.

The relative amount of different carbon components did not vary significantly among the five fly ash samples tested. The literature shows that the relative amount of different carbon components does vary a lot among different samples. For example, Deng et al. (2016) found that the relative amount for the C-C and C-H groups could be as low as 25%.

LOI, XPS, and Foam Index Tests

A comparison of LOI, XPS, and foam index tests was performed of the five fly ash samples to understand their interdependence (Table 8). LOI was measured following ASTM C311 (2018). The foam index test was performed using the method mentioned in the previous section titled "Foam Index Test." All data presented in Table 8 were obtained from samples collected in 2018, so the foam index results do not match Figure 10.

Because the C-C and C-H groups adsorb the AEA, only these forms of carbon (C-C and C-H groups) is considered. The XPS absolute atom percentage of C-C and C-H was calculated using this formula:

(absolute C-C, C-H atom %) = (total carbon atom %) x (relative percentage of C-C, C-H)

The XPS/LOI is a semi-empirical parameter. A higher XPS/LOI represents that a higher fraction of total carbon present in the fly ash is present on the surface of the fly ash particles, assuming that LOI is a good indicator of total carbon present in the fly ash. XPS/LOI showed very wide variations among the five samples tested (Table 8).

Figure 12 shows the inter-relationship between XPS, LOI, and foam index. In general, they are all related, but no significant advantage of using XPS over LOI was found for the five fly ash sources.

Table 8. Comparison of Foam Index Test, LOI, and XPS (2018 Fly Ash Samples)

	XPS (C-C, C-H)	LOI	Foam Index	XPS/LOI
	(atom %)	(weight %)	(µL AEA/gm fly ash)	(atom %) / (weight %)
Fly Ash 1	40.27	0.77	5.00	52.29
Fly Ash 2	37.14	0.70	3.50	53.06
Fly Ash 3	30.98	0.31	2.00	99.92
Fly Ash 4	31.65	0.47	4.50	67.33
Fly Ash 5	32.68	0.52	1.50	62.84

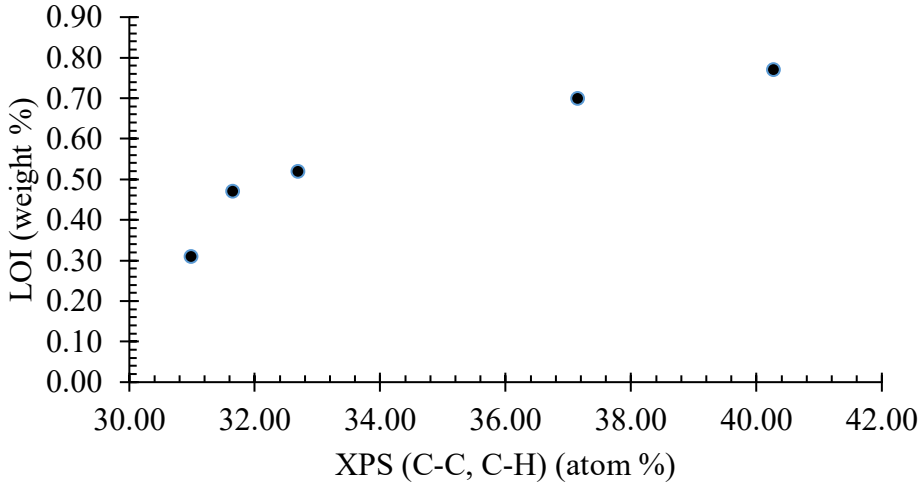

A. XPS vs. LOI

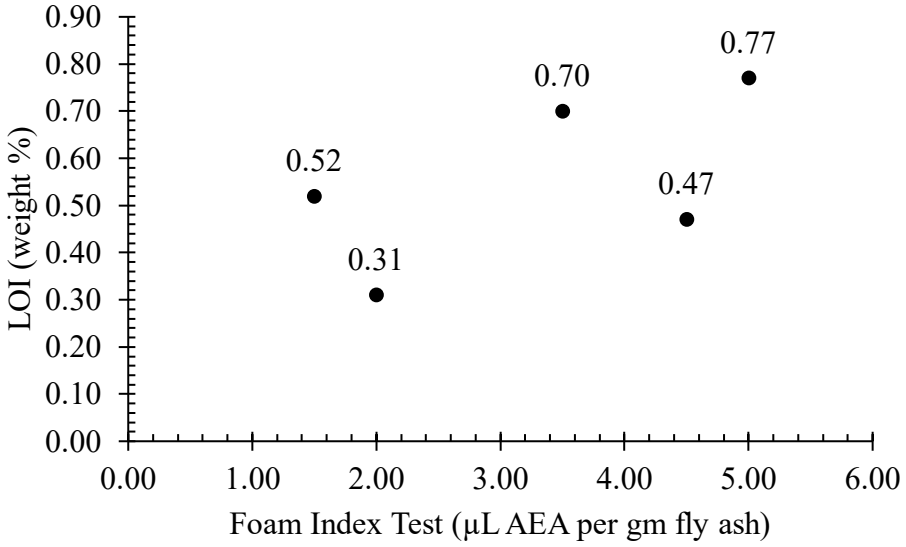

B. LOI vs. foam index

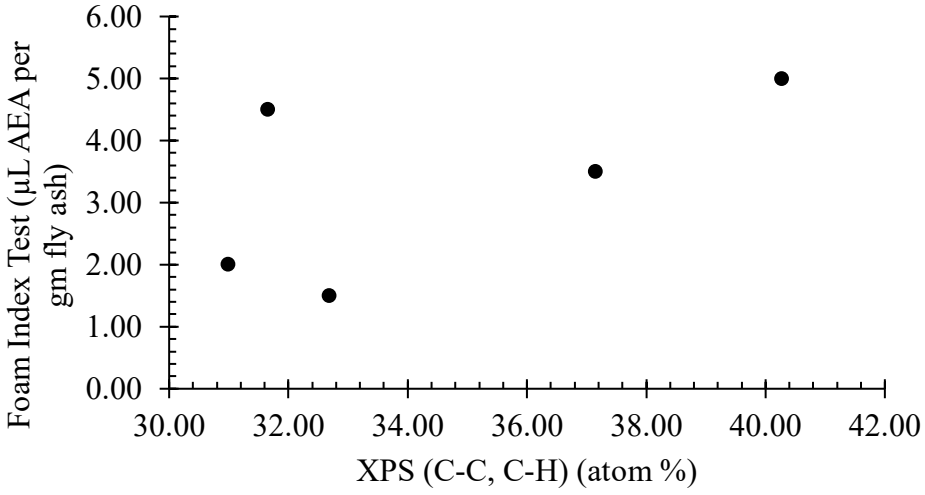

C. Foam index vs. XPS

Figure 12. Graphs. Relationship between (a) XPS vs. LOI, (b) LOI vs. foam index, and (c) foam index vs. XPS

Digital Foam Index Test

Since the introduction of the foam index test about 30 years ago, researchers have studied (Harris et al. 2008b, 2008c, 2008a) the effects of different test parameters such as the water-to-binder ratio, fly ash-to-binder ratio, container capacity versus the amount of solution used, mixing procedure, time of test, as well as proposed guidelines for a standardized test method given its known repeatability issues (Taylor et al. 2006a, 2006b). One of the major reasons behind the repeatability issues of the foam index test is that human judgment is used to know whether the foam has covered the surface fully, leading to errors. Stencel, Song, and Cangialosi (2009) automated the foam index test to

determine bubble stability through measuring the number of acoustic events using acoustic sensors, which can then be related to the foam index test. However, acoustic emissions caused by bubble bursting have frequencies in the range of 500–15,000 Hz and thus can be easily affected by the ambient sound environment.

In this section, we propose using a computer vision technique to determine when the foam is stable and when the foam is covering the entire solution surface, reducing operator error and improving consistency between laboratories. The proposed procedure will employ the traditional foam index test method but also take a video of the created foam layer with a digital camera. A neural network–based computer vision algorithm will then be used to evaluate the foam stability and surface area covered by the foam.

Methodology

The digital foam index data collection will follow Ley et al. (2008), with some modifications from the recently approved foam index test, ASTM C1827 (2020). The proposed test setup is shown in Figure 13; the steps of the digital foam index test are listed next:

- Step 1: Mix 5 gm (0.176 oz) cement, 5 gm (0.176 oz) fly ash, and 25 mL (0.845 oz) water in a ~100 mL (3.38 oz) container.
- Step 2: Shake it vigorously and vertically for 20 seconds.
- Step 3: Add 0.1 mL (3.38×10^{-3} oz) of diluted AEA (preferably vinsol resin–based AEA).
- Step 4: Shake it vigorously and vertically for 10 seconds.
- Step 5: Allow the container to stay undisturbed and collect a video of the foam layer for 30 seconds. A valid dosage level is when the foam still covers the entire surface after 20 seconds.
- Step 6: Repeat steps 3–5 until foam covers the entire container surface at 20 seconds. If this happens with less than 1 mL (0.0338 oz) (or 10 drops) of diluted AEA solution, discard this test and restart testing from step 1 again using a more diluted AEA solution. If a stable foam is formed after adding more than 1 mL (0.0338 oz) of diluted AEA solution, continue with steps 3–5 until the foam covers the entire solution surface.
- Step 7: The amount of AEA required for a foam layer that covers the entire surface area of the container is taken as the foam index of the fly ash sample and is expressed in terms of µL AEA/gm of fly ash (oz AEA/lb of fly ash).

After collecting video at 30 frames per second and extracting one frame per second, a computer vision–based technique will be developed to assess both the percentage of the surface covered and the stability of the foam.

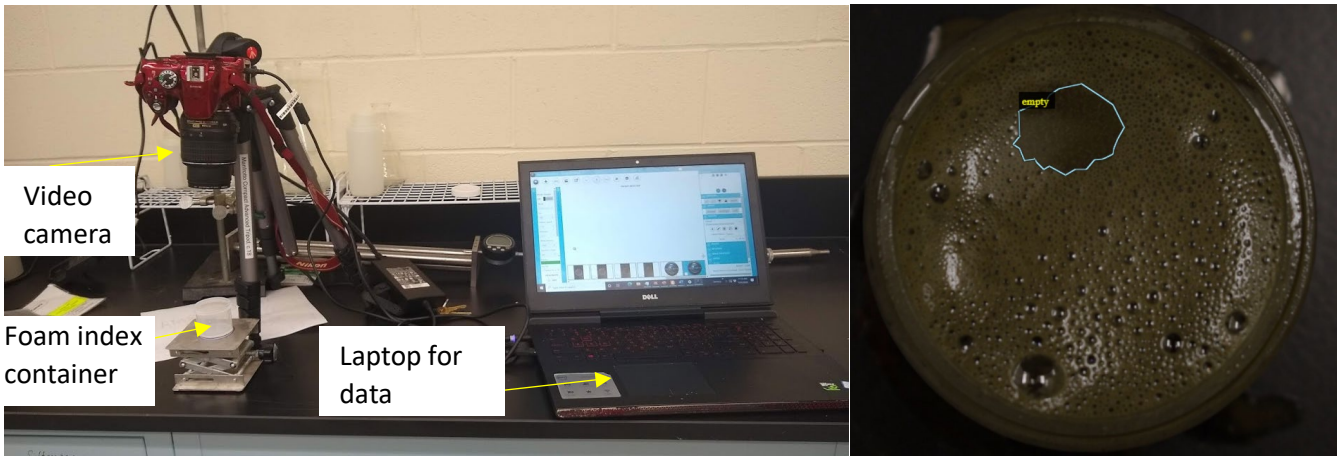

A. Digital foam index test set up B. Image of the foam layer

Figure 13. Photos. Digital foam index test set up (a), consisting of a video camera, foam index container, and a laptop for data storage. A representative image of the foam layer is shown in (b), with the empty area manually annotated.

Computer Vision Techniques for Characterizing Foam

In the last decade, multiple algorithms and tools have been developed for image segmentation and classification using deep learning methods. Region-Convolutional Neural Network (R-CNN) is one type of CNN-based deep learning object-detection approach by Girshick et al. (2014). The algorithm has already been modified by many to improve both the accuracy, training, and testing speed, leading to Fast-RCNN (Girshick 2015) and Faster-RCNN (Ren et al. 2017). Faster-RCNN identifies each candidate object in an image and shows a "bounding box," i.e., a rectangular region where the candidate object is identified. Faster-RCNN has been further improved to output the exact location of the candidate object, including pixel-to-pixel alignment, which is named Mask-RCNN algorithm. This Mask-RCNN algorithm will be used to characterize the images obtained from the digital foam index test video.

Mask-RCNN Digital Foam Index Algorithm

Mask-RCNN is a reinforced learning algorithm and needs to be trained to characterize the foam layer. The Mask-RCNN algorithm involves multiple steps, as follows:

Step 1—Data Collection and Annotation: Images extracted from the foam index test video will be annotated using the VGG VIA software to mark the empty area, i.e., the surface area without any bubbles. Approximately 650 randomly chosen annotated images will be used for the training dataset and 160 randomly chosen annotated images will be used for the validation dataset.

Step 2—Mask-RCNN Training Configuration: The Mask-RCNN algorithm will be implemented in Python using Tensorflow and Keras (Abdulla 2017). The annotated images have a dimension of 1920 × 1080 pixels, which will be down sampled and padded with zeroes to keep the image aspect ratio unchanged but to achieve a 1024 × 1024 pixel image because square images are computationally faster. Initially training a neural network without weighting functions can become computationally expensive, so a method called "transfer learning" will be applied. The initial weights of this training

model will be assigned the COCO weights taken from pre-training on the Microsoft COCO database. Finally, the deep learning model will be trained using a desktop PC with an Intel Core i7-7700 @3.6 GHz CPU, 32 GB RAM, and NVIDIA 1080 Ti GPU with a learning rate of 0.001.

Step 3—Model Validation: One major concern with using a neural network–based approach for image segmentation is over-fitting the data, where the weights of the neural network may change in a way to perfectly fit the training dataset without learning the different key features in the images. Thus, overtraining can lead to high prediction errors. A loss function is used to measure the model error in the prediction of both the training and the validation dataset, and the evolution of the loss function over training time will be monitored to choose the optimum training weights. Mask-RCNN model uses a loss function (zero to three), which is a sum of the loss functions corresponding to classification, bounding box prediction, and, finally, the pixel-to-pixel aligned mask generation.

Step 4—Evaluate Mask-RCNN Model Quality: Three parameters—precision, recall, and error—will be used to quantify the quality of the trained model on the validation dataset. Precision is the ratio of true positives (TP) out of all the predicted positive cases (Figure 14), whereas recall is the ratio of true positives out of total real positive cases (Figure 15). Error measures the ratio of false-positive cases over real positive cases (Figure 16).

$$\text{Precision} = \frac{TP}{TP+FP}$$

Figure 14. Equation. Equation to calculate precision.

$$\text{Recall} = \frac{TP}{TP+FN}$$

Figure 15. Equation. Equation to calculate recall.

$$\text{Error} = \frac{FP}{TP+FN} \times 100$$

Figure 16. Equation. Equation to calculate error.

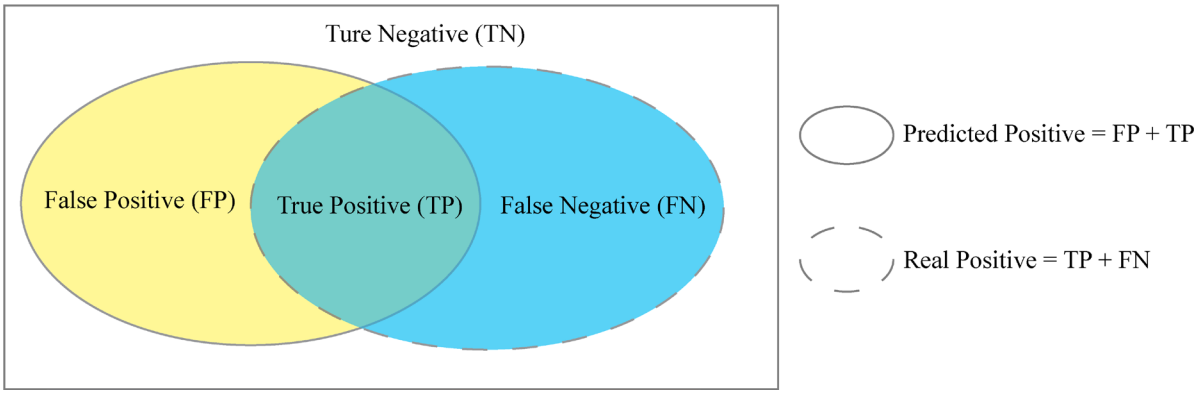

Figure 17. Graph. Parameters for assessing the actual empty area (real positive) and the predicted empty area (predicted positive).

The Predicted Positive (Figure 17) can be divided into two parts: area that is predicted to be empty but actually is not (False Positive, FP), and the area that is predicted to be empty and actually is empty (TP). The Real Positive area consists of TP and the area that is actually empty but predicted not to be empty (False Negative FN). True Negative (TN) is the area that is actually not an empty area and correctly predicted to be not an empty area.

Training of the Mask-RCNN Model

The evolution of the statistical parameters associated with the Mask-RCNN model with training times is shown in Figure 18. The training time is expressed in terms of "epoch," which is the number of times that the learning algorithm has worked through the entire training dataset. The loss in the training dataset decreases logarithmically in general over the entire 350 epochs of training. In contrast, the loss function in the validation dataset decreases only till 50–100 epochs, and then a slight increase in loss function is observed, potentially due to over-fitting in the training dataset. To choose a particular epoch of training that can be used over all the datasets, the different parameters described in the previous section titled "Mask-RCNN Digital foam Index Algorithm" were calculated over the validation dataset. The recall and precision both increased significantly till 20 epochs of training and then became close to constant. Interestingly, the value of error increased and decreased randomly with increasing epochs of training till epoch 80, and then sharply decreased close to ~1 after 100 epochs of training. As the error decreased significantly at the 100th epoch, the weights obtained after training the 100th epoch will be used for identifying the empty area.

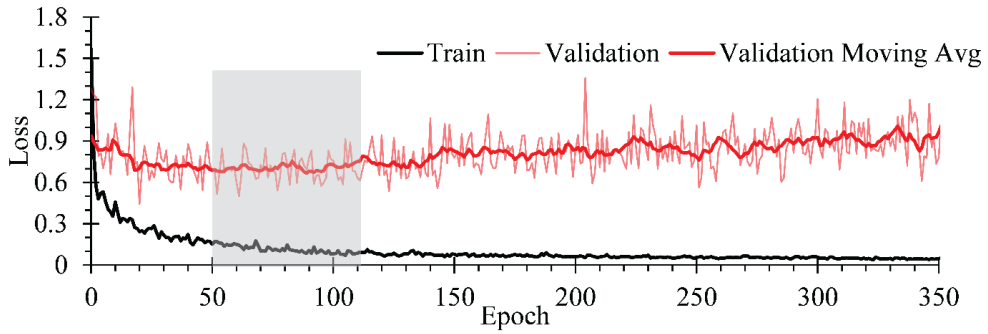

A. Change in the value of the Mask-RCNN loss function over epochs of training

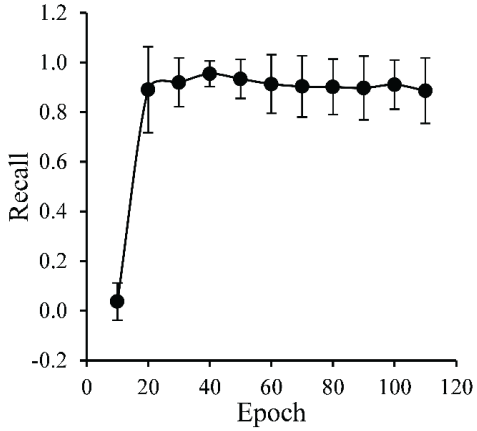

B. Evolution recall calculation

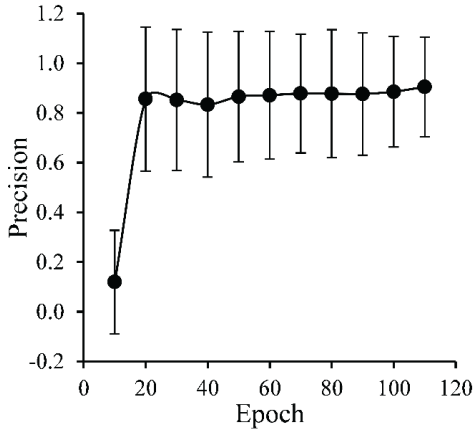

C. Precision calculation

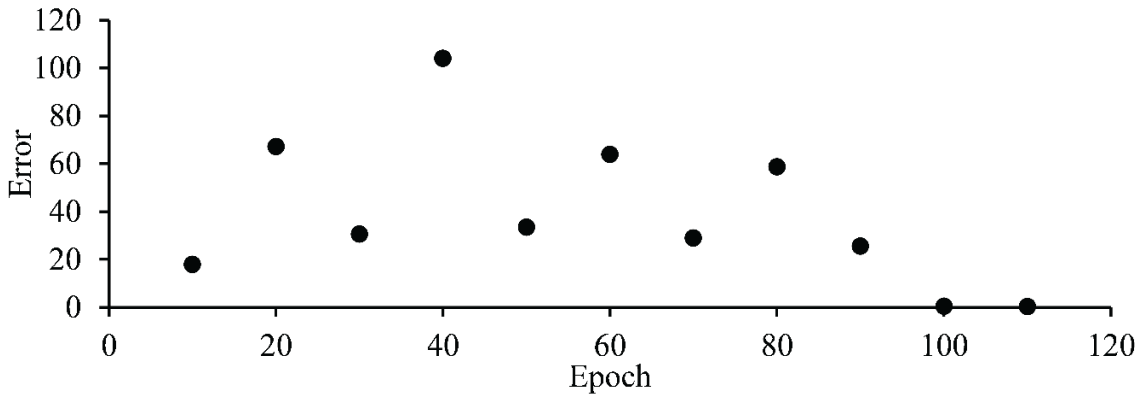

D. Error calculation

Figure 18. Graphs. Evolution of different statistical parameters with training time of the Mask-RCNN model: (a) change in the value of the Mask-RCNN loss function over epochs of training for both the training and validation datasets. The moving average was calculated using seven epochs. The (b) evolution recall, (c) precision, and (d) error calculated over the validation dataset are also shown. The standard deviations are shown in the error bars in Figures 18-B and 18-C.

Digital Foam Index Test Result and Discussion

The Mask RCNN model quantifies the empty area in pixel counts, and the empty area pixel count has been normalized to the bottle cross-sectional area pixel count to obtain the "empty area fraction." Five fly ash samples were tested, and their LOI was measured. Four fly ash sources with relatively low LOI (0.3% to 0.8%) were chosen along with an ash sample with very high LOI (3.2%). Two AEAs, one sodium olefin sulfonate and one vinsol resin–based, were used in this study.

The results of the digital foam index test of a representative fly ash sample (Fly Ash 3) are shown in Figure 19, with the foam layer covering the entire container surface after adding 24 drops of AEA (2.4 µL AEA/gm fly ash or 0.01533 oz AEA/ lb fly ash). The empty area fraction measured after 20 seconds of shaking decreases with increasing AEA dosage until it becomes zero (Figure 19-A). The empty area fraction measured before 5 seconds varies rapidly, and sometimes the empty area fraction shows anomalies with the empty area fraction increasing with AEA dosage. To further understand the effect of AEA dosage on the evolution of empty area fraction with time, the data in Figure 19-A was replotted with the empty area fraction on the y-axis and number of drops of AEA on the x-axis (Figure 19-B). The empty area fraction did not change with time (time > 5 seconds) after 16 drops of AEA addition, showing that the foam layer becomes stable only after 16 drops of AEA addition (Part 1), even though it takes 24 drops to make the foam layer cover the entire container surface (foam index, part 2). It takes less AEA to make the foam layer stable compared to the amount of AEA required to make the foam layer cover the entire container surface area.

To further understand the effect of the AEA type and LOI of the ash on the evolution of the empty area fraction, the dosage required to make the foam layer stable (Part 1) and the dosage required to achieve complete coverage of the test container surface (foam index, part 2) were plotted (Figure 20). In general, the foam index increased with LOI content (Figure 20-A). The foam index was higher for the vinsol resin–based AEA compared to the sodium olefin sulfonate–based AEA. However, the

AEA dosage required to achieve stable foam was higher for the sodium olefin sulfonate–based AEA compared to the vinsol resin–based AEA. The ratio of foam index and part 1 did not change much with different LOI values, and but was different for the two different AEAs tested. The first part is related to the adsorption of AEA into the fly ash particles and, thus, is expected to depend both on the AEA and the fly ash characteristics. The second part depends on the surface tension of the solution, and mostly depends on the AEA type.

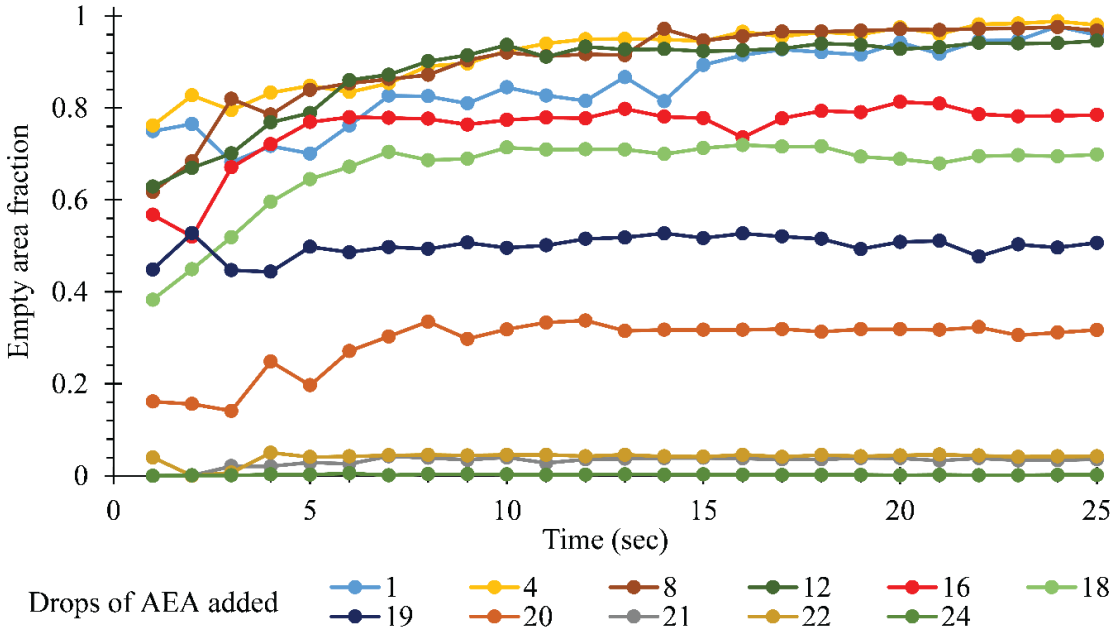

A. Change in empty area fraction with time

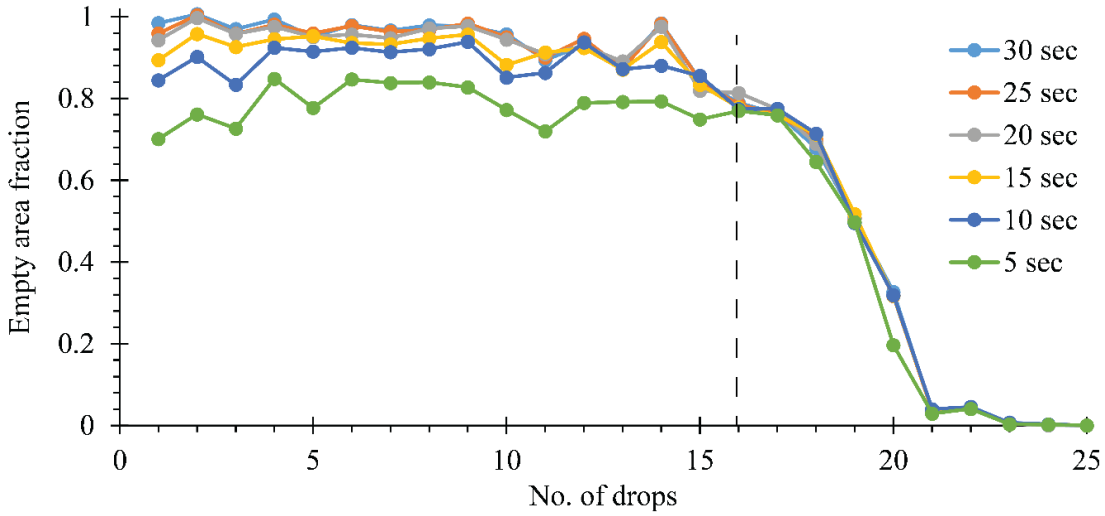

B. Evolution of empty area fraction with the number of drops of AEA addition

Figure 19**. Graphs. Change in empty area fraction with time (a) for different AEA dosage addition for a representative fly ash sample (Fly Ash 3). The evolution of the empty area with the number of drops of AEA addition for different times after stopping the shaking is shown in (b). Both figures use the same digital foam index test data.**

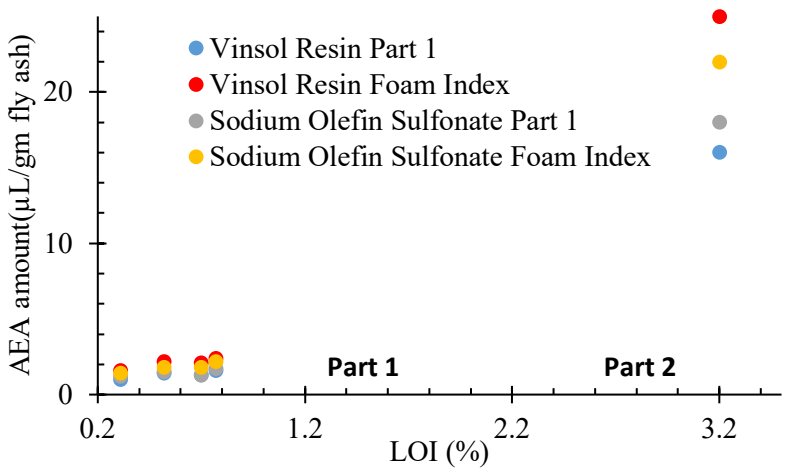

A. AEA dosage required to make foam layer stable and foam index for ashes with different LOIs

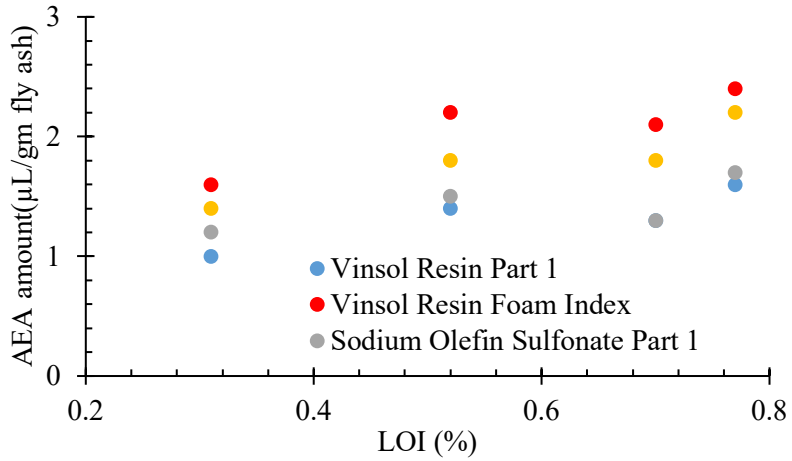

B. Zoomed-in version of Figure 20-A

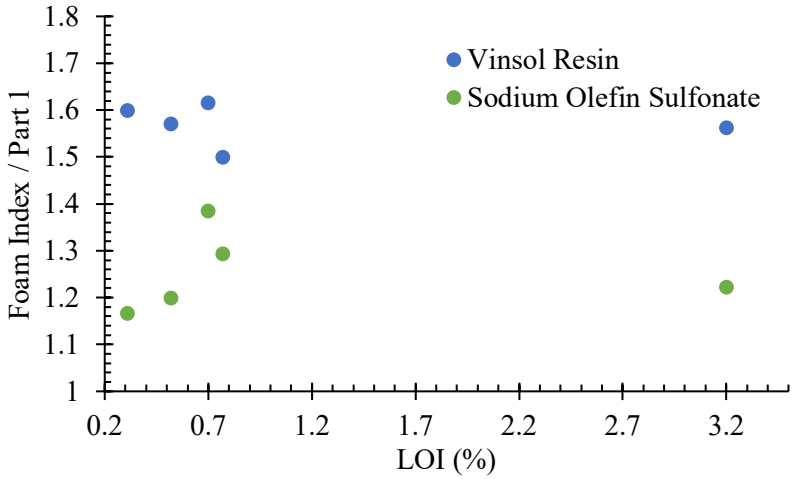

C. Ratio of foam index and AEA dosage required for making the foam layer stable

Figure 20. Graphs. AEA dosage required for making the foam layer stable and the foam index for different ashes with different LOIs. A zoomed version of (a) is shown in (b). The ratio of foam index and AEA dosage required for making the foam layer stable is plotted in (c).

CHAPTER 3: HYDRATION OF HIGH-VOLUME FLY ASH CONCRETE

Hydration of different high-volume fly ash mixes were performed using an isothermal calorimeter at 22°C (71.6°F). All mixes tested had a 0.45 water-to-binder ratio (w/b) unless noted. After inserting the sample in the calorimeter, the data obtained in the first 45 minutes was discarded, as the thermal equilibrium of the calorimeter was disturbed while inserting the sample. Figure 21 shows photographs of the isothermal calorimeter and the glass ampule used.

A. Isothermal calorimeter

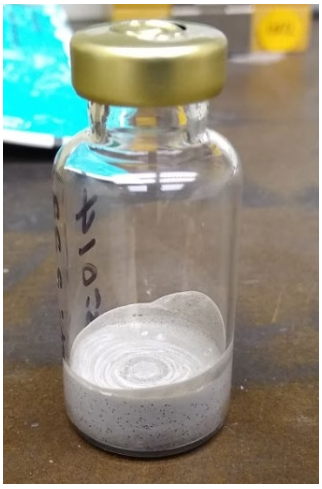

B. Glass ampule

Figure 21. Photos. Photograph of (a) isothermal calorimeter and (b) glass ampule.

In this report, many test variables such as quarter-to-quarter variation of the fly ash source, different cement sources, replacing binder with micro- and nano-limestone, and using a water reducer and superplasticizer were studied. The cumulative heat evolved over 48 hours of hydration were studied along with estimating the setting time. (See "Hydration of HVFAC" in Appendix A for a more detailed explanation of the isothermal calorimeter and calculation of setting time from the heat flow curves including Figure 43.)

QUARTER-TO-QUARTER VARIATION

Four fly ash samples from Quarters 1 and 2 (Q1 and Q2) in 2019 were tested at 40% of the binder content to understand the quarter-to-quarter variation of fly ash sources. Figure 22 and Figure 23 show the heat flow rate and cumulative heat flow of the mixes tested. All four fly ash sources had cumulative heat releases within 68%–71.5% of the straight cement mix (control) after 48 hours of hydration.

Fly Ash 1 and 4 showed almost the same heat flow rate curve, whereas Fly Ash 2 and 3 showed slightly different heat flow rate for different quarter samples. In Fly Ash 3, the relative position of Peak 1 and Peak 2 (as described in Figure 43) changed in the quarter-to-quarter sample, showing a possible change in sulfate content. In terms of cumulative heat, ashes from different quarters showed very similar heat released after 48 hours of hydration. The setting times of two different quarter

samples were within ±15 minutes for Fly Ash 1 and 4, whereas the setting time deviated as much as 30 minutes for Fly Ash 2 and 3 (Table 9).

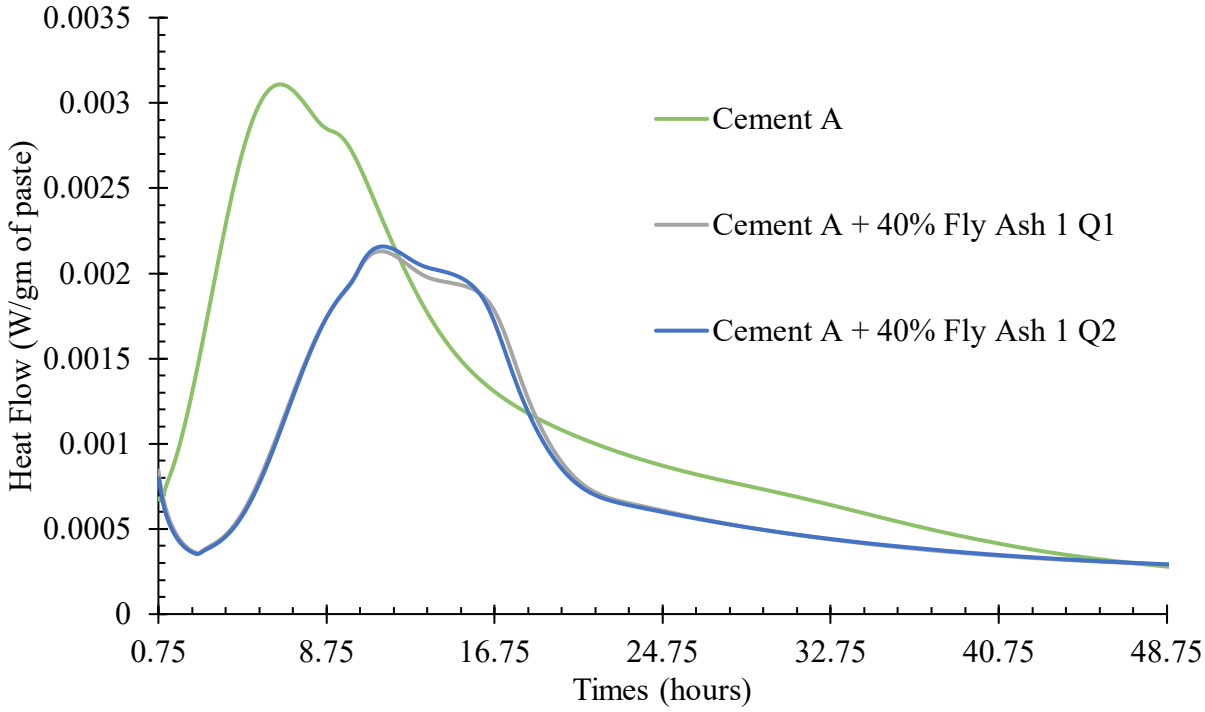

A. Fly Ash 1

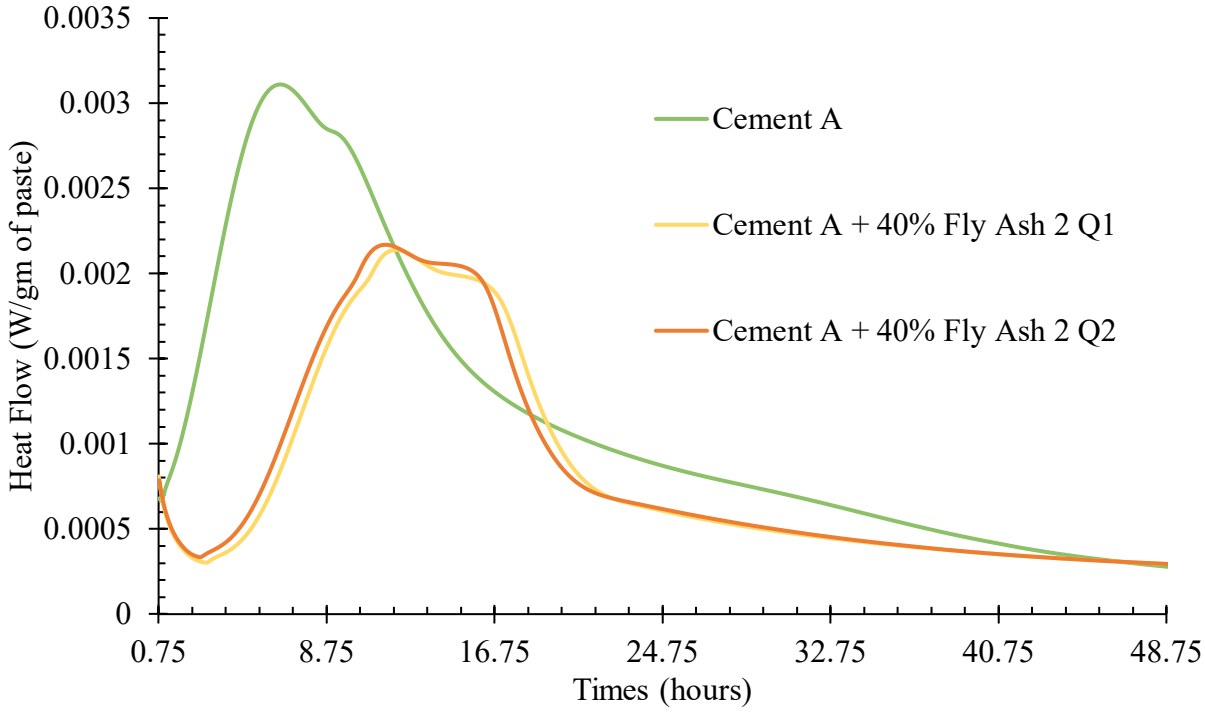

B. Fly Ash 2

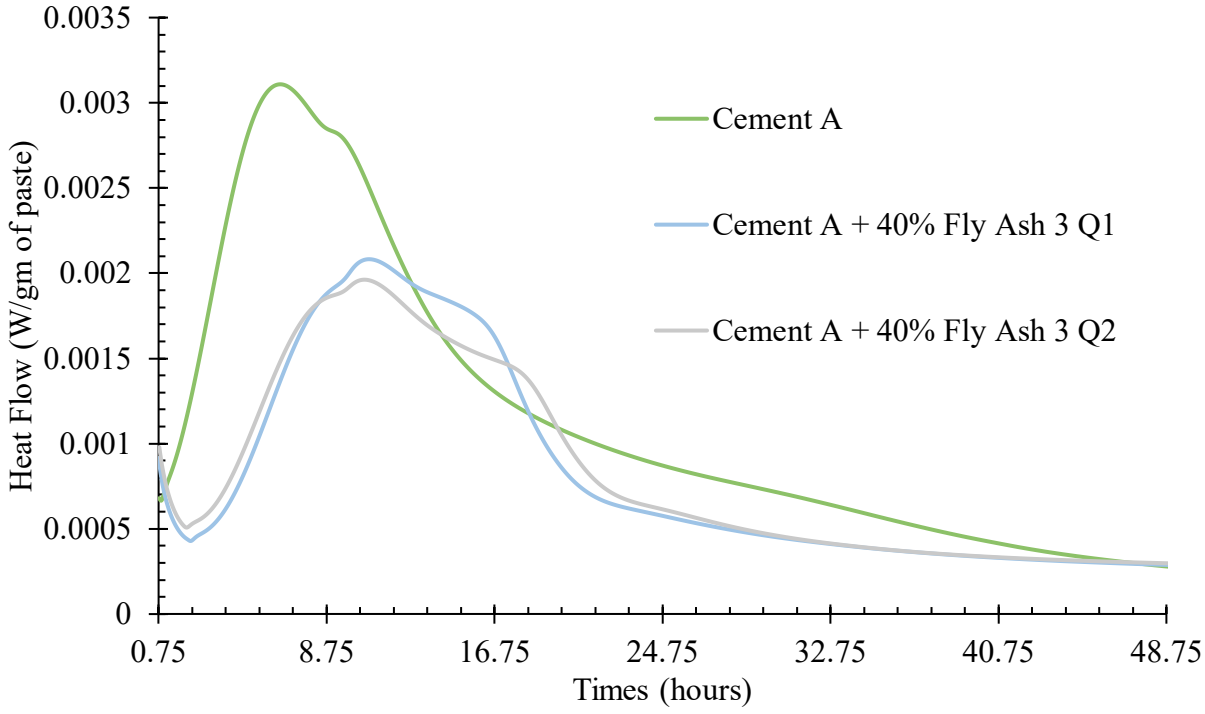

C. Fly Ash 3

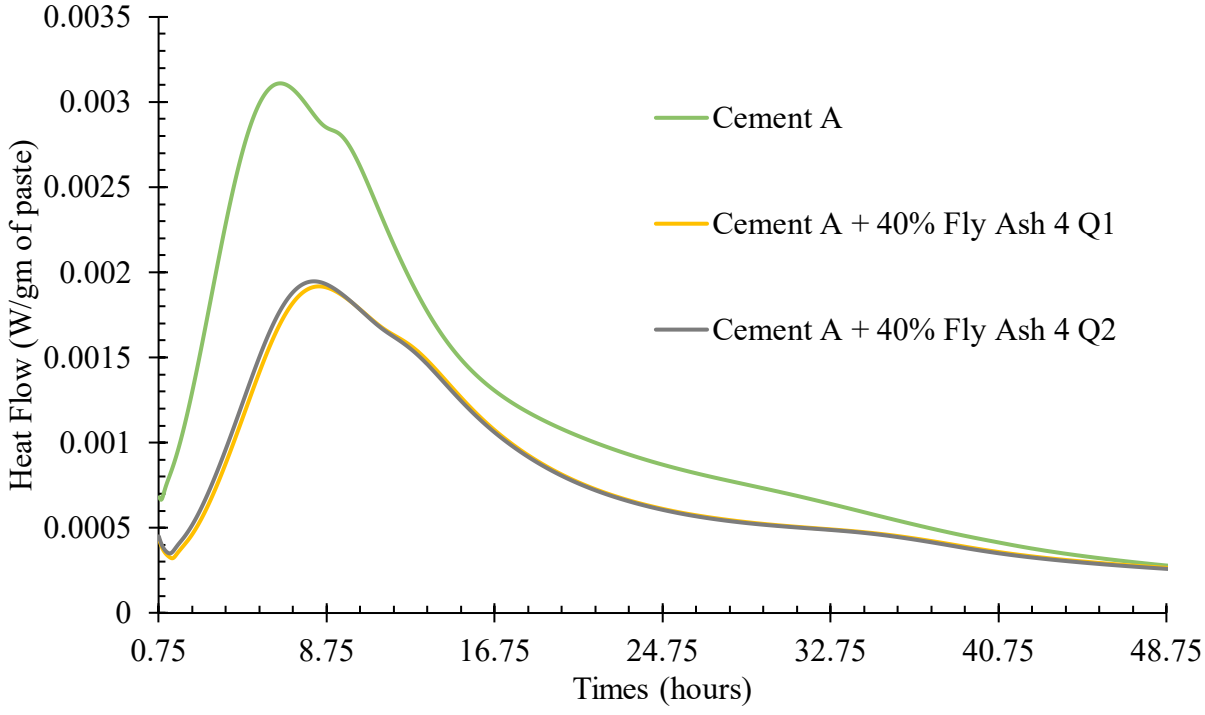

D. Fly Ash 4

Figure 22. Graphs. Heat flow rates for 40% weight replacement of cement with (a) Fly Ash 1, (b) Fly Ash 2, (c) Fly Ash 3, and (d) Fly Ash 4 for two quarterly samples in 2019 (Q1 and Q2).

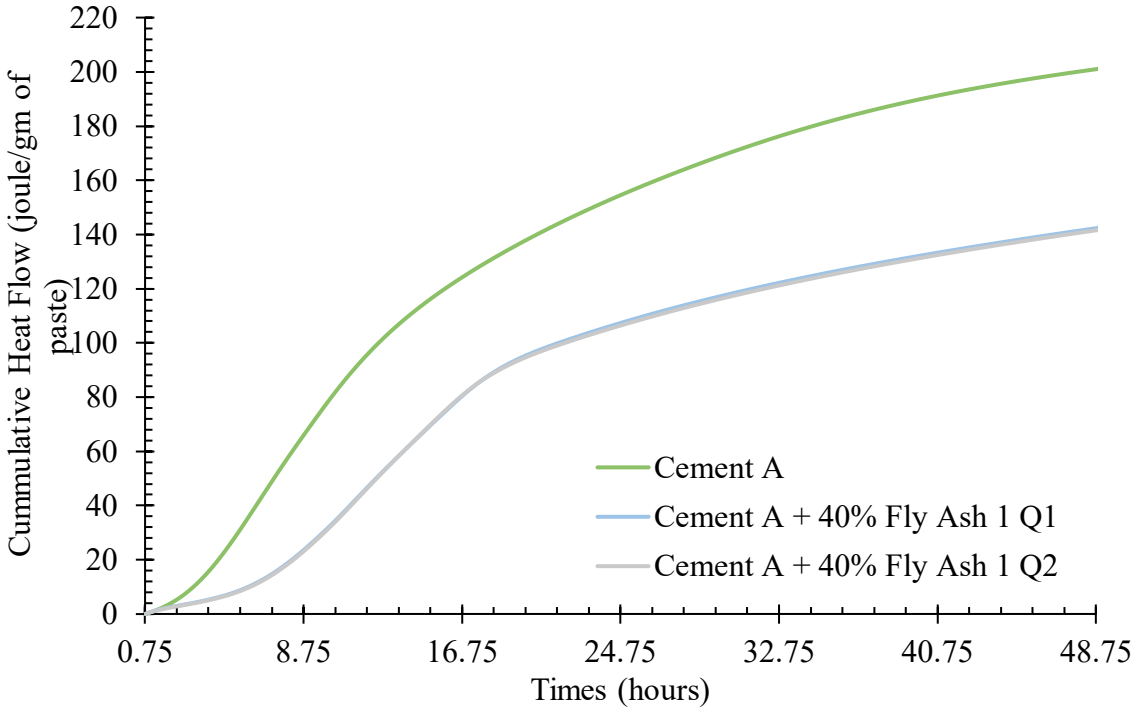

A. Fly Ash 1

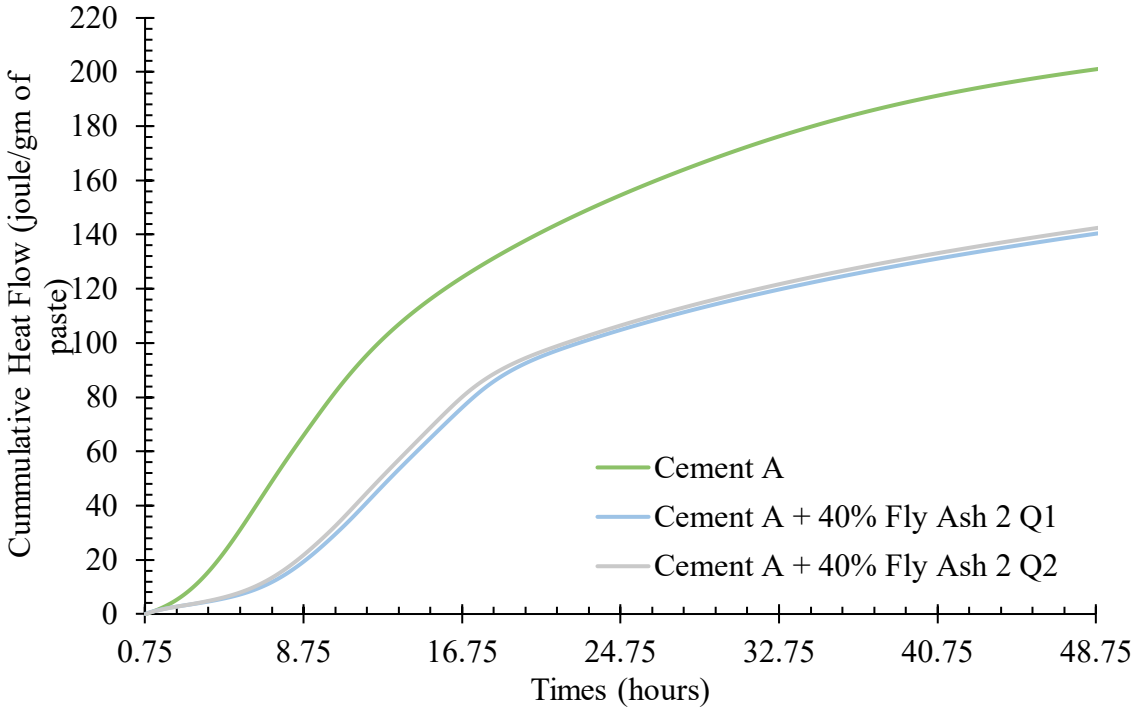

B. Fly Ash 2

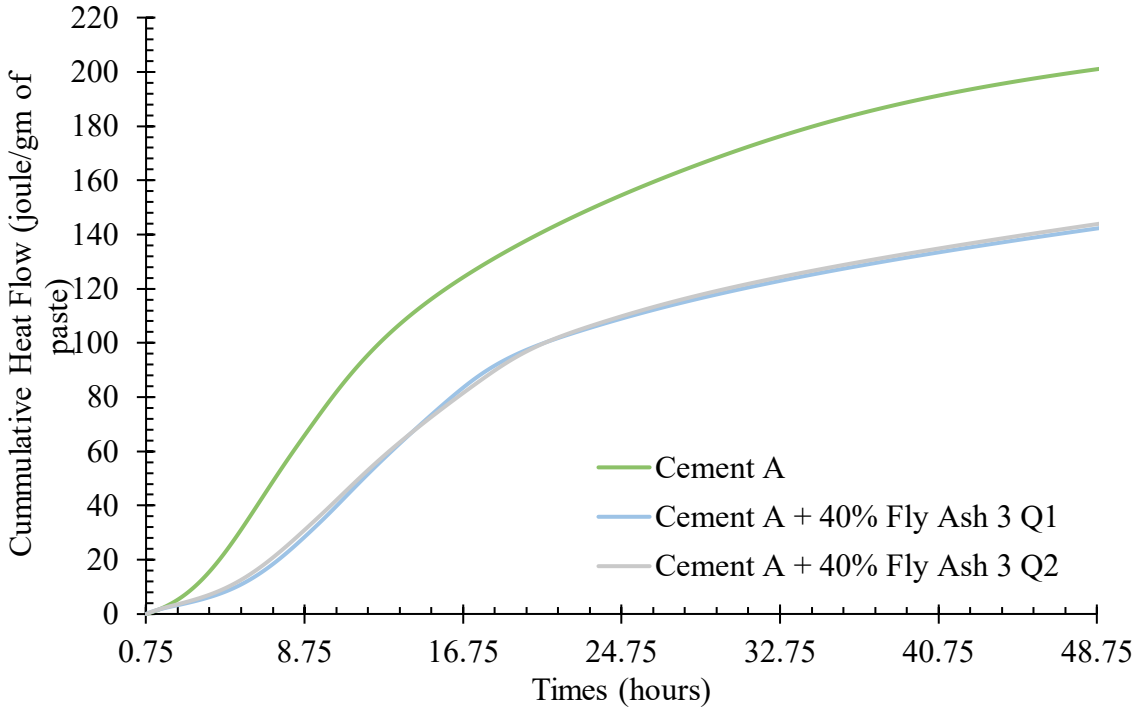

C. Fly Ash 3

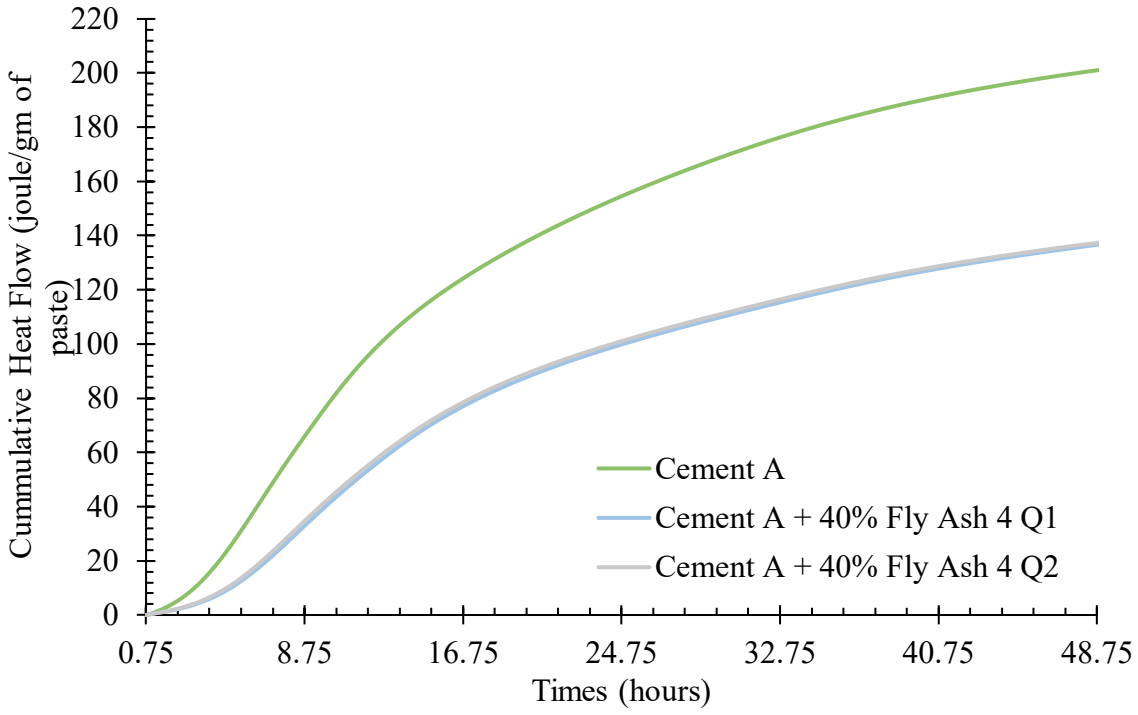

D. Fly Ash 4

Figure 23. Graphs. Cumulative heat flow for 40% weight replacement of cement with (a) Fly Ash 1, (b) Fly Ash 2, (c) Fly Ash 3, and (d) Fly Ash 4 for two quarterly samples in 2019 (Q1 and Q2).

Table 9. Setting Time Variation in Two Quarterly Samples

		Initial Setting Time (hr)	Final Setting Time (hr)
Control		3.3	6.5
Fly Ash 1	Q1	6.8	10.9
	Q2	7.0	11
Fly Ash 2	Q1	7.7	11.6
	Q2	7.2	11.2
Fly Ash 3	Q1	5.9	9.8
	Q2	5.6	9.2
Fly Ash 4	Q1	4.8	8.4
	Q2	4.7	8.2

Effect of Different Cements

Figure 24 presents the heat flow rate for a blend of 40% fly ash and 60% Portland cement for two cement sources (Cement A and Cement B) used in Illinois. The heat flow rates of the blended systems were lower than the 100% Portland cement system for the first 10 hours of hydration because C-S-H nucleation occurs during that period. Because fly ash does not contain tricalcium silicate as the dominant phase, HVFAC produces lower C-S-H in the early period. In terms of sulfate imbalance, Cement B is considered a more well-sulfated system compared to Cement A, as Peak 1 and Peak 2 are closer for Cement B (Figure 24). The setting times of the Cement B mixes were about 1–3 hours longer compared to the Cement A mixes (Table 10). The cumulative heat release after 48 hours was 67%–68% of the control for all HVFAC mixes with Cement B, whereas it was 68%–71.5% for Cement A HVFAC mixes.

Table 10. Setting Times of HVFA Mixes with Different Cements

		Initial Setting Time (hr)	Final Setting Time (hr)
Control	Cement A	3.3	6.5
	Cement B	5.2	9.5
Fly Ash 1	Cement A	7.0	11.0
	Cement B	9.1	12.6
Fly Ash 2	Cement A	7.2	11.2
	Cement B	9.4	12.6
Fly Ash 3	Cement A	5.6	9.2
	Cement B	6.6	11.4
Fly Ash 4	Cement A	4.7	8.2
	Cement B	6.4	10.4

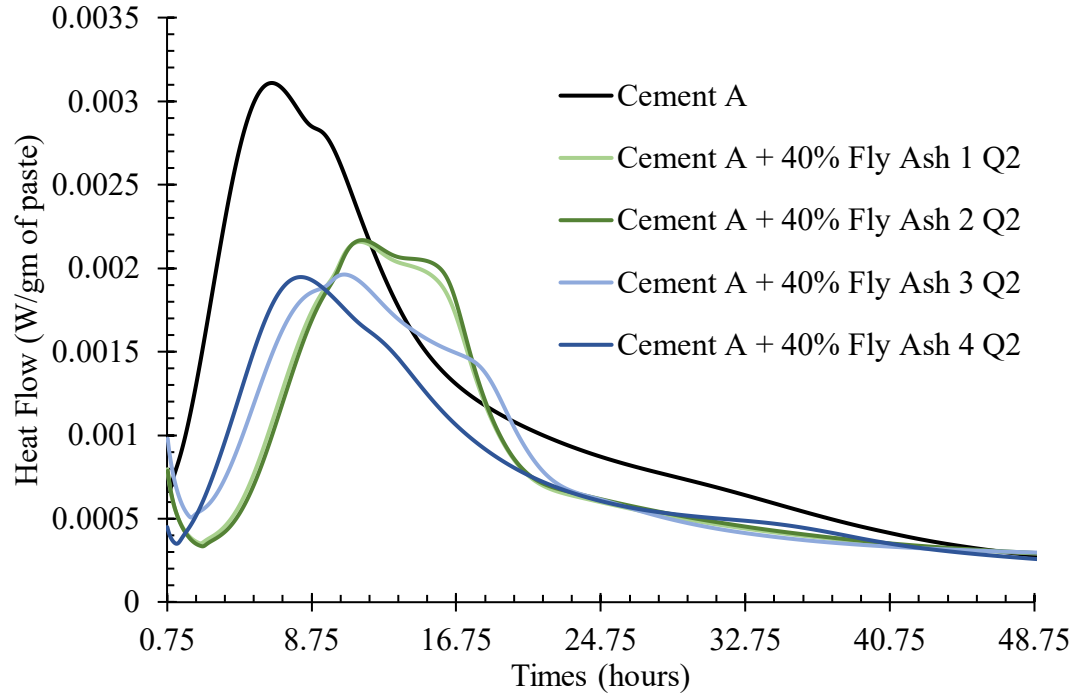

A. Cement A

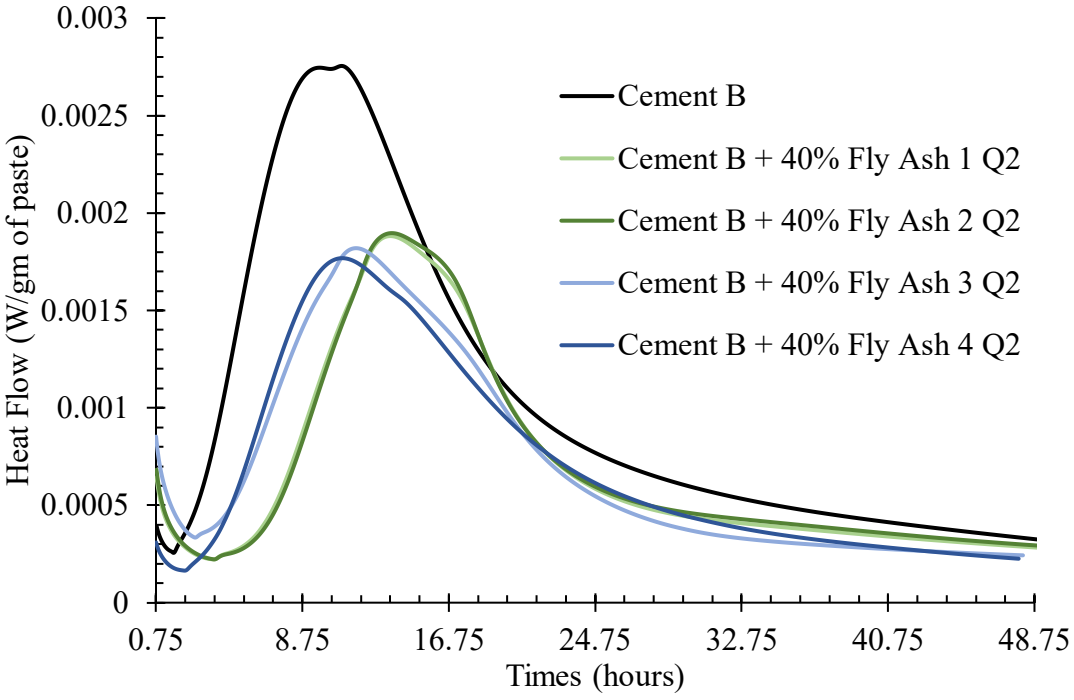

B. Cement B

Figure 24. Graphs. Heat flow rates for (a) Cement A and (b) Cement B replaced with 40% Class C (Fly Ash 1, Fly Ash 2, Fly Ash 3) and Class F (Fly Ash 4) fly ash sources for 2019 Quarter 2 samples.

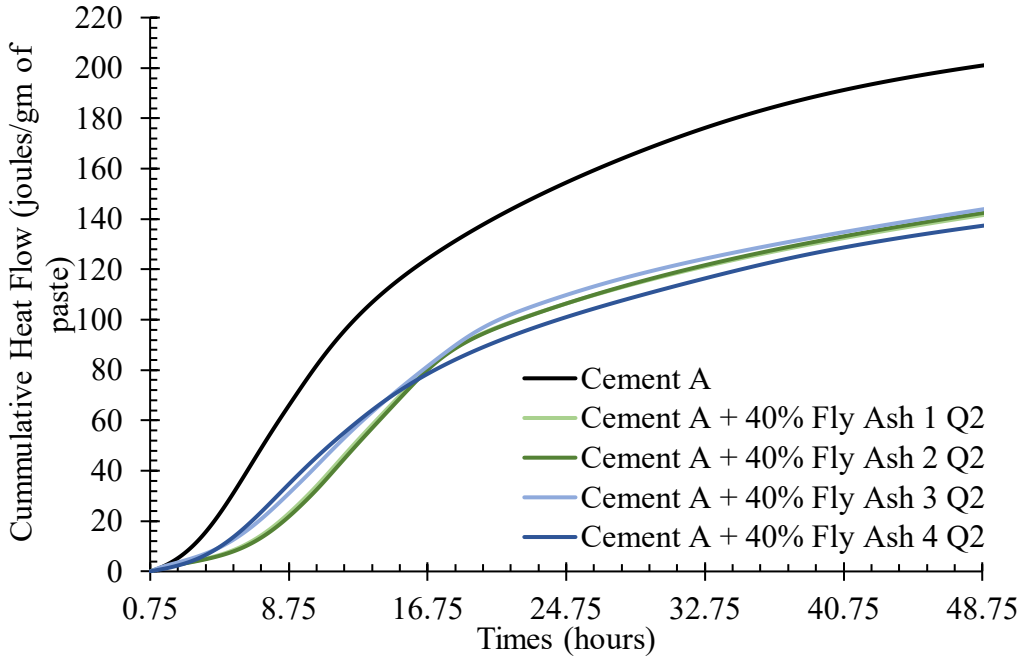

A. Cement A

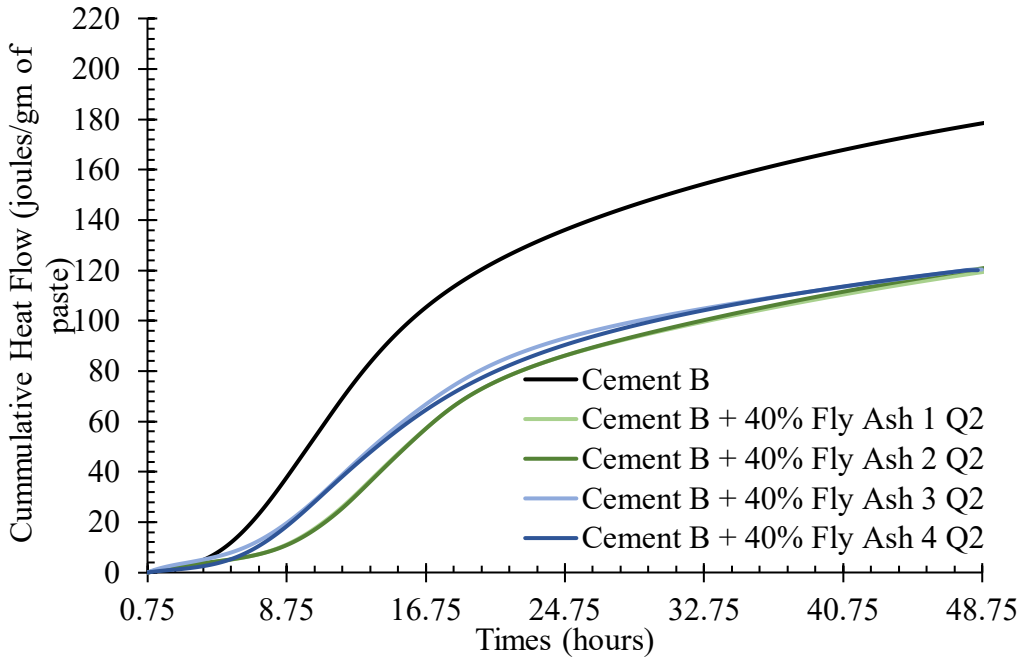

B. Cement B

Figure 25. Graphs. Cumulative heat flow for (a) Cement A and (b) Cement B replaced with 40% Class C (Fly Ash 1, Fly Ash 2, Fly Ash 3) and Class F (Fly Ash 4) fly ash sources for 2019 Quarter 2 samples.

Effect of Chemical Admixtures

Chemical admixtures are used in concrete to provide workability as well as accelerate or retard the hydration reaction. In this report, the effect of a water reducer (WRDA 82) and a superplasticizer

(ADVA Cast 600) that improve workability of HVFAC mixes was studied. The middle point of the dosage recommended by the manufacturer (300 mL/100 [4.6 oz/100 lb] kg binder for both the superplasticizer and water reducer) was used for the calorimeter tests. The superplasticizer was a polycarboxylate ether (PCE based), whereas the water reducer was lignosulfonate based. PCE- and lignosulfonate-based admixtures provide workability using two mechanisms. The lignosulfonate salt dissolves in water and releases a cation, making the admixture molecule negatively charged. The negatively charged lignosulfonate gets attached to cement particles through electrostatic force and makes all the cement particles negatively charged and thus minimize flocculation. In contrast, PCE-based admixture molecules have a large negatively charged backbone with shorted sidechains. The PCE backbone is adsorbed on the cement grains (especially on the aluminate phases as they are positively charged), and the sidechains stops the flocculation through steric hindrance. As steric hindrance is the major factor providing workability, PCE-based admixtures are not affected by the change in ion concentration over time and thus provide workability for a longer time compared to lignosulfonate-based admixtures.

Both the water reducer and superplasticizer delayed the hydration reaction significantly. The induction period was consistently longer for the PCE-based admixture compared to the lignosulfonate one (Figure 26), which also led to a further delay in setting times (Table 11). The setting times were delayed by 4–5 hours and 5–6 hours for the water reducer and superplasticizer usage, respectively. The peak heat flow rate also decreases significantly with chemical admixture, and the peak heat flow is generally similar for both the admixtures for Fly Ash 1, 3, and 4, but not for Fly Ash 2. The cumulative heat release after 48 hours was similar for both lignosulfonate and PCE-based admixtures, and they were about 10%–15% less than the control mix without any chemical admixtures (Figure 27).

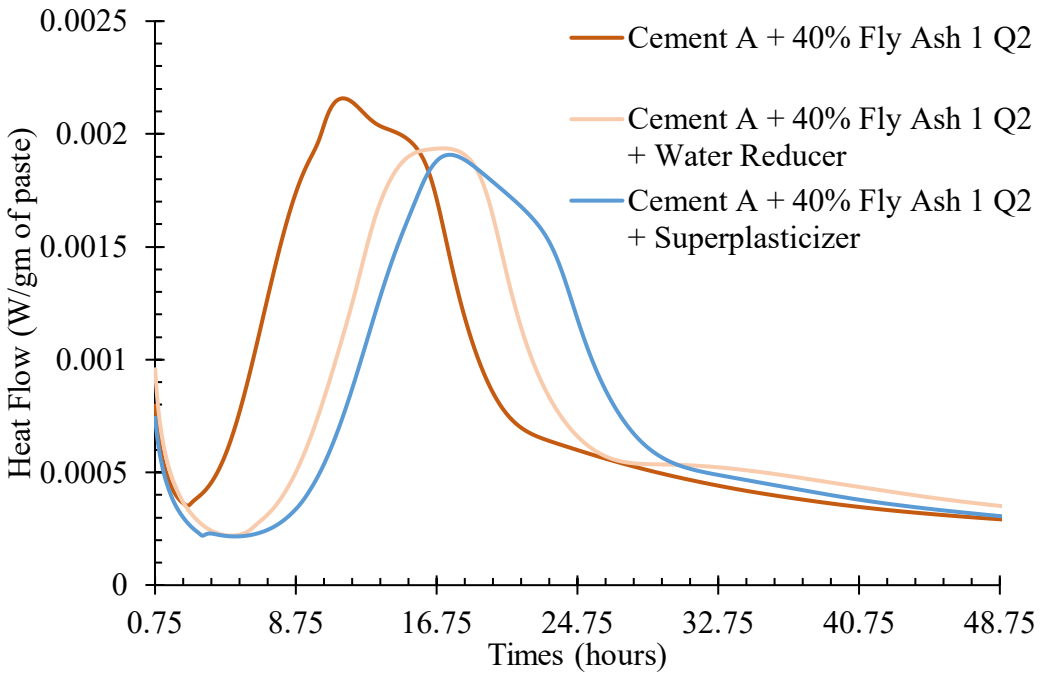

A. Fly Ash 1

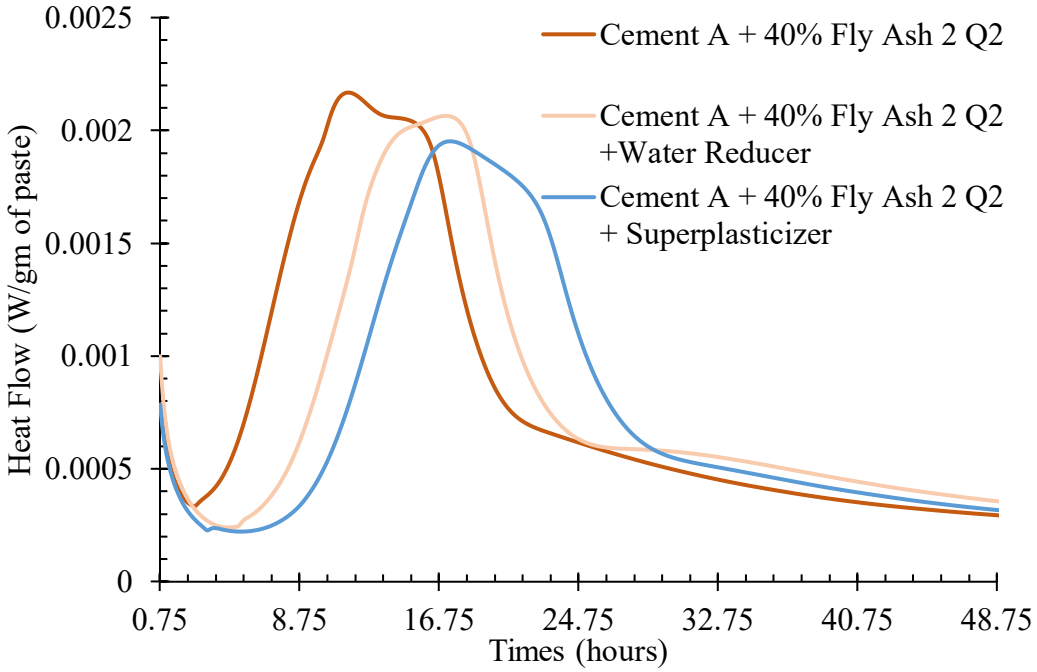

B. Fly Ash 2

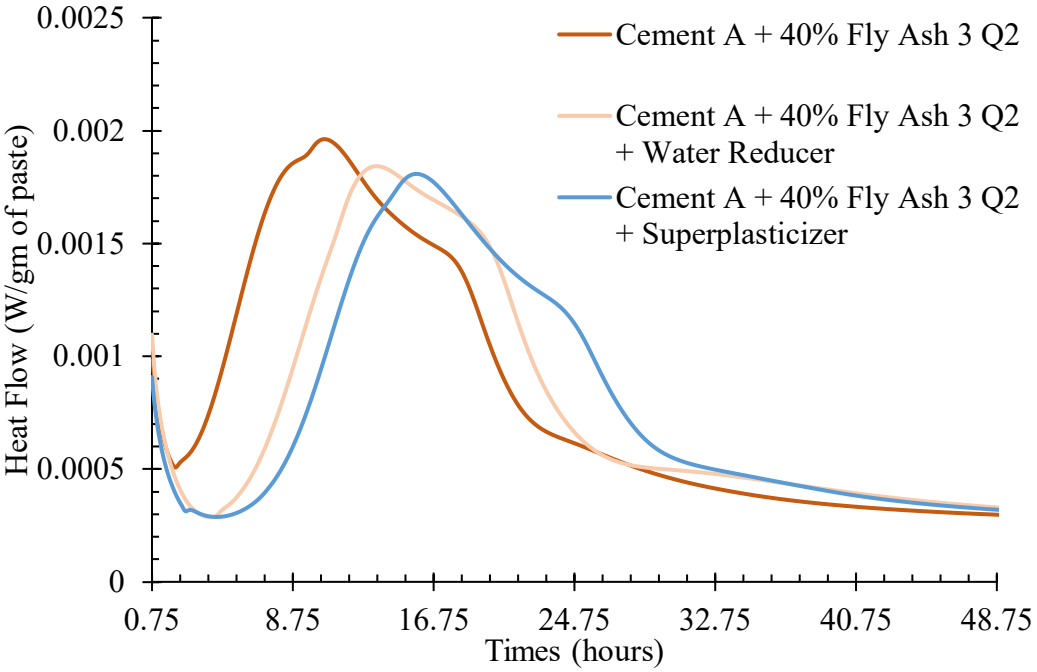

C. Fly Ash 3

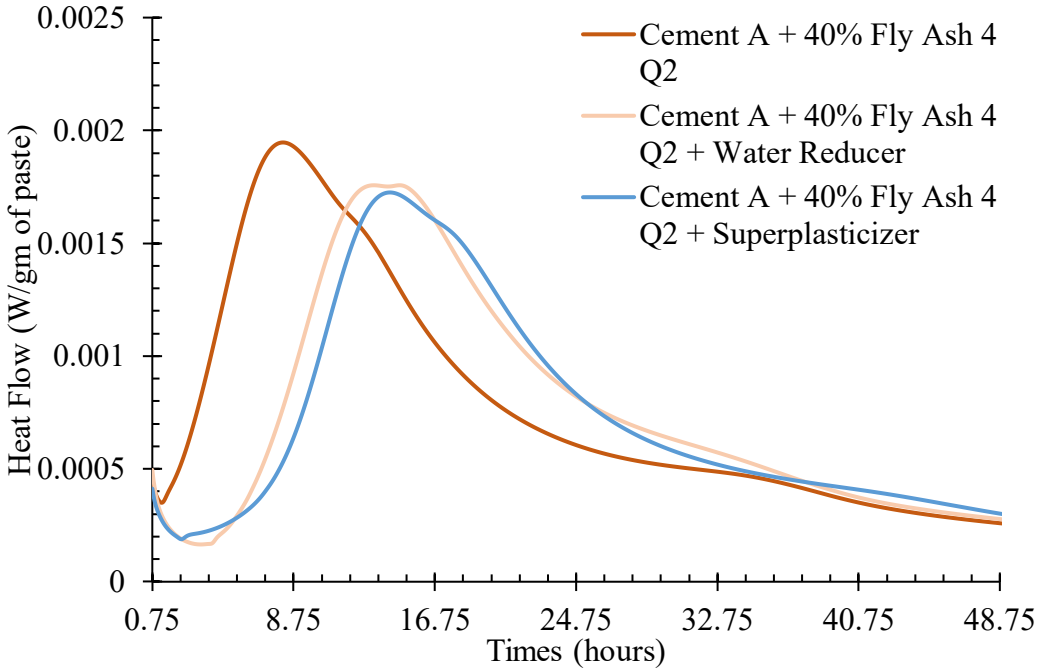

D. Fly Ash 4

Figure 26. Graphs. Effect of superplasticizer and water reducer on heat flow rates for 40% weight replacement of cement with (a) Fly Ash 1, (b) Fly Ash 2, (c) Fly Ash 3, and (d) Fly Ash 4 for 2019 Quarter 2 samples.

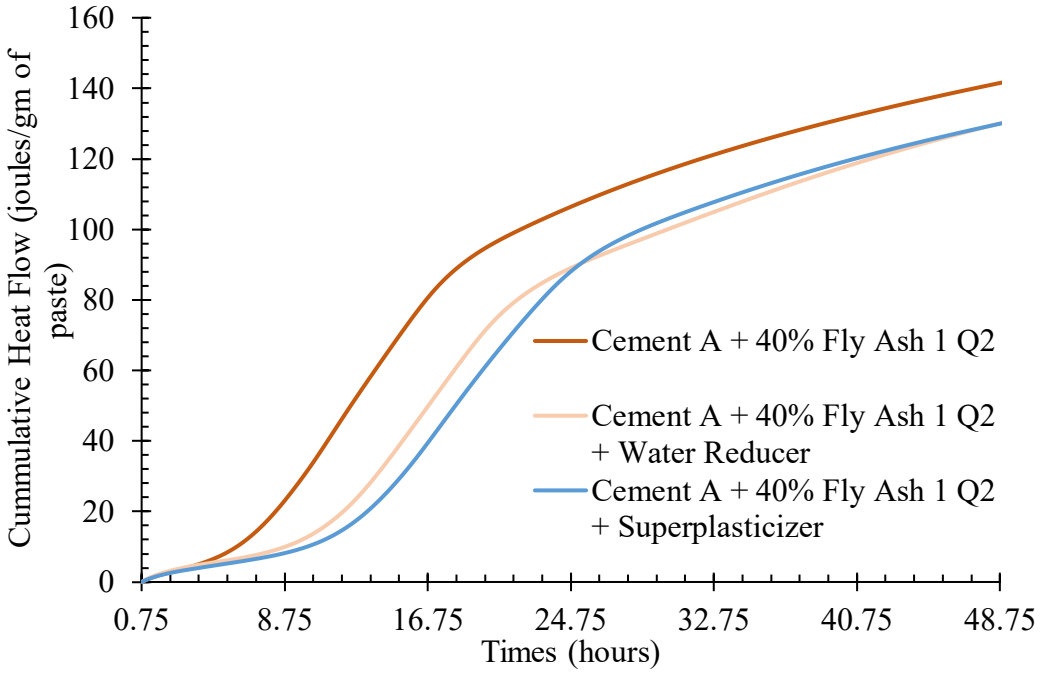

A. Fly Ash 1

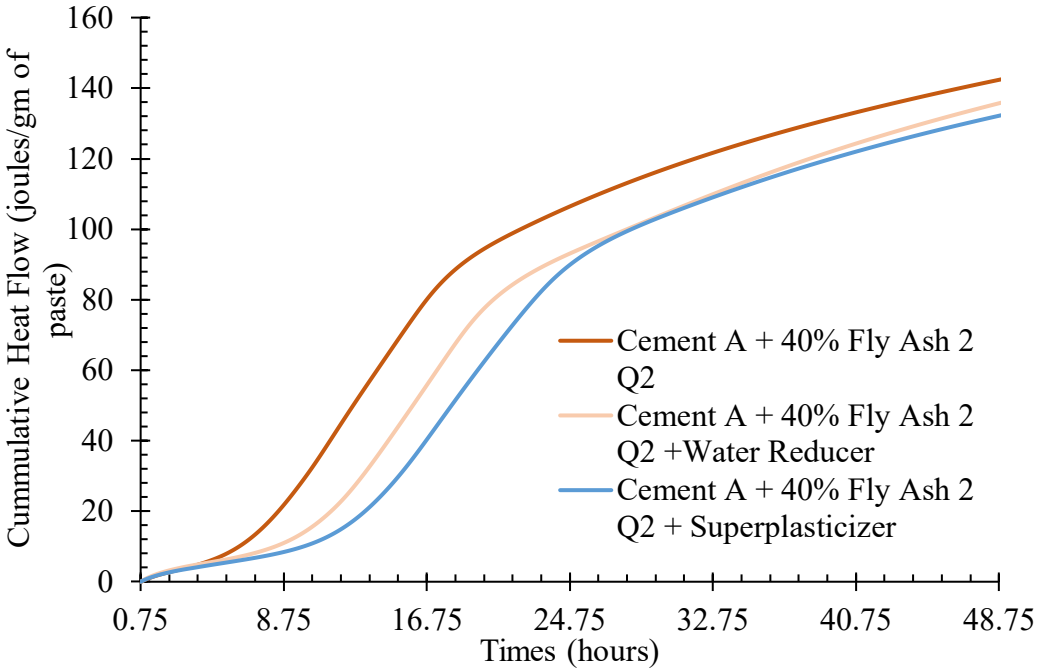

B. Fly Ash 2

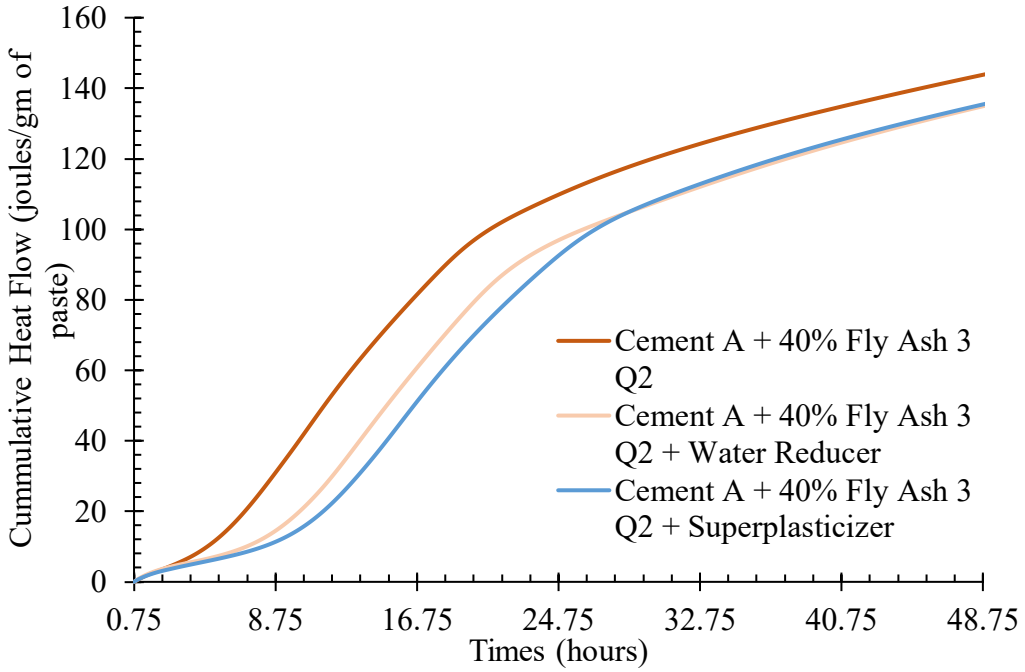

C. Fly Ash 3

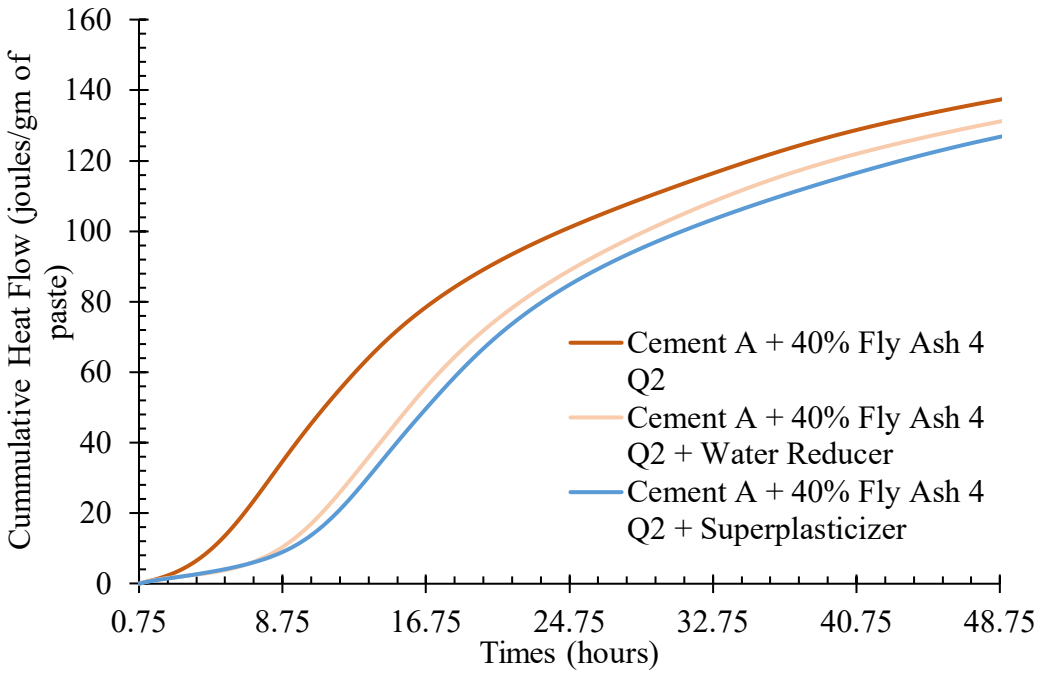

D. Fly Ash 4

Figure 27. Graphs. Effect of superplasticizer and water reducer on cumulative heat flow for 40% weight replacement of cement with (a) Fly Ash 1, (b) Fly Ash 2, (c) Fly Ash 3, and (d) Fly Ash 4 for 2019 Quarter 2 samples.

Table 11. Effect of Chemical Admixtures on Setting Times of HVFAC (Cement A + 40% fly ash)

		Initial Setting Time (hr)	Final Setting Time (hr)
Fly Ash 1	Control	7.0	11.0
	Water Reducer	12.4	15.1
	Superplasticizer	13.0	17.0
Fly Ash 2	Control	7.2	11.2
	Water Reducer	12.0	14.6
	Superplasticizer	13.0	17.1
Fly Ash 3	Control	5.6	9.2
	Water Reducer	9.3	13.2
	Superplasticizer	11.1	15.3
Fly Ash 4	Control	4.7	8.2
	Water Reducer	9.7	13.1
	Superplasticizer	10.6	14.0

EFFECT OF LIMESTONE REPLACEMENT

Limestone is a commonly available material used in cement production and directly as coarse aggregates in concrete. Even though limestone is generally considered an inert material, it can react with the aluminate phases and form monocarbonate and hemicarbonates. In this project, addition of

limestone powder (micro and nano) to accelerate the setting times have been investigated. Nanomaterials offer a very high specific surface area and provide nucleation sites for calcium silicate hydrate precipitation. Thus, nano-limestone is expected to affect the hydration reaction rate of HVFAC more than the addition of micro-limestone (Bentz 2011).

Straight Cement Mixes—Micro- vs. Nano-limestone

For all the mixes, nano-limestone replacement was much more effective in accelerating the setting times compared to micro-limestone (Table 12). Replacing cement by 5% nano-limestone accelerated the initial setting time significantly—the straight cement mix had an initial setting time of 3.3 hours, whereas the initial setting time with 5% nano-limestone replacement was only 1.8 hours. Increasing nano-limestone dosage beyond 5% accelerated the final setting time, whereas the initial setting time did not change significantly. Micro-limestone replacement also accelerated the setting time, but not as much as nano-limestone replacement. The peak heat flow of the nano-limestone-replaced mixes were higher than the straight cement mix and the micro-limestone mix except for the 10% nano-limestone mix (Figure 28). The heat flow measured after 20 hours of hydration decreased with increasing limestone content because of the dilution of cement in the total paste volume.

The cumulative heat flow after 48 hours decreased with increasing limestone replacement, and the there was no apparent effect of limestone powder particle size on 48-hour cumulative heat flow values (Figure 48). Mixes with 5% limestone replacement had a higher cumulative heat flow than the straight cement mix.

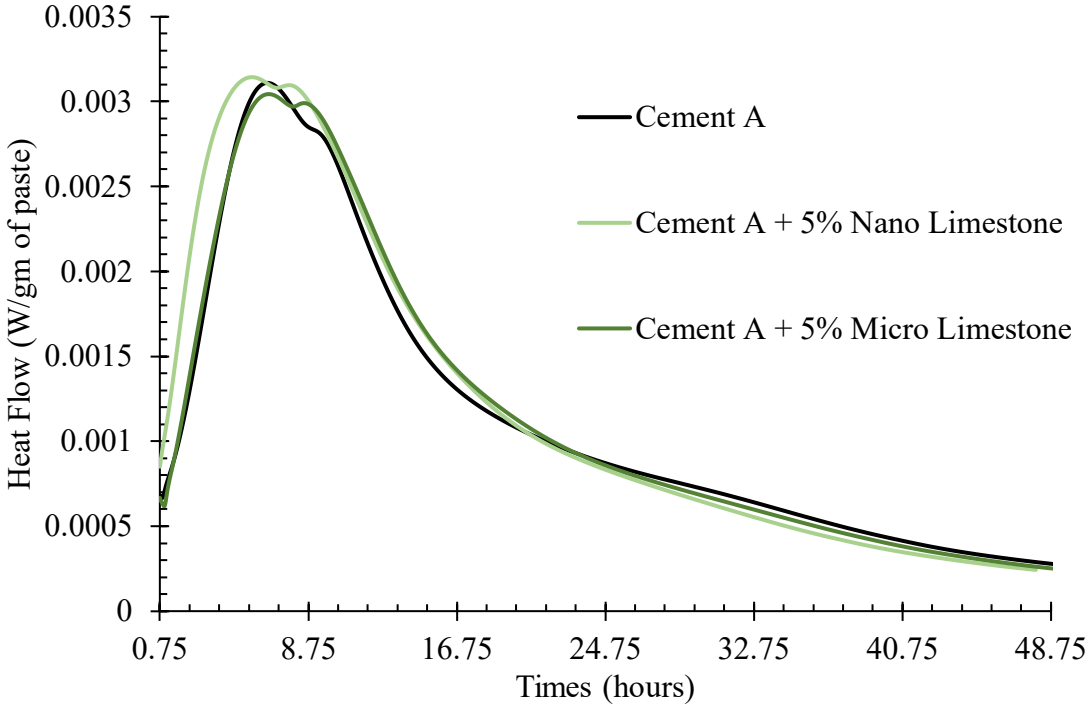

A. 5% replacement

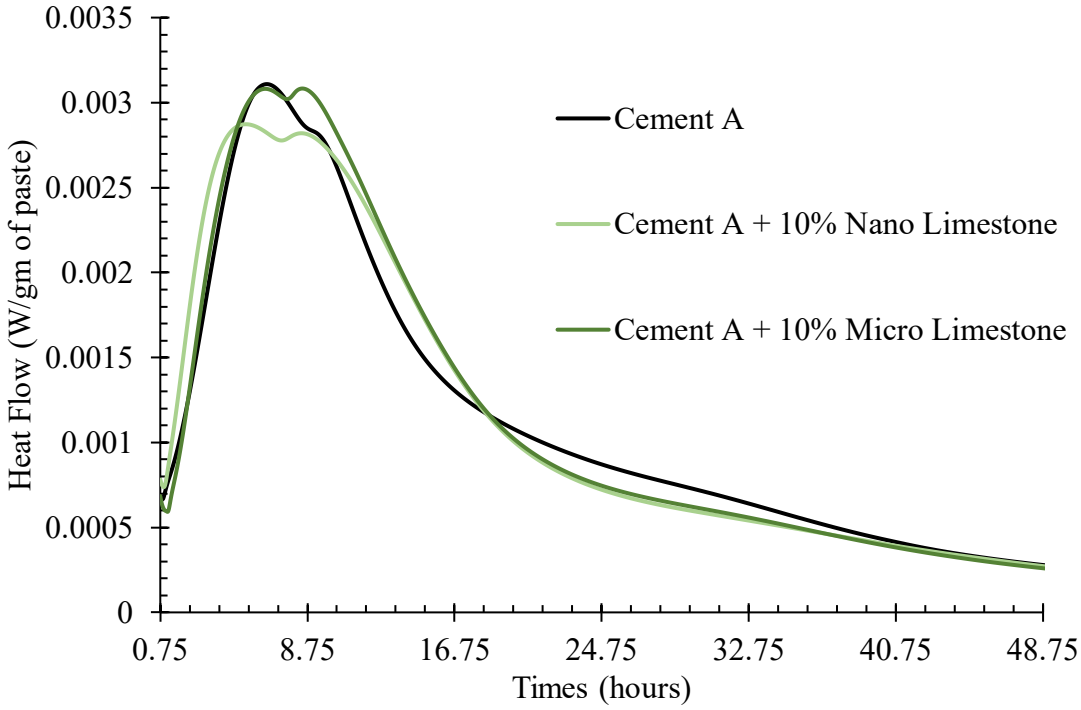

B. 10% replacement

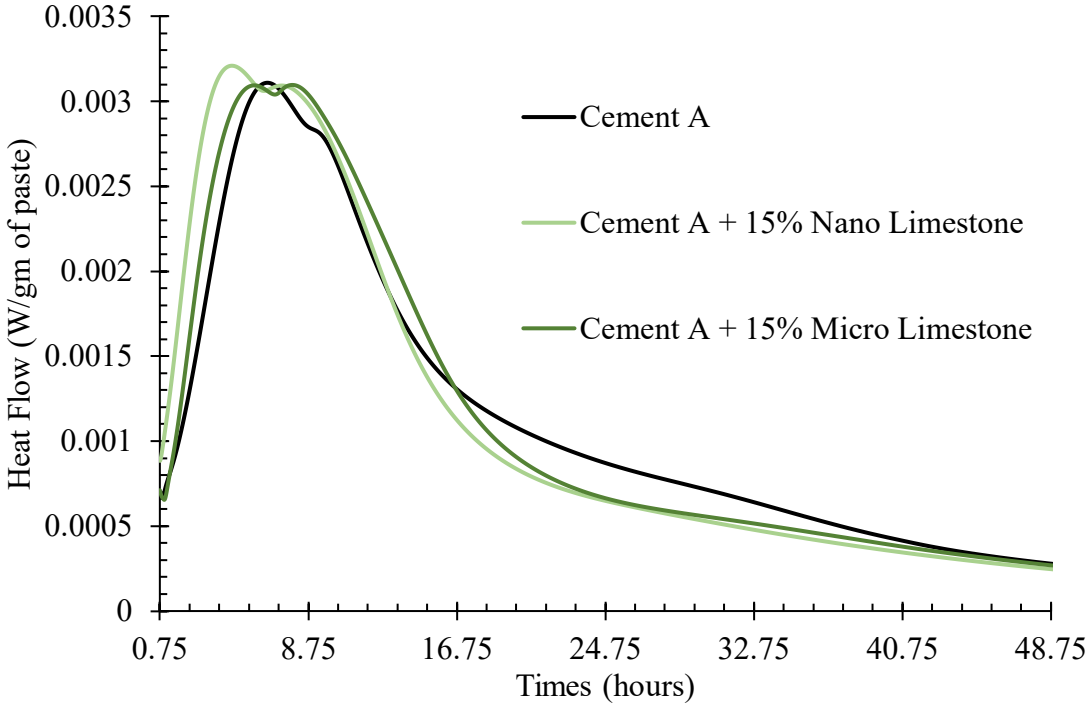

C. 15% replacement

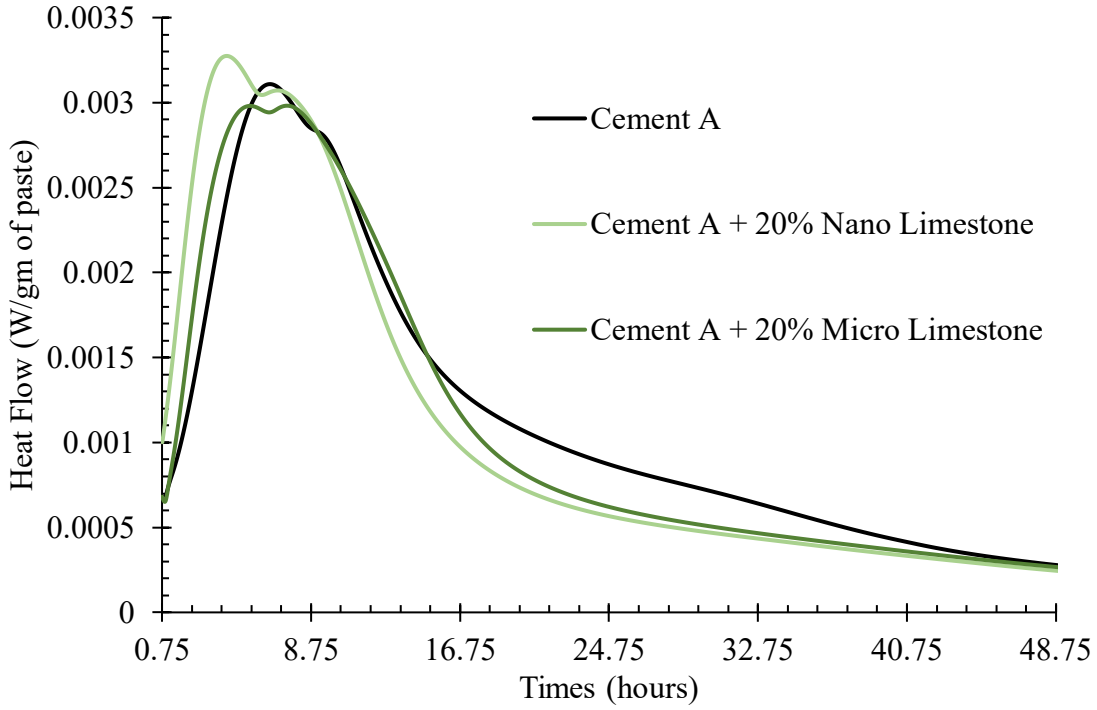

D. 20% replacement

Figure 28. Graphs. Effect of micro- and nano-limestone replacement on heat flow rates for different cement replacement rates of (a) 5%, (b) 10%, (c) 15%, and (d) 20%.

Table 12. Effect of Micro- and Nano-limestone Replacement in Straight Cement Mixes

Limestone Content (%)	Limestone Type	Initial Setting Time (hr)	Final Setting Time (hr)
0	Control	3.3	6.5
5	Micro-limestone	2.4	6.6
	Nano-limestone	1.8	5.8
10	Micro-limestone	2.5	6.5
	Nano-limestone	2.0	4.7
15	Micro-limestone	2.4	5.8
	Nano-limestone	1.9	4.6
20	Micro-limestone	2.1	5.4
	Nano-limestone	1.7	4.2

HVFAC Mixes—Micro- vs. Nano-limestone

For HVFAC mixes, nano-limestone replacement was more effective in accelerating the setting times compared to micro-limestone, similar to straight cement mixes (Table 13). Increasing nano-limestone addition to 10% for Fly Ash 1 decreased the initial and final setting times by 3.2 and 2.7 hours, respectively. The set time acceleration was slightly lower for the system with 40% Fly Ash 4 (Class F)

and 10% nano-limestone as initial and final setting times were 2.3 and 2.5 hours faster, respectively. In fact, nano-limestone was more effective in accelerating setting time in HVFAC systems compared to straight cement systems. Replacement of Cement A with 10% nano-limestone accelerated the initial and final setting times by only 1.3 and 1.8 hours, respectively. Even micro-limestone was more effective in accelerating setting times in HVFAC systems compared to the straight cement system, though the absolute decrease in setting times was lower in case of micro-limestone compared to nano-limestone.

In the case of Class F fly ash (Fly Ash 4) replacement, the relative shape of Peak 1 and Peak 2 in the heat flow curve did not change significantly with limestone replacement (Figure 29 and Figure 30). However, for Class C fly ash, the heat flow of Peak 2 increases significantly compared to the heat flow of Peak 1, when limestone replaced cement by more than 10% of the total binder. Fly ash does not contain a significant amount of calcium sulfate, but Class C ash can have a significant amount of tricalcium aluminates. When increasing the amount of limestone replacing the cement while keeping the fly ash amount constant, the amount of calcium sulfate in the system decreases faster than the decrease in the amount of tricalcium aluminate, leading to a higher tricalcium aluminate-to-calcium sulfate ratio.

The cumulative heat released after 48 hours decreased with increasing limestone replacement (Figure 49 and Figure 50). For Fly Ash 2 and 4, the cumulative heat flow after 48 hours increased when 5% of the cement was replaced with nano-limestone, but for micro-limestone replacement, the cumulative heat released after 48 hours was always lower than the control mix.

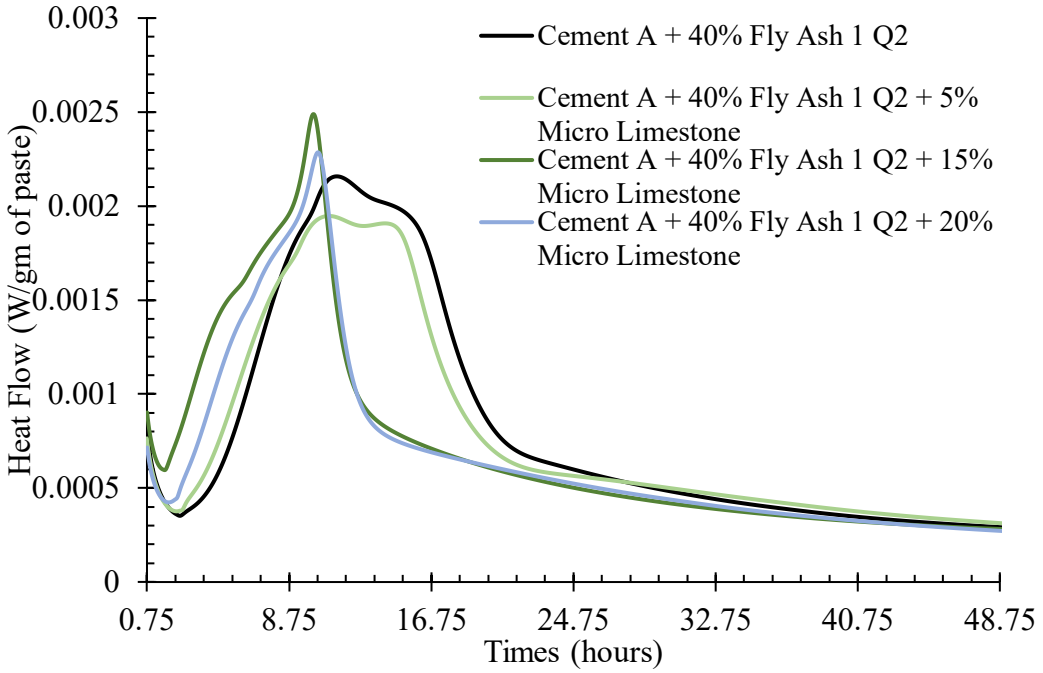

A. Fly Ash 1

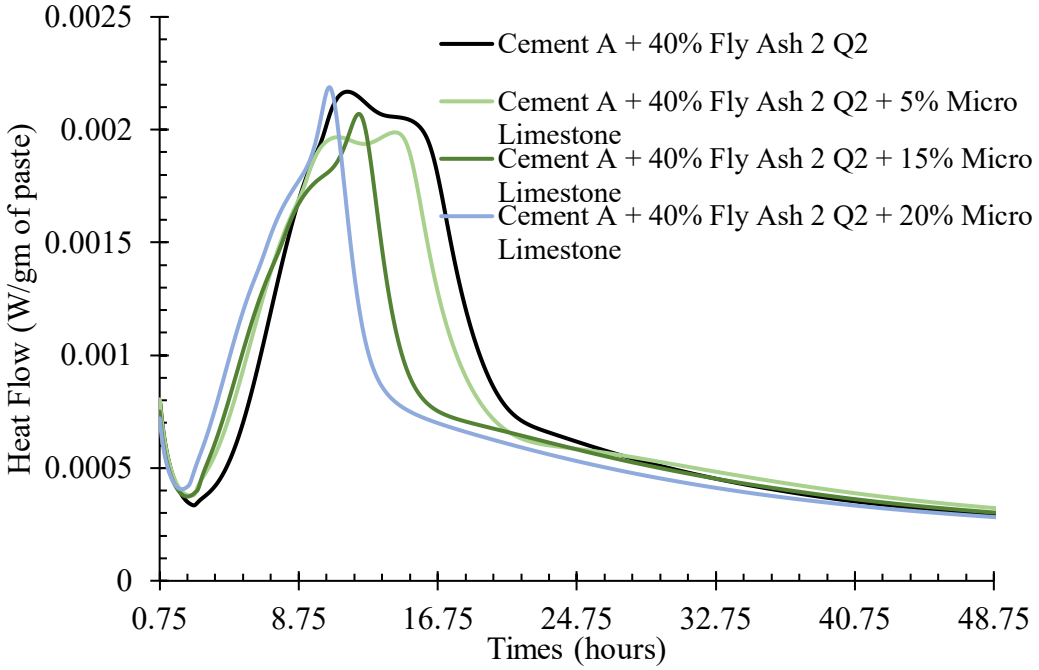

B. Fly Ash 2

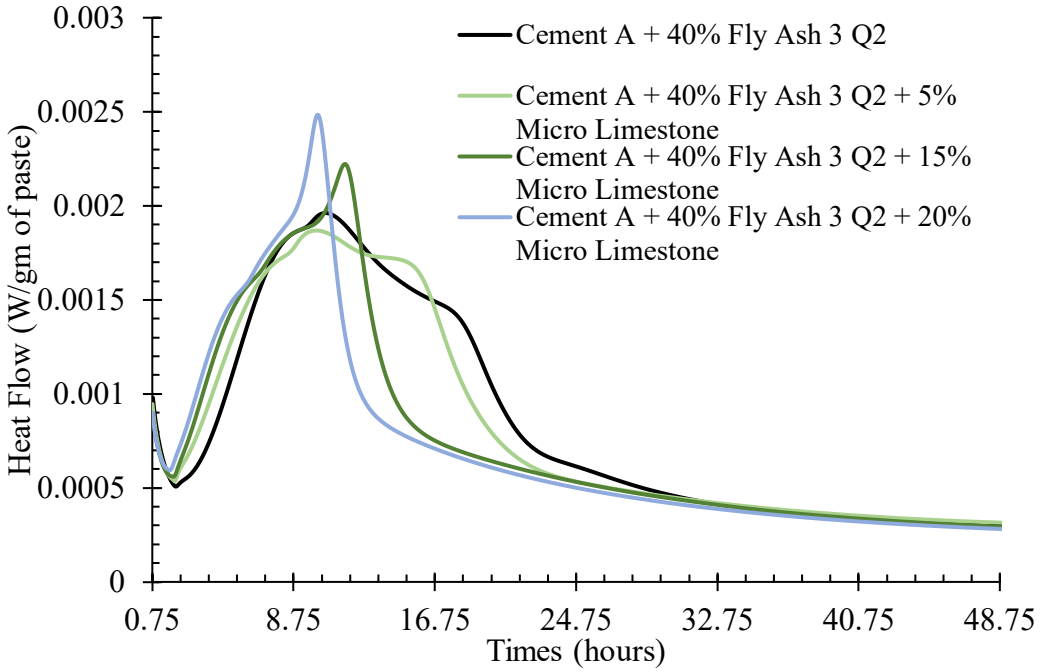

C. Fly Ash 3

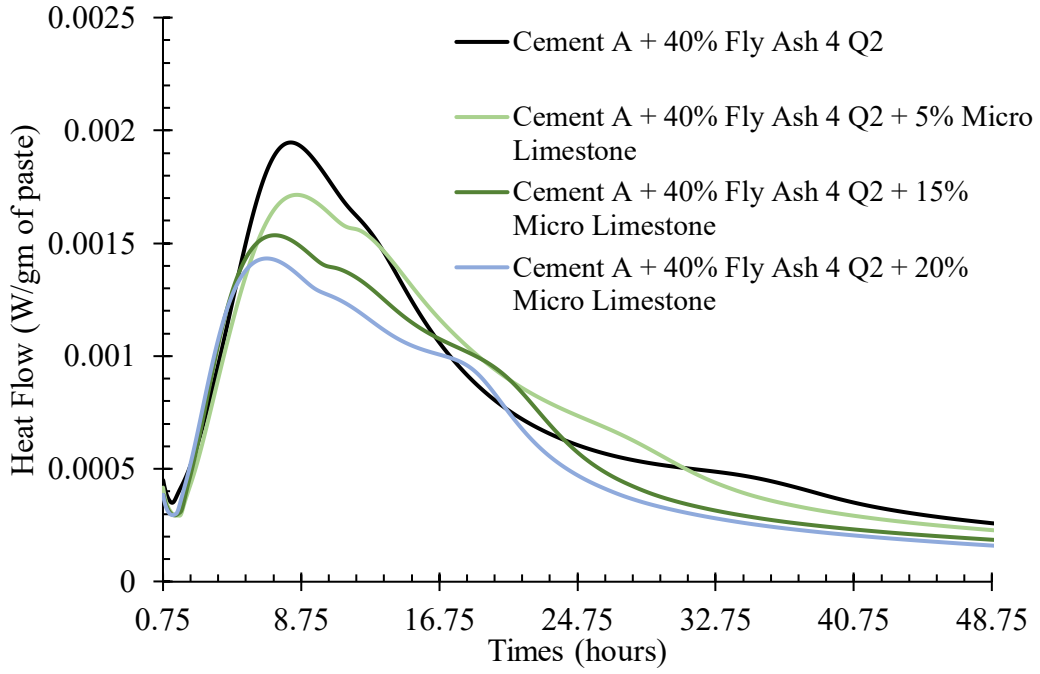

D. Fly Ash 4

Figure 29. Graphs. Effect of increasing micro-limestone replacement on heat flow rates for 40% weight replacement of cement with (a) Fly Ash 1, (b) Fly Ash 2, (c) Fly Ash 3, and (d) Fly Ash 4 for 2019 Quarter 2 samples.

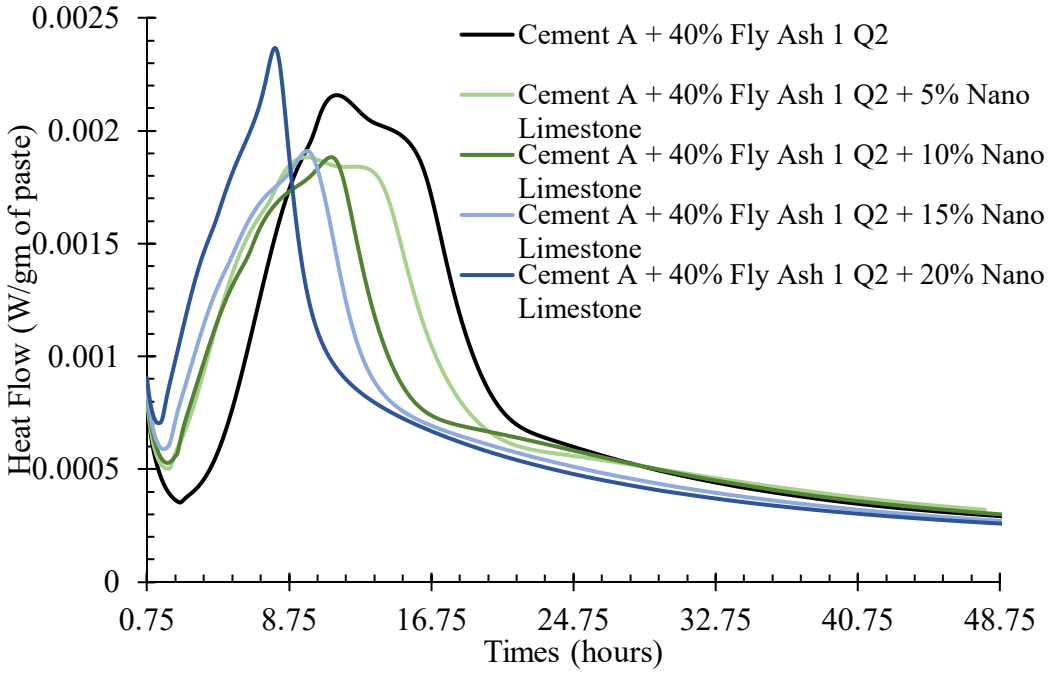

A. Fly Ash 1

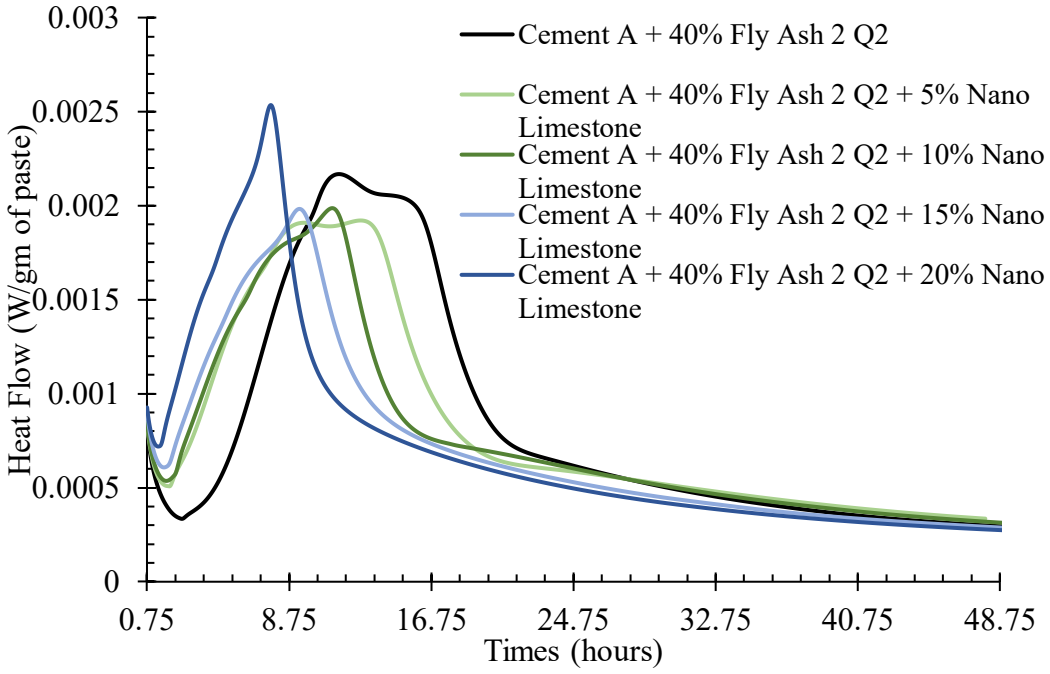

B. Fly Ash 2

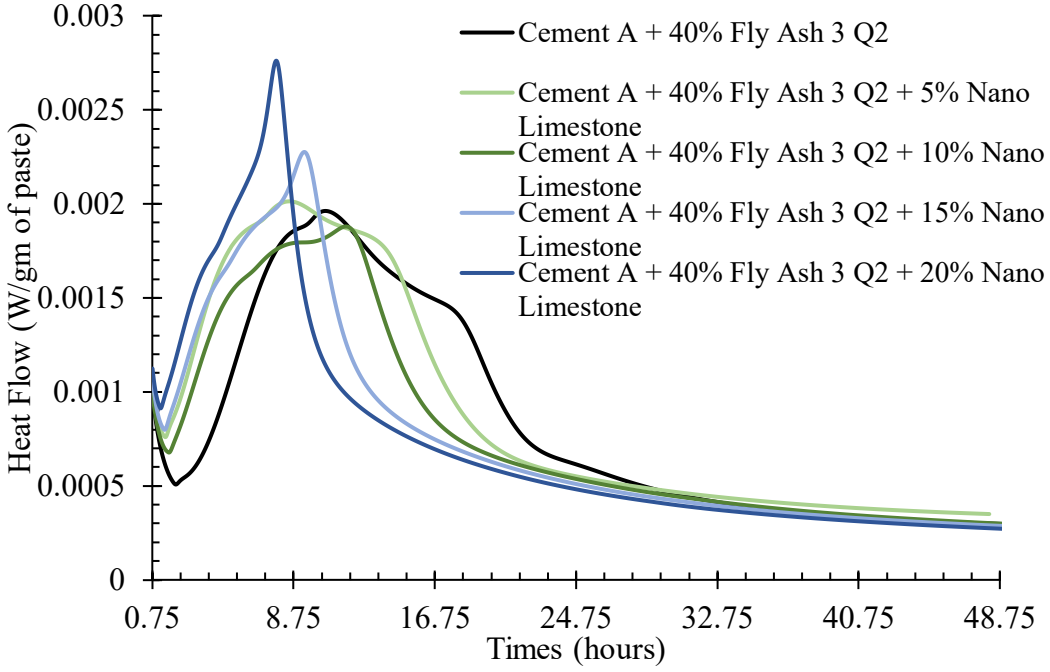

C. Fly Ash 3

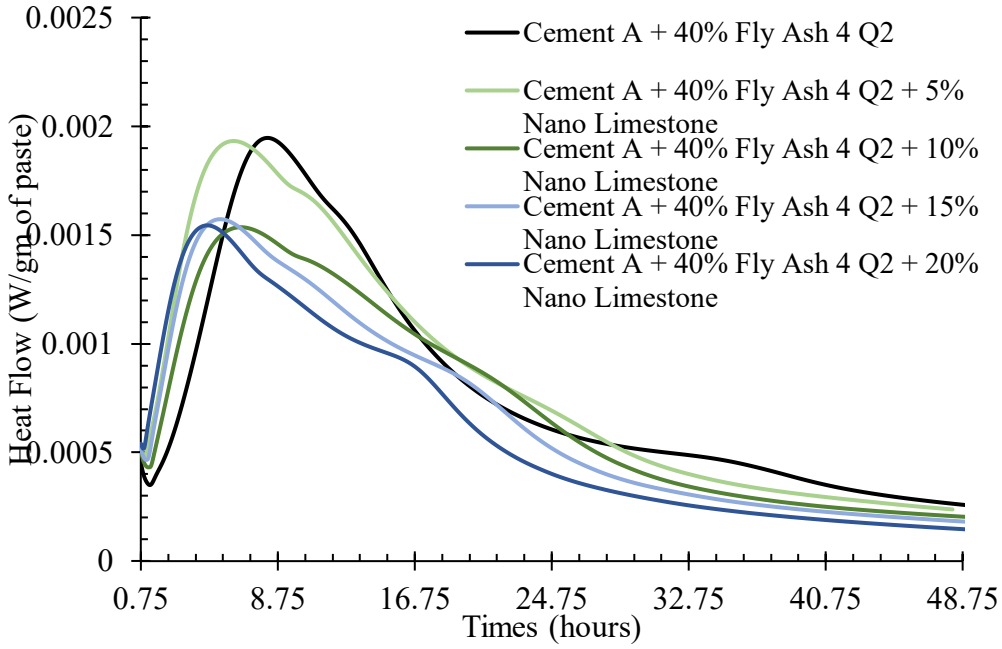

D. Fly Ash 4

Figure 30. Graphs. Effect of increasing nano-limestone replacement on heat flow rates for 40% weight replacement of cement with (a) Fly Ash 1, (b) Fly Ash 2, (c) Fly Ash 3, and (d) Fly Ash 4 for 2019 Quarter 2 samples.

Table 13. Effect of Limestone Replacement of Cement on Setting Time of HVFAC

		Micro-limestone		Nano-limestone	
		Initial Setting Time (hr)	Final Setting Time (hr)	Initial Setting Time (hr)	Final Setting Time (hr)
Fly Ash 1	0%	7.0	11.0	7.0	11.0
	5%	5.8	9.3	4.2	9.0
	10%	–	–	3.7	8.3
	15%	3.3	6.0	2.2	7.6
	20%	4.3	6.5	1.8	5.9
Fly Ash 2	0%	7.2	11.2	7.2	11.2
	5%	5.8	10.6	4.5	9.4
	10%	–	–	2.5	8.8
	15%	5.2	9.3	2.2	7.7
	20%	4.5	7.9	1.7	6.0
Fly Ash 3	0%	5.6	9.2	5.6	9.2
	5%	4.3	8.8	3.1	6.9
	10%	–	–	3.1	6.5
	15%	3.6	6.8	2.6	5.6
	20%	3.3	6.3	2.3	4.4
Fly Ash 4	0%	4.7	8.2	4.7	8.2
	5%	3.7	8.4	2.4	6.1
	10%	–	–	2.3	5.9
	15%	3.3	7.2	1.3	5.2
	20%	3.0	6.7	1.1	4.7

Effect of Chemical Admixtures on HVFAC with Micro-limestone

Chemical admixtures had a strong retarding effect on hydration and setting times of HVFAC. Limestone replacement was found to be useful in accelerating the setting times in the previous section titled “HVFAC Mixes—Micro- vs. Nano-limestone.” Thus, the next step was to verify whether micro-limestone is useful in accelerating setting times of HVFAC with chemical admixtures. Even though nano-limestone is more effective in accelerating setting times, micro-limestone was used because of its higher availability and ease of use. A high limestone replacement rate can decrease the long-term strength gain, as observed from the 48-hour cumulative heat flow. As a result, only a 5% replacement of micro-limestone was used in this section. The chemical admixture dosages were kept the same as in the previous section titled “Effect of Chemical Admixtures.”

Similar to the HVFAC mixes without any limestone, the PCE-based superplasticizer increased the induction period longer than the lignosulfonate-based water reducer for the HVFAC mixes with 5% micro-limestone (Figure 31), and thus the superplasticizer mixes had longer setting times than the water-reducer ones (Table 14). The heat flow rate at Peak 1 also decreases significantly with both chemical admixtures. The cumulative heat release after 48 hours was similar for both lignosulfonate- and PCE-based admixtures, and they were about 10% less than the control mix without any chemical admixtures (Figure 32). Even though the different chemical admixtures had a retarding effect, even on HVFAC mixes with 5% micro-limestone, the micro-limestone replacement had a significant effect on accelerating the setting times by 2–3 hours compared to plain HVFAC mixes with chemical admixtures (Table 15). For Class F mixes (Fly Ash 4), the setting time acceleration due to 5% micro-limestone replacement was similar for mixes with PCE- and lignosulfonate-based admixtures. However, for Class C mixes, the acceleration was much higher in PCE-based admixture mixes compared to the lignosulfonate-based mix. Thus, micro-limestone replacement at a really low amount can be a great tool to accelerate the setting times without sacrificing long-term strength. Moreover, micro-limestone is already widely available in the United States and can be applied to high-volume, ready-mix concrete mixes.

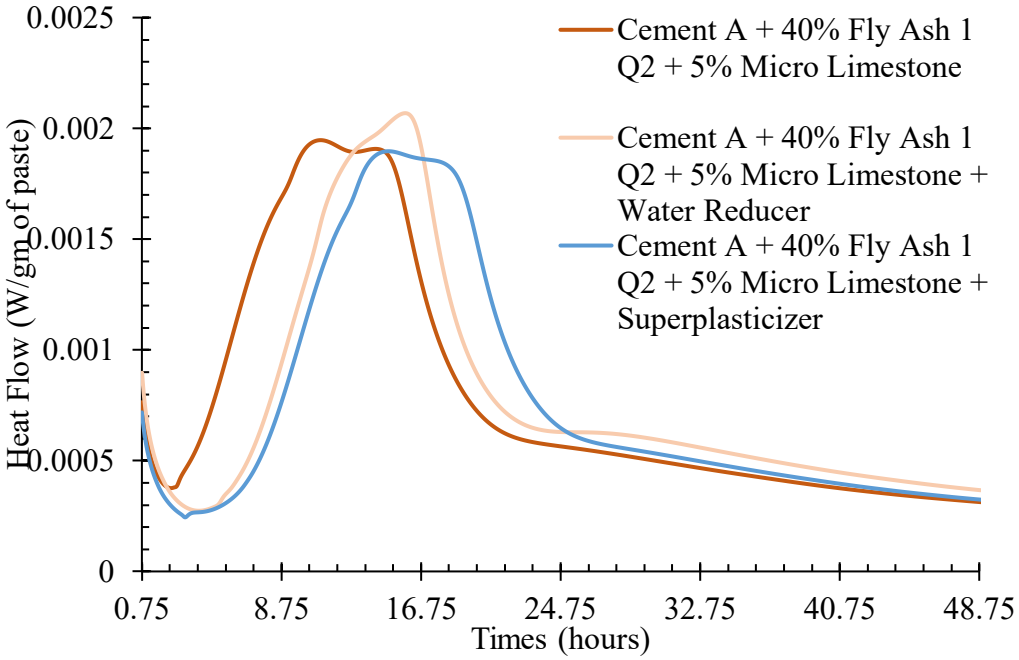

A. Fly Ash 1

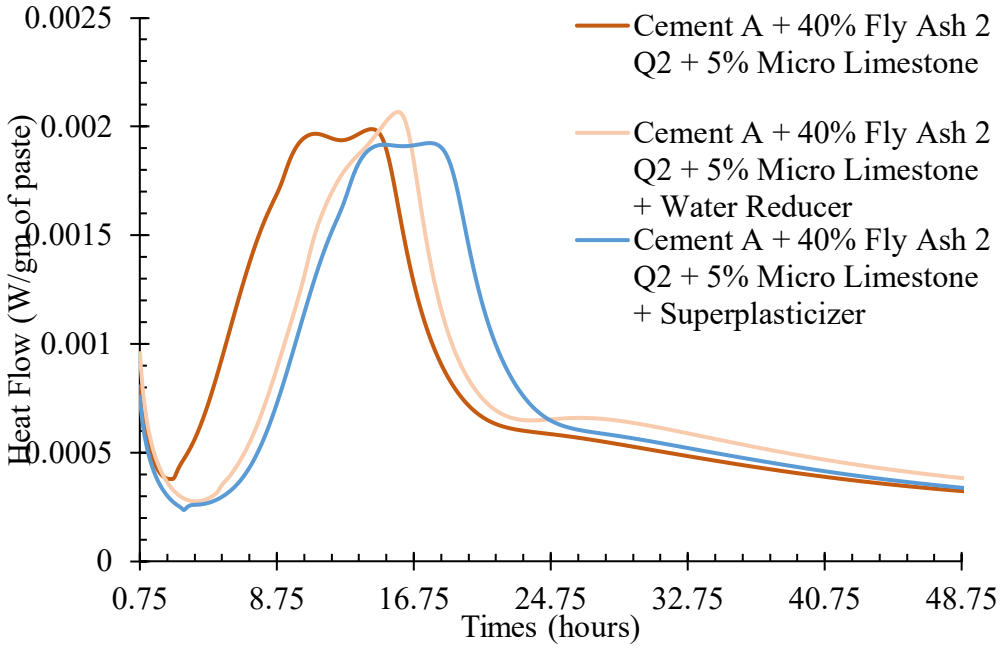

B. Fly Ash 2

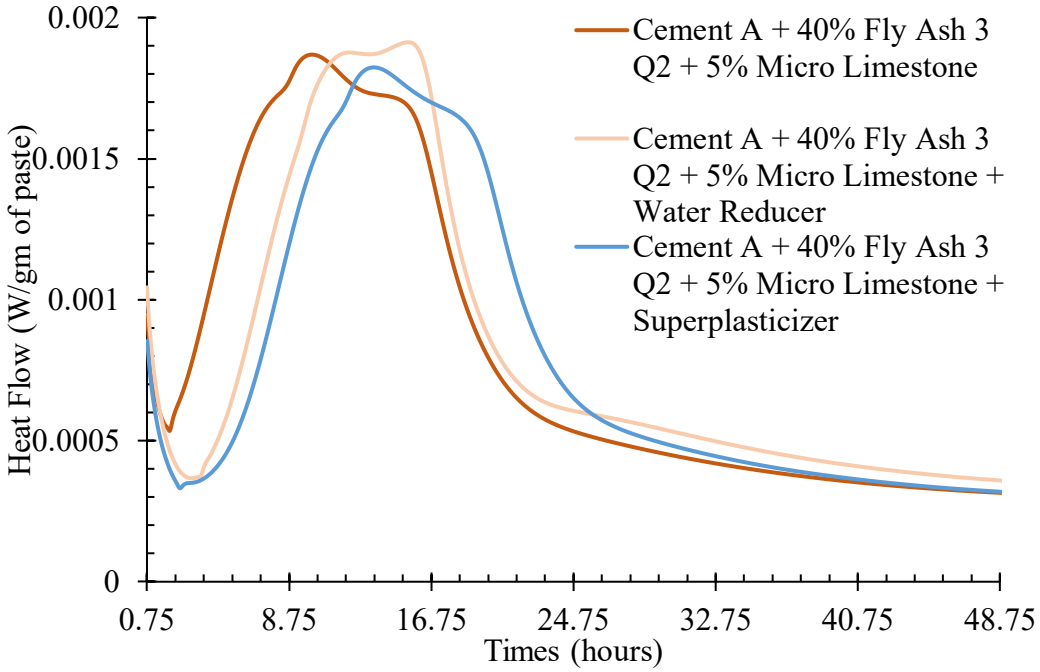

C. Fly Ash 3

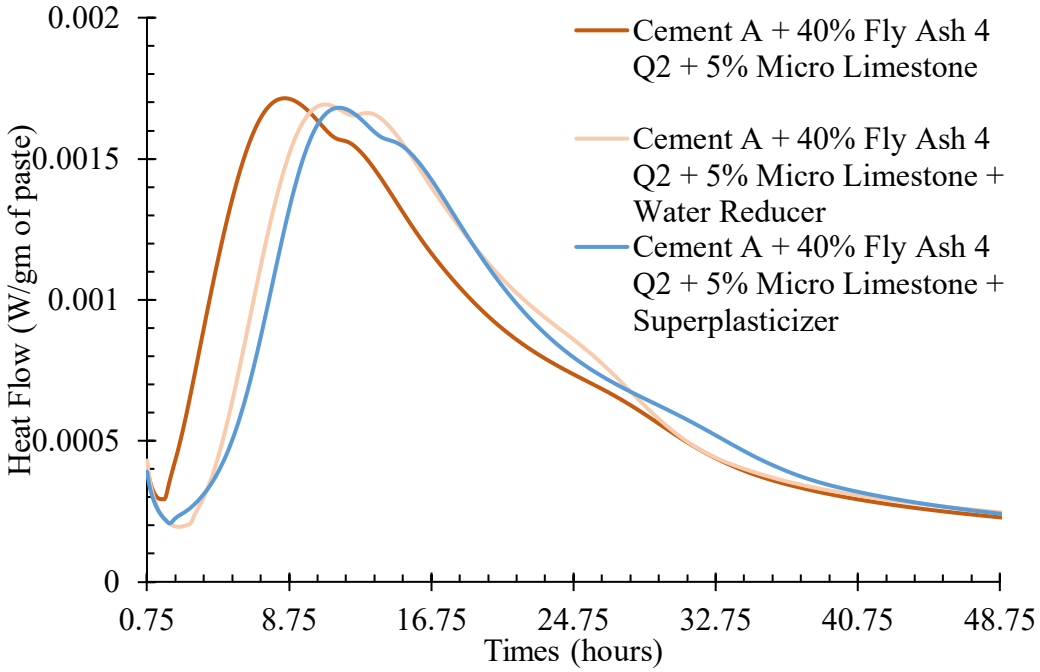

D. Fly Ash 4

Figure 31. Graphs. Effect of superplasticizer and water reducer on heat flow rates for 5% micro-limestone and 40% weight replacement of cement with (a) Fly Ash 1, (b) Fly Ash 2, (c) Fly Ash 3, and (d) Fly Ash 4 for 2019 Quarter 2 samples.

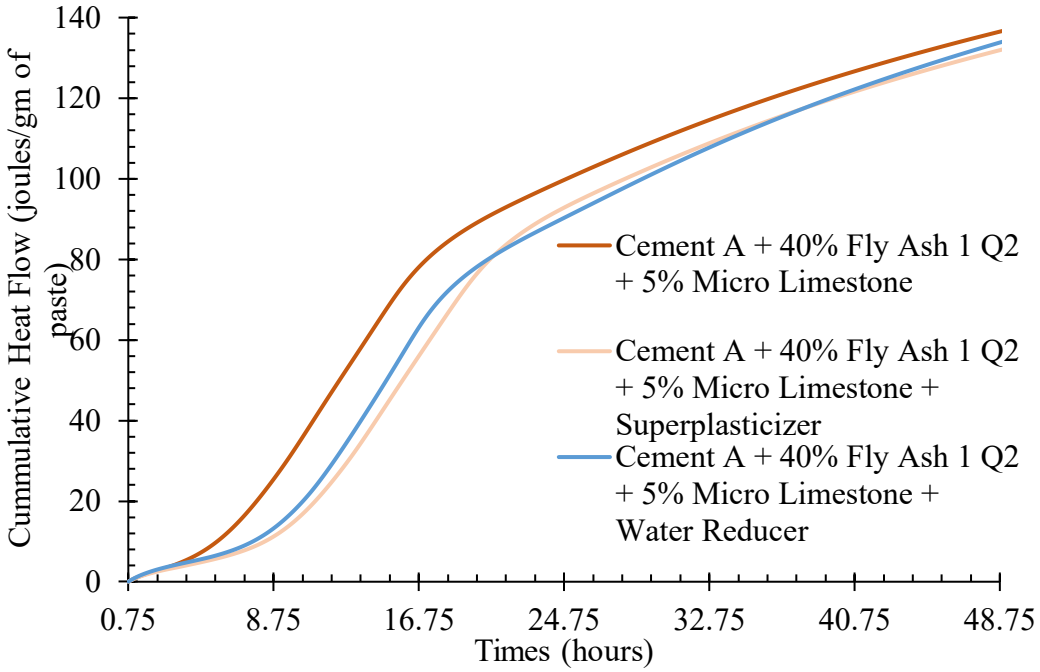

A. Fly Ash 1

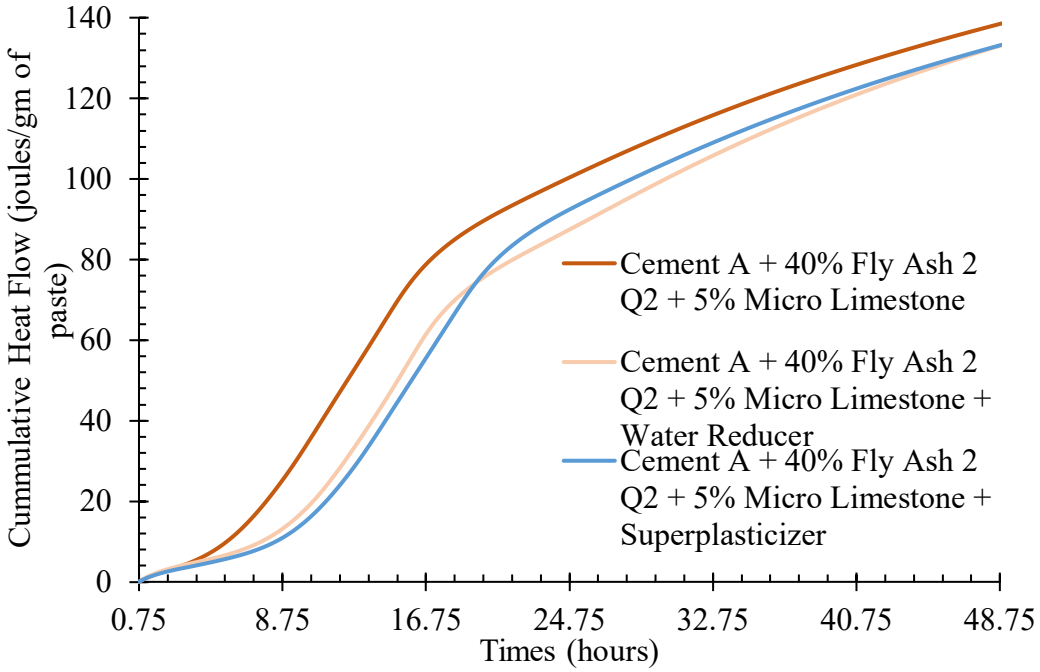

B. Fly Ash 2

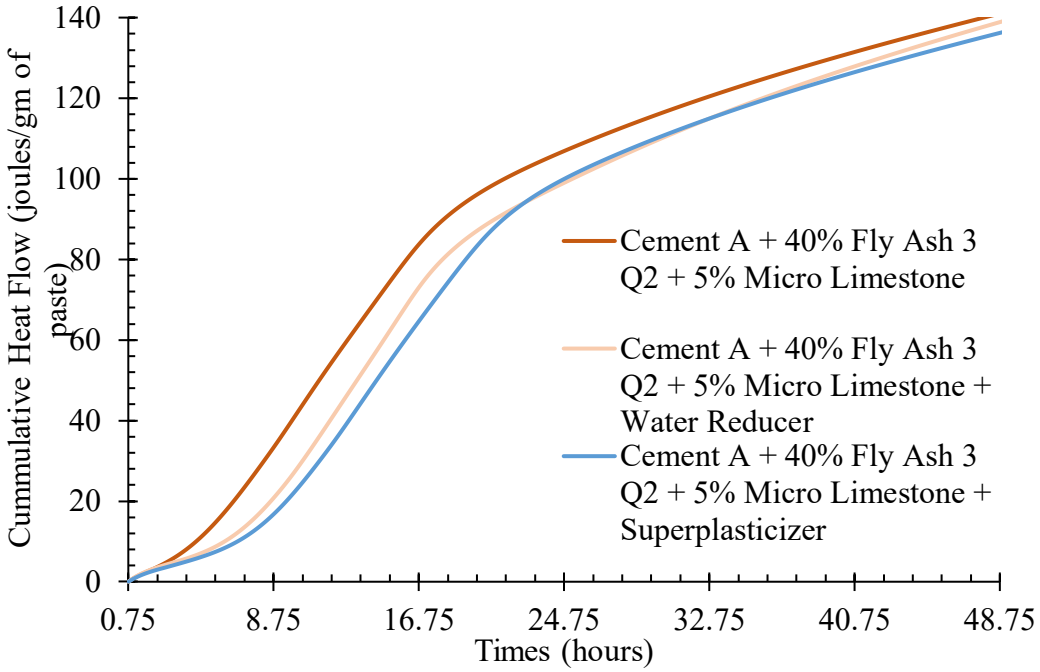

C. Fly Ash 3

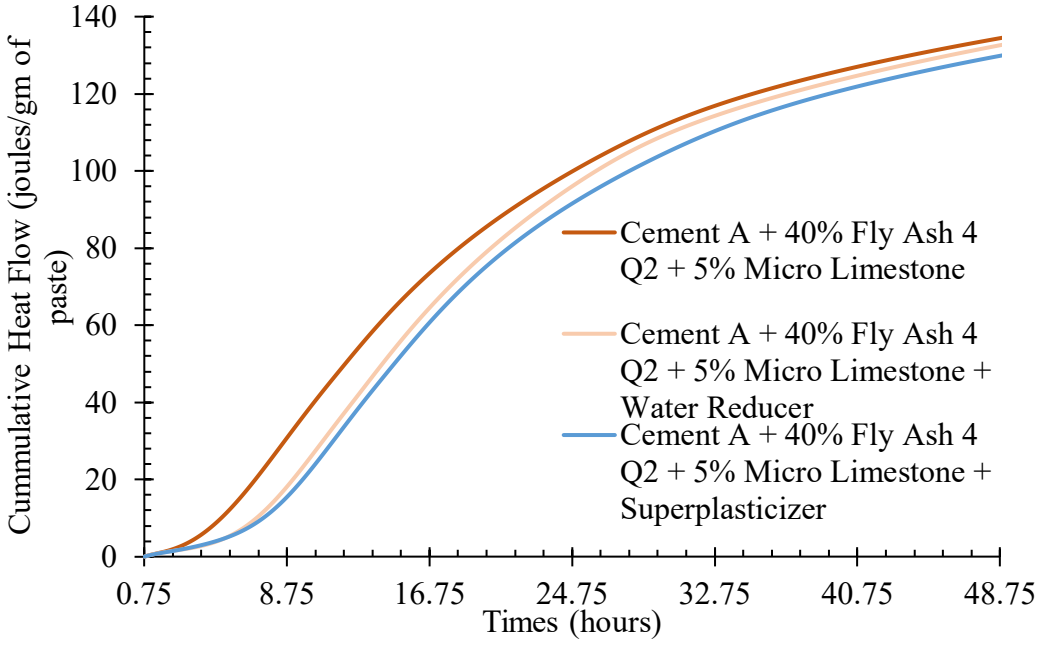

D. Fly Ash 4

Figure 32. Graphs. Effect of superplasticizer and water reducer on cumulative heat flow for 5% micro-limestone and 40% weight replacement of cement with (a) Fly Ash 1, (b) Fly Ash 2, (c) Fly Ash 3, and (d) Fly Ash 4 for 2019 Quarter 2 samples.

Table 14. Effect of Superplasticizer and Water Reducer on Cumulative Heat Flow for 5% Micro-limestone and 40% Weight Replacement of Cement with Different Fly Ash Sources

		Initial Setting Time (hr)	Final Setting Time (hr)
Fly Ash 1	Control	5.8	9.3
	Water Reducer	10.9	13.2
	Superplasticizer	9.6	14.2
Fly Ash 2	Control	5.8	10.6
	Water Reducer	10.6	13.1
	Superplasticizer	10.1	14.0
Fly Ash 3	Control	4.3	8.8
	Water Reducer	7.1	11.5
	Superplasticizer	8.2	13.1
Fly Ash 4	Control	3.7	8.4
	Water Reducer	6.5	10.2
	Superplasticizer	7.9	11.4

Table 15. Effect of 5% Micro-limestone Replacement on Acceleration of Setting Times

		Acceleration in Initial Setting Time (hr)	Acceleration in Final Setting Time (hr)
Fly Ash 1	Control	1.2	1.7
	Water Reducer	1.5	1.9
	Superplasticizer	3.4	2.8
Fly Ash 2	Control	1.4	0.6
	Water Reducer	1.4	1.5
	Superplasticizer	2.9	3.1
Fly Ash 3	Control	1.3	0.4
	Water Reducer	2.2	1.7
	Superplasticizer	2.9	2.2
Fly Ash 4	Control	1	-0.2
	Water Reducer	3.2	2.9
	Superplasticizer	2.7	2.6

CHAPTER 4: HVFAC FIELD TEST

Two test sections (each approximately 7.62 m [25 ft] long) were constructed in Canton, Illinois, in September 2020, to evaluate the mix design process and field performance of high-volume fly ash concrete pavement mixture relative to a conventional PCC pavement patching mixture. An IDOT-approved PP-1 mix (patching mix) with 25% cement replacement with fly ash was used as the control mix, where the other test section had 40% Class C fly ash replacement of cement. Patching mixtures have higher cementitious content and lower water-to-binder ratio. IDOT engineers performed compressive strength, slump, and air content tests, whereas the UIUC team installed wireless thermal sensors for compressive strength estimation using the maturity method and performed setting time measurement using noncontact ultrasound and laboratory calorimeter tests.

TEST SECTION DETAILS AND MIXTURE DESIGN

Both pavement test sections had a crushed aggregate base layer to which a 25.4 cm (10 in.) concrete pavement was cast. Wireless thermal sensors were placed at four different depths—1.3 cm (0.5 in.), 7.6 cm (3 in.), 19 cm (7.5 in.), and 22.9 cm (9 in.)—from the surface of the concrete. Two sets of sensors (a total of eight) were placed in each test section to ensure data quality and repeatability. Figure 33 presents schematics and details of the test section layout.

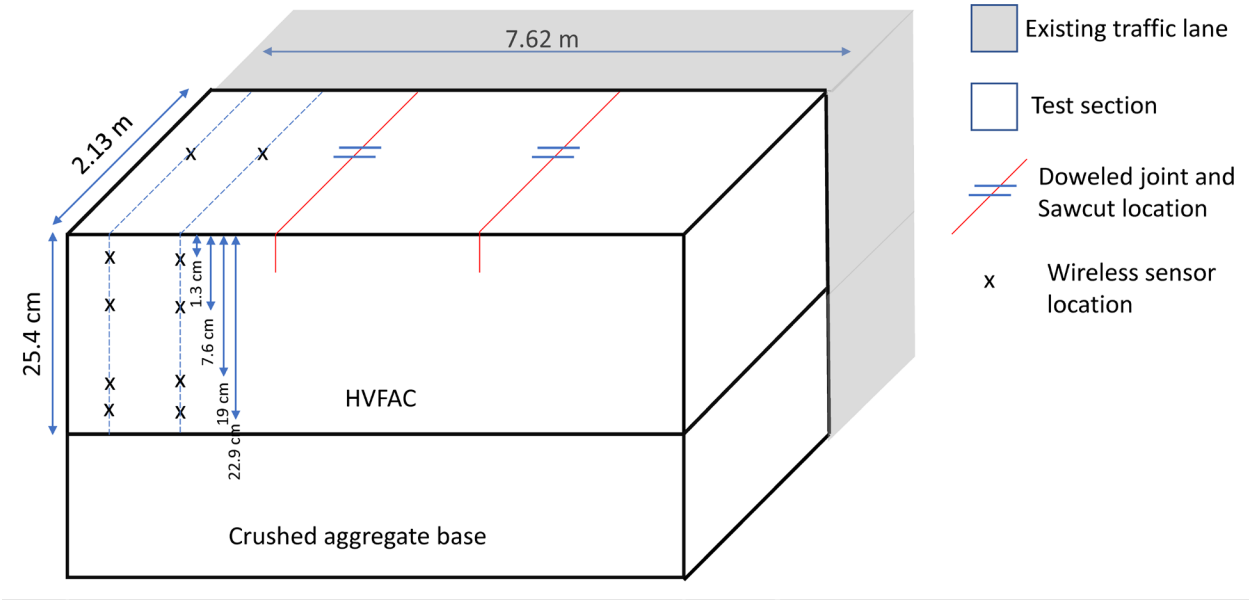

Figure 33. Photo. HVFAC field pavement test section details (not to scale).

The detailed mix design of both the HVFAC mix and the control mix (PP-1 mix) is given in Table 16. Both mixes had a water-to-binder ratio of 0.376. The air entrainer, water reducer, and superplasticizer used were AEA-92, WR-91, and EUCON-37, respectively. The water reducer and superplasticizer used in the concrete were kept constant in both the control and HVFAC mixes, but the AEA dosage was increased in the HVFAC mix to achieve proper air content. The superplasticizer

was batched and mixed in the concrete truck at the job site. The control and HVFAC mixes were prepared at 8:45 a.m. and 10:10 a.m., respectively, in the ready-mix plant. Both mixes had a similar slump and air content.

Table 16. Mix Design and Fresh Properties of Concrete Mixes

	Unit	Control Mix	HVFAC
Cement	Kg/m^3 (lbs/yd^3)	304 (512)	247 (416)
Fly Ash	Kg/m^3 (lbs/yd^3)	103 (174)	162 (273)
Coarse Aggregate	Kg/m^3 (lbs/yd^3)	1080 (1821)	1082 (1824)
Fine Aggregate	Kg/m^3 (lbs/yd^3)	700 (1179)	705 (1189)
Water	L/m^3 (gal/yd^3)	129 (26)	119 (24)
Air Entrainer	mL/m^3 (oz/yd^3)	232 (6)	309 (8)
Water Reducer	mL/m^3 (oz/yd^3)	812 (21)	812 (21)
Superplasticizer	mL/m^3 (oz/yd^3)	696 (18)	696 (18)
Air Content	%	5.7	5.1
Air Content from SAM	%	5.8	5.5
SAM No		0.3	0.1
Slump	cm (in.)	(6.25)	(5.5)

SETTING TIME MEASUREMENT

Setting time was measured in the field using the noncontact ultrasound developed by Tran and Roesler (2021). Constituent materials (cement, fly ash, chemical admixtures) from the field test site were collected and brought to the UIUC lab facilities to perform the noncontact ultrasound test in the lab environment (fixed temperature and humidity). Additionally, the UIUC lab calorimeter was used to evaluate the setting time as well for the cement, fly ash, and chemical admixture combination.

Noncontact Ultrasound Setting Time Test Method

The setting time of concrete is related to the penetration resistance of the concrete. According to ASTM C403 (2016), penetration resistance of 500 psi and 4,000 psi is related to the initial and final setting time of concrete. The penetration resistance of concrete indicates the development of compressive, tensile and shear resistance of the hydrating paste. In its plastic state, concrete has little to no shear resistance, but as concrete hydrates, significant shear resistance develops with time (Figure 34). Thus, tracking the shear resistance of concrete directly or indirectly can potentially indicate the setting time of concrete. One of the ways to indirectly track shear resistance development is the propagation of leaky Rayleigh waves. The noncontact ultrasound setting time measurement device developed by Tran and Roesler (2021) measures the energy of the leaky Rayleigh wave transmission to determine the time of final setting.

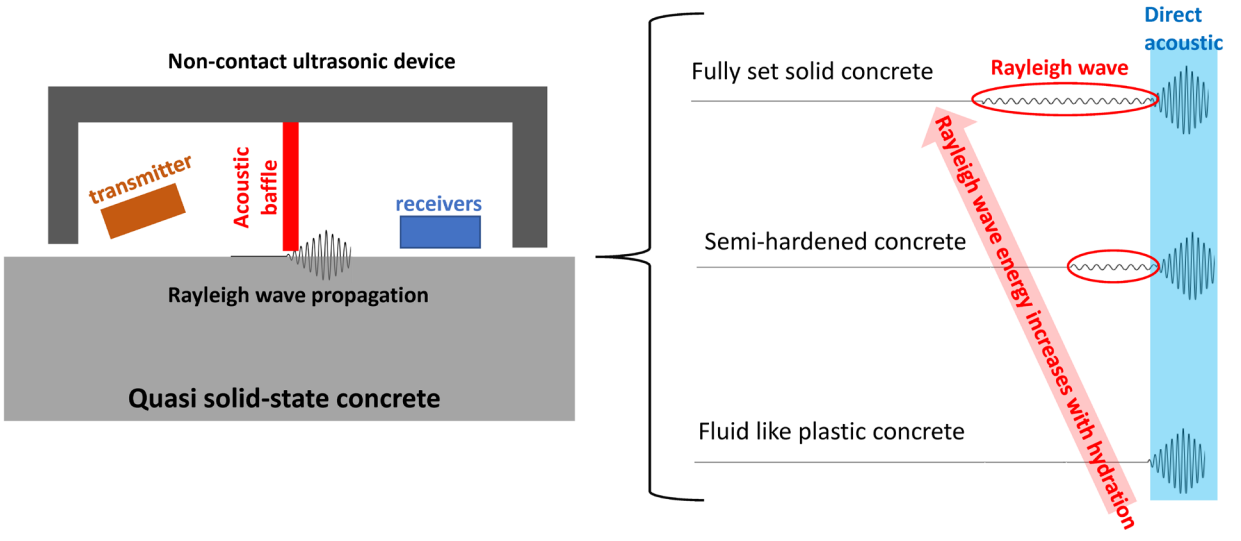

Figure 34. Schematic. Leaky Rayleigh wave propagation in concrete at different stages of hydration.

Briefly, this device uses an electrostatic-type ultrasonic transducer to transmit a 16-cycle 50 kHz ultrasonic pulse and three MEMS sensors as receivers. An acoustic baffle is placed in between the transmitter and receivers to reduce the direct-air acoustic signal. The receiver signal is then processed to calculate the leaky Rayleigh wave energy received over time. A sudden sharp increase of the leaky Rayleigh wave energy is taken as the final setting time. A detailed description of the test method and calculations can be found in Tran and Roesler (2021). A detailed schematic of the test set-up and an example of the setup in the field setting is shown in Figure 35.

Field Test Result

The evolution of the energy of the leaky Rayleigh wave over time after mixing the concrete for the control and HVFAC mixes is shown in Figure 36. The evolution of energy of the leaky Rayleigh wave received at the MEMS overtime was largely consistent between the three sensors. The noncontact ultrasound setting time device was successfully used to measure the average final setting time of the control mix of 4 hours 10 minutes. The final setting times from the three independent sensors were within 5 minutes. The set time for the HVFAC mix was not determined, as the final setting time of the HVFAC mix was much longer (> 7 hours) because of the higher fly ash content and superplasticizer.

Lab Test Result

For the same constituent materials in the field, setting time was determined in the lab environment using both the noncontact ultrasound setting time measurement device and the isothermal calorimeter. The calorimeter was operated at 22°C (71.6°F), whereas the ambient temperature for the noncontact ultrasound setting time device setup was at 25°C (77°F). The final setting time obtained from the two testing methods is shown in Table 17. Both methods gave similar results for the same mix. The HVFAC mix in the lab environment had a very high final setting time of 14–15 hours, consistent with the field result that the setting time is more than 7 hours. The control mixture final set was approximately 1.5 hours longer in the cooler lab environment. Note that the peak field temperatures were much higher (> 40°C [104°F]) than the lab environment, and thus the calculated

final setting time in these two environments are not meant to be same but should have similar relative trends when compared.

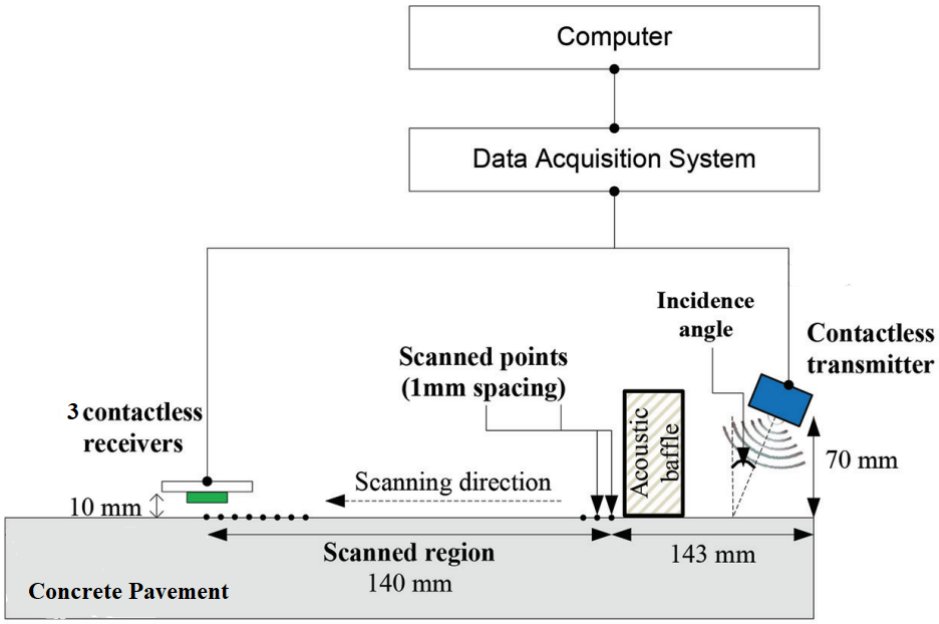

A. Schematic of noncontact ultrasound device

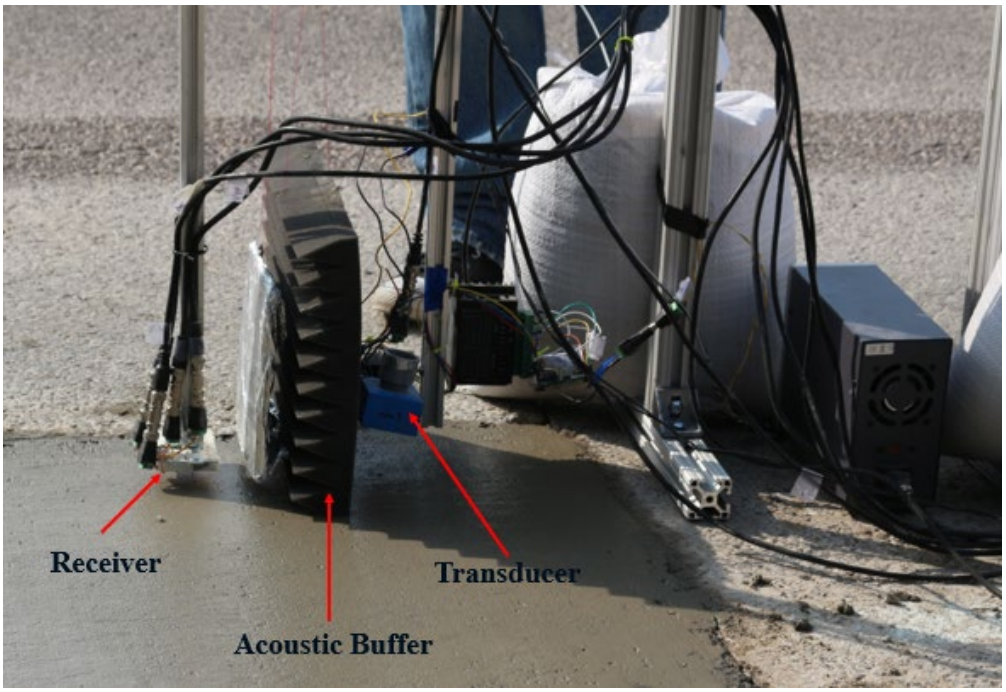

B. Photo of noncontact ultrasound device at test site

Figure 35. Photos. Noncontact ultrasound setting time measurement device. A detailed schematic of the device is shown in (a) (taken and modified from Tran and Roesler [2021]), and the device at the Canton, Illinois, field test site (b).

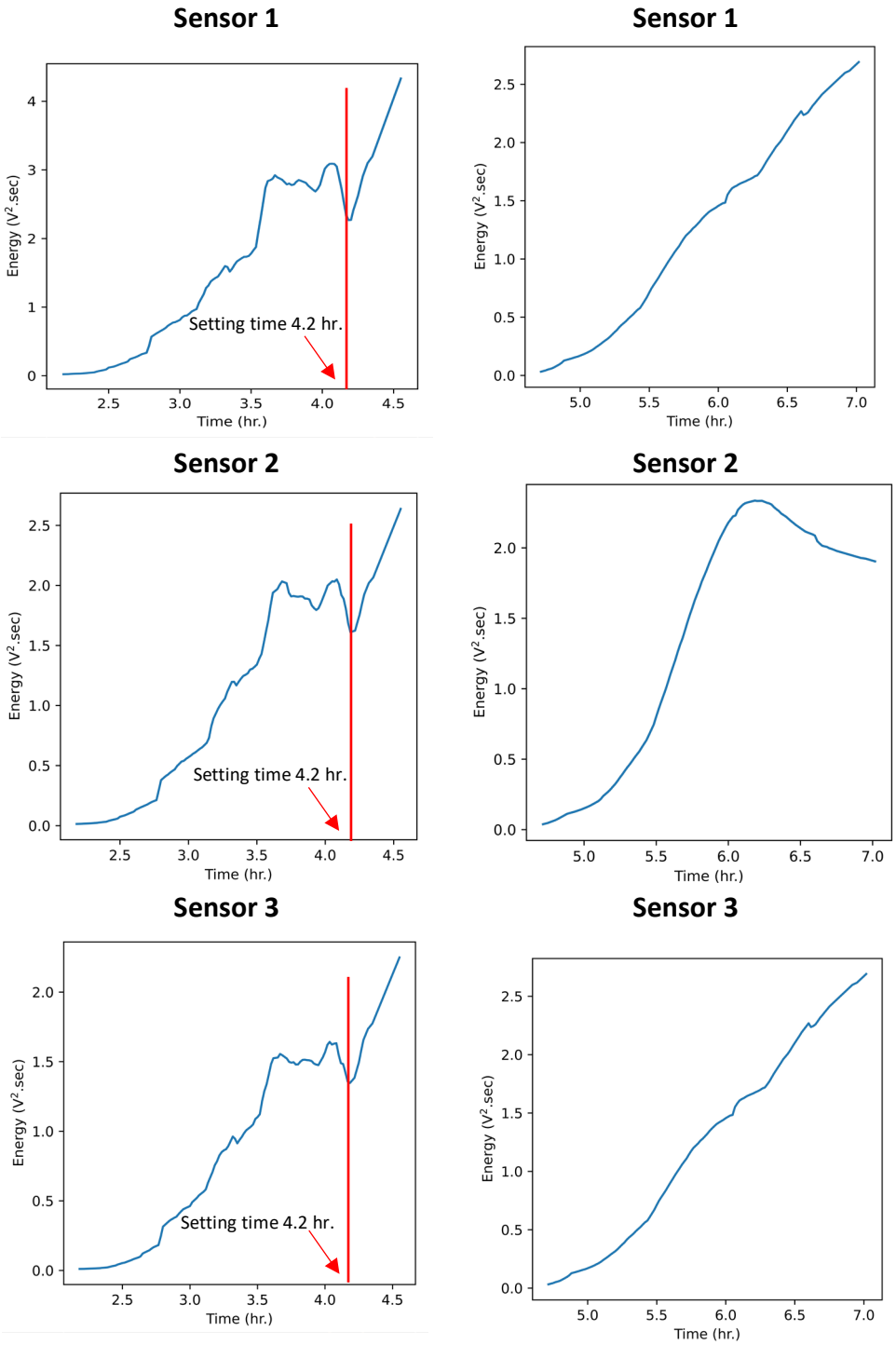

A. Control Mix B. HVFAC Mix

Figure 36. Graphs. Leaky Rayleigh wave energy of the (a) control mix and (b) HVFAC mix from three MEMS sensors. The setting time of the control mix determined by the three sensors were within 5 minutes of each other.

Table 17. Final Setting Time of Control and HVFAC Mixes in the Laboratory

Mix Type	Noncontact Ultrasound	Calorimetry
Control	5.4 hours	5.7 hours
HVFAC	14 hours	15.2 hours

Saw Cutting

The optimal saw-cutting timing to minimize joint raveling, while ensuring joint activation and no random crack development in the concrete slab, has been of interest to pavement engineers for a long time. Recently, Tran and Roesler (2020) evaluated joint raveling at different times using a computer vision–based technique and concluded that the ideal saw-cutting time should be a function of the final setting time: Saw-cut time = 1.3 x Final Setting Time + 39 minutes. Accordingly, the ideal saw-cutting time for the control mix should have been approximately 6 hours after the batching of the concrete. For the HVFAC mix, we know that the final setting time in the field was longer than 7 hours, and thus the ideal saw-cut timing would have been greater than 10 hours after batching. Saw cutting in both sections was performed extremely early (Control: 4 hours 25 minutes; HVFAC: 5 hours 35 minutes and 6 hours 20 minutes). Severe joint raveling was observed in both control and HVFAC sections. These incidents highlight the importance of using an on-site setting time measurement equipment such as the noncontact ultrasound setting time device to determine the saw-cut timing, especially for combinations of cement, fly ash, and admixtures.

A. Control mix: Saw cut after 4 hours 25 minutes

B. HVFAC mix: Saw cut after 5 hours 35 minutes

C. HVFAC mix: Saw cut after 6 hours 20 minutes

Figure 37. Photos. Saw cut and joint raveling in (a) control and (b and c) HVFAC sections.

MATURITY METHOD AND COMPRESSIVE STRENGTH

Wireless thermal sensors were installed in the field at different heights, and the temperature was measured for 30 days. Cylinders were cast in the field test sites by the IDOT engineers, and the cylinders were transported to the IDOT laboratory for compressive strength measurement. Wireless sensors were also placed inside two cylinders for each mix for maturity calibration. Finally, the maturity calibration curve was used to evaluate the compressive strength of the in-place concrete in the field.

Temperature Data

Wireless thermal sensors were placed at four different depths—1.3 cm (0.5 in.), 7.6 cm (3 in.), 19 cm (7.5 in.), and 22.9 cm (9 in.)—from the surface of the concrete. A photograph of the thermal sensors placed in the field site is shown in Figure 38. The repeatability of the thermal sensor data was quite good, as the mean deviation between two sensors installed at the same depth for the same mix was less than 0.5°C (0.9°F) (Figure 39). The temperature was significantly different at different depths inside the concrete. The variation in temperature over day and night in a single day decreased with increasing depth (Figure 40). Moreover, the peak temperatures (either highest or lowest in a single 24-hour period) occurred first on the sensors closest to the surface (1.3 cm [0.5 in.] depth), followed by the sensors at 6 cm (3 in.), 19 cm (7.5 in.), and 22.9 cm (9 in.) depths, respectively. As the temperature is significantly different at various depths inside the concrete, it is important to evaluate how the compressive strength changes when the compressive strength is calculated using the temperature data at different depths through the maturity method.

A. Thermal sensors installed in the field test section

B. Close-up photograph of the wireless thermal sensors

Figure 38. Photos. Thermal sensors installed in the field test section (a). Close-up photograph of the wireless thermal sensors (b).

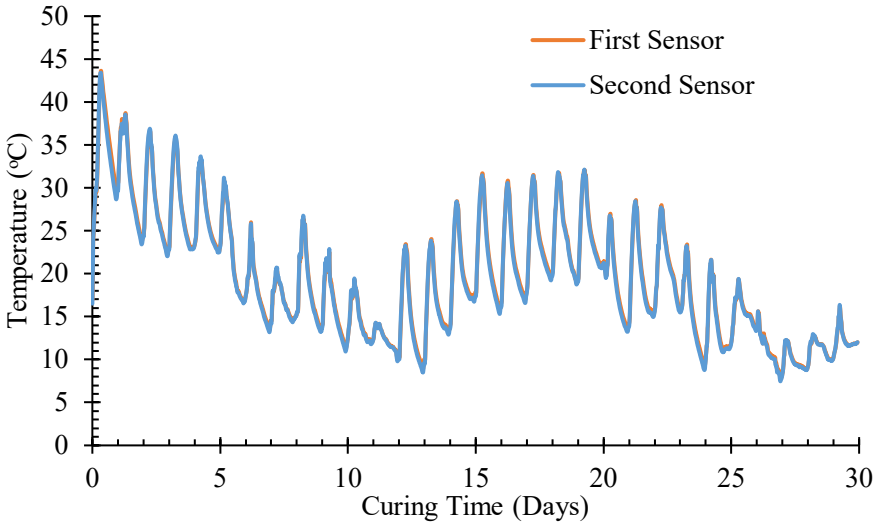

Figure 39. Graph. Temperature data from the topmost sensors (1.3 cm [0.5 in.] from the surface) for the control mix. The average deviation was 0.36°C (0.65°F).

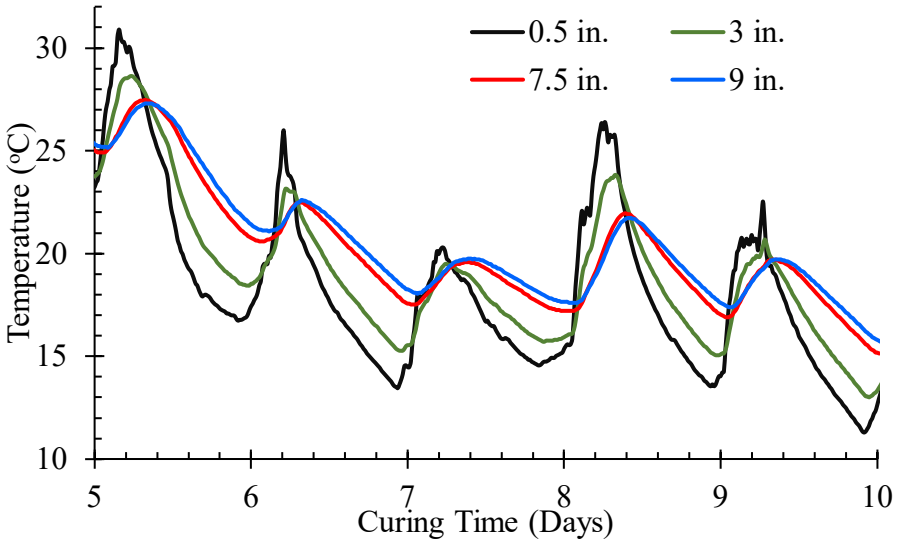

Figure 40. Graph. Temperature data at different depths for the control mix.

Compressive Strength Data and Maturity Calibration

The IDOT laboratory measured the compressive strength of the control and HVFAC mixes after 1, 3, 14, and 28 days of curing. As expected, the strength gain of the HVFAC mix was significantly lower than the control mix, but the 28-day strength for both the mixes was equal—49 MPa (7100 psi) (Figure 41). Current IDOT policy requires Class PV concrete to achieve 24 MPa (3,500 psi) compressive strength in 14 days, whereas Class PP concrete (used for patching) must have 22 MPa (3,200 psi) strength within 48 hours. Both mixes used in this project were PP mix and were thus required to reach 22 MPa (3,200 psi) strength in 48 hours. Even though the control mix reached that strength in

1-day curing, the HVFAC mix took 3 days to achieve that strength (1-day strength 15 MPa [2,175 psi], 3-day strength 26 MPa [3,770 psi]). Thus, based on the laboratory compressive strength data, a potential relaxation of the strength gain criteria or implementation of different methods to accelerate early-age strength (nano-limestone replacement, accelerator chemical admixture) will be needed for using this particular HVFAC mix for patching applications, given that the weather conditions remain same.

The maturity calibration curve is shown in Figure 42. The temperature-time factor was calculated using the Nurse-Saul equation. The maturity calibration curve fitting was good based on the limited compressive strength data collected for each mix.

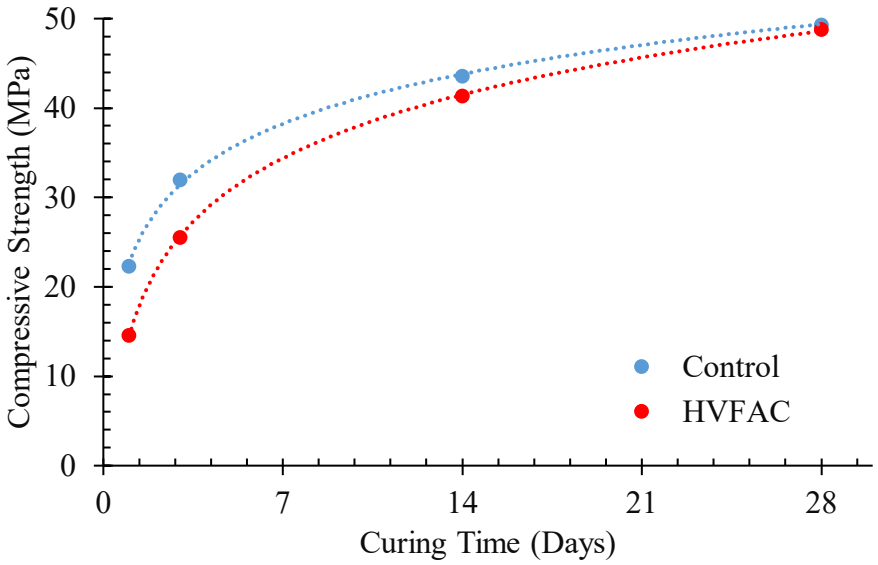

Figure 41. Graph. Compressive strength vs. curing time for HVFAC and control mixes.

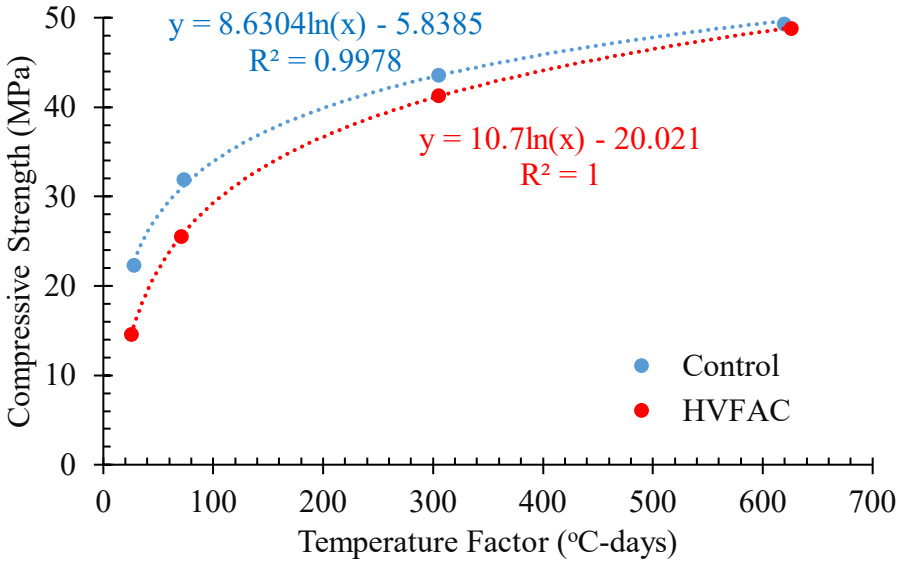

Figure 42. Graph. Maturity calibration curve for HVFAC and control mixes.

In-place Strength Estimation Using Maturity Method

The change in maturity over time for both the control and HVFAC mixes are given in Table 18 and Table 19, respectively. The HVFAC mix had a lower maturity than the control mixes, mostly because of the significantly higher temperature during the first day of hydration of the control mix compared to the HVFAC mix. Moreover, the maturity increased with depth in general for both the HVFAC and control mixes. However, the maturity at the top and bottom of the slab was not very different, and the difference was within 6%.

The maturity was then used to calculate the in-place compressive strength of the concretes at different times and different depths. Table 20 and Table 21 show the in-place compressive strength of the control and HVFAC mixes, respectively. The compressive strength at the top and bottom of the slab as calculated using the maturity method was within 5%. The percentage difference in the compressive strength between the top and the bottom of the slab was further reduced with increasing curing time. Thus, to evaluate the in-place compressive strength, the thermal sensor can be potentially placed at any depth for a concrete pavement within 25.4 cm (10 in.) thickness.

The in-place compressive strength for both the control and HVFAC mixes was greater than the compressive strength obtained in the laboratory at the same curing time. However, the in-place compressive strength may not always be greater than the laboratory strength, as the in-place compressive strength is strongly dependent on the weather.

The maturity method was also used to measure the in-place strength after 48 hours of casting, for both HVFAC and control mixes. Both the HVFAC and control mixes passed the 22 MPa (3,200 psi) criteria after 48 hours of curing, with the compressive strength of HVFAC and control mixes being 23 and 30 MPa (3,335 and 4,350 psi), respectively. The maturity method thus can be used to determine the earliest road-opening time after construction. Moreover, this method can be utilized when using traditional HVFAC mixes for patching projects with a relatively flexible road-opening time.

Table 18. Maturity of the Control Mix in the Field

	Control Mix Maturity (°C.days)			
	1.27 cm (0.5 in.)	**7.62 cm (3 in.)**	**19.05 cm (7.5 in.)**	**22.86 cm (9 in.)**
Day 1	34.8	36.4	35.8	34.8
Day 2	64.6	66.6	67.0	68.2
Day 3	94.2	97.2	98.0	97.1
Day 14	298.9	307.0	316.3	318.0
Day 28	564.3	575.1	588.1	591.3

Table 19. Maturity of the HVFAC Mix in the Field

	HVFAC Mix Maturity (°C.days)			
	1.27 cm (0.5 in.)	**7.62 cm (3 in.)**	**19.05 cm (7.5 in.)**	**22.86 cm (9 in.)**
Day 1	29.3	30.5	30.6	30.8
Day 2	60.4	61.0	61.1	61.2
Day 3	88.2	91.1	92.0	92.5
Day 14	291.5	300.4	309.9	313.3
Day 28	550.4	562.3	575.6	583.3

Table 20. In-place Compressive Strength of the Control Mix in the Field

	Control Compressive Strength (MPa)			
	1.27 cm (0.5 in.)	**7.62 cm (3 in.)**	**19.05 cm (7.5 in.)**	**22.86 cm (9 in.)**
Day 1	24.8	25.2	25.0	24.8
Day 2	30.1	30.4	30.4	30.6
Day 3	33.4	33.7	33.7	33.6
Day 14	43.4	43.6	43.8	43.9
Day 28	48.8	49.0	49.2	49.2

Table 21. In-place Compressive Strength of the HVFAC Mix in the Field

	HVFAC Compressive Strength (MPa)			
	1.27 cm (0.5 in.)	**7.62 cm (3 in.)**	**19.05 cm (7.5 in.)**	**22.86 cm (9 in.)**
Day 1	16.1	16.6	16.6	16.6
Day 2	23.9	24.0	24.0	24.0
Day 3	27.9	28.3	28.4	28.4
Day 14	40.7	41.0	41.4	41.5
Day 28	47.5	47.7	48.0	48.1

CHAPTER 5: CONCLUSIONS

This report contains a detailed literature review of concrete with high fly ash replacement of cement as well as different characterization test methods for satisfying the performance of HVFAC concrete. Replacement of cement with 50% GGBFS is allowed in multiple agencies, even though there are some concerns regarding salt-scaling performance. For GGBFS, no persistent problem was reported with setting time, strength gain, and durability properties for concrete with up to 50% GGBFS replacement. High-volume fly ash concrete (> 40% replacement of cement) was found to result in more variability in the early-age properties, which has limited its widespread application to pavements. The composition of fly ash and its chemical interaction with the cement and admixtures becomes more dominate in the overall hydration process, air system, and early-age properties of HVFAC.

Different fly ash sources used in Illinois were characterized with laser diffraction to measure the particle size distribution and EDXRF to measure the bulk oxide compositions. The fly ash oxide compositions from the same source but different quarterly samples were overall consistent with the most variations observed in SO_3 and MgO content. XPS was performed to evaluate the surface elemental composition. The elemental composition on the surface was significantly different from the bulk analysis. The surface had more carbon, sodium, potassium, and sulfur and less calcium, silicon, and aluminum than the bulk. XRD data showed that the minerals present in various fly ash sources were similar over multiple quarters, with amount of minerals varying for a particular source.

To understand the air-entraining performance of the different fly ash and quarterly variation, foam index tests were performed. The foam index of the different fly ash from Illinois varied over a wide range—from 1 µL AEA per gm fly ash (6.387×10^{-3} oz per lb fly ash) to 10 µL AEA per gm fly ash (6.387×10^{-2} oz per lb fly ash). XPS was performed to evaluate different carbon chemical environments of five fly ash sources, and a positive correlation among LOI, foam index, and C-C, C-H species percentage were found. A new computer vision–based foam index test, the digital foam index test (D-FIT), was also developed, which can reduce the sources of error between labs and operators.

Isothermal calorimetry provided necessary data on the heat evolved over time, which indicated setting times of the cement–fly ash combinations and potential sulfate imbalance in an HVFAC mixture. All calorimeter tests were run with a 40% cement replacement with fly ash. The HVFAC mixes had a lower hydration rate than the straight cement mixes, and the cumulative heat released after 48 hours was only about 70% of the straight cement mixes.

The setting times of fly ash from different quarters did not vary by more than 30 minutes. The Class C HVFAC mixes had a higher sulfate imbalance than Class F mixes. The addition of chemical admixture (both PCE- and lignosulfonate-based) delayed the hydration, but the delay was higher in using PCE-based admixture. The setting times were delayed by 4 to 5 hours and 5 to 6 hours for lignosulfonate-based and PCE-based admixtures, respectively.

To accelerate the setting times, micro- and nano-limestones partially replaced the cement. Limestone replacement in straight cement mixes accelerated the setting times, but the cumulative heat flow

after 48 hours decreased compared to the control mix when the replacement rate was higher than 5%. Nano-limestone was much more effective in accelerating the setting times compared to micro-limestone. Even though the cumulative heat flow after 48 hours was higher for 5% nano-limestone replacement than 5% micro-limestone replacement, there was no significant effect of the limestone particle size when the limestone replacement rate was 10% or higher.

Effects of replacing cement with limestone in HVFAC mixes were similar to that of straight cement mixes—the setting times were accelerated, and nano-limestone was more effective than micro-limestone. Both types of limestone were more effective in accelerating the setting times of HVFAC mixes compared to straight cement mixes. Five percent micro-limestone replacement accelerated setting times of HVFAC mixes with chemical admixtures by 2–3 hours. The setting time acceleration because of 5% micro-limestone replacement was similar for Class F HVFAC mixes with PCE- and lignosulfonate-based admixtures. However, for Class C HVFAC mixes, the acceleration was much higher in PCE-based admixture mixes compared to the lignosulfonate-based mixes. Thus, micro-limestone replacement at a relatively low rate can be a practical tool to accelerate the setting times without sacrificing long-term strength. Moreover, micro-limestone is widely available in the United States and can be used in high-volume, ready-mix concrete mixes.

The field test section construction of the HVFAC mix showed the feasibility and importance of using the noncontact ultrasound device to measure the final setting time as a function of the local climate conditions as well as determine the saw-cutting time. Field implementation of the maturity method showed that the compressive strength calculated using the maturity method does not depend on the pavement depth from which the temperature data is collected. Implementation of the maturity method for HVFAC and particularly the wireless thermal sensors can help agencies determine the earliest possible opening times for construction and regular traffic.

REFERENCES

Abdulla, Waleed. 2017. “Mask R-CNN for Object Detection and Instance Segmentation on Keras and TensorFlow.” *GitHub Repository*.

ACI CODE-318-19. 2019. *Building Code Requirements for Structural Concrete and Commentary.* Farmington Hills, MI: American Concrete Institute.

ACI SPEC-301-20. 2020. *Specifications for Concrete Construction.* Farmington Hills, MI: American Concrete Institute.

Amini, Kamran, Payam Vosoughi, Halil Ceylan, and Peter Taylor. 2019. “Linking Air-Void System and Mechanical Properties to Salt-Scaling Resistance of Concrete Containing Slag Cement.” *Cement and Concrete Composites* 104 (November): 103364. https://doi.org/10.1016/j.cemconcomp.2019.103364.

ASTM C150. 2020. *Standard Specification for Portland Cement.* West Conshohocken, PA: American Society for Testing and Materials.

ASTM C1827. 2020. *Standard Test Method for Determination of the Air-Entraining Admixture Demand of a Cementitious Mixture*. West Conshohocken, PA: American Society for Testing and Materials.

ASTM C188. 2017. *Standard Test Method for Density of Hydraulic Cement.* West Conshohocken, PA: American Society for Testing and Materials.

Bamforth, P. B. 1980. “In Situ Measurement of the Effect of Partial Portland Cement Replacement Using Either Fly Ash or Ground Granulated Blast-Furnace Slag on the Performance of Mass Concrete.” *Proceedings of the Institution of Civil Engineers (London). Part 1—Design & Construction* 69 (pt 2): 777–800.

Bentz, Dale P. 2011. “Powder Additions to Mitigate Retardation in High-Volume Fly Ash Mixtures.” *ACI Materials Journal* (107): 508–14. https://www.concrete.org/publications /internationalconcreteabstractsportal/m/details/id/51663971.

Boyd, A., and R. D. Hooton. 2007. “Long-Term Scaling Performance of Concretes Containing Supplementary Cementing Materials.” *Journal of Materials in Civil Engineering* 19 (10): 820–25.

California Department of Transportation. 2013. *Concrete Technology Manual*. Sacramento, CA: California Department of Transportation. https://dot.ca.gov/programs/engineering-services /manuals/sc-concrete-tech-manual.

Chatterjee, Anupam. 2015. “Duke Energy Fined over $100 Million for Environmental Violations.” *Reuters*, February 20, 2015. https://www.reuters.com/article/us-usa-duke-energy-environment/duke-energy-fined-over-100-million-for-environmental-violations-idUSKBN0LP00P20150221?irpc=932.

Deng, Shuang, Yun Shu, Songgeng Li, Gang Tian, Jiayu Huang, and Fan Zhang. 2016. “Chemical Forms of the Fluorine, Chlorine, Oxygen and Carbon in Coal Fly Ash and Their Correlations with Mercury Retention.” *Journal of Hazardous Materials* 301: 400–406. http://doi.org/10.1016/j.jhazmat.2015.09.032.

Detwiler, Rachel. 1997. *The Role of Fly Ash Composition in Reducing Alkali-Silica Reaction*. Skokie, IL:

Portland Cement Association.

Diaz-Loya, Ivan, Maria Juenger, Saamiya Seraj, and Rafic Minkara. 2019. “Extending Supplementary Cementitious Material Resources: Reclaimed and Remediated Fly Ash and Natural Pozzolans.” *Cement and Concrete Composites* 101: 44–51.

Duke Energy. 2020. *Duke Energy Winter Update*. Charlotte, NC: Duke Energy. https://www.duke-energy.com/_/media/pdfs/our-company/investors/2020-winter-update-w-reg-g.pdf?la=en.

Environmental Protection Agency. 2020. “Mercury and Air Toxics Standards for Power Plants Electronic Reporting Revisions.” *Federal Register*, 85 (175). https://www.govinfo.gov/content/pkg/FR-2020-09-09/pdf/2020-15950.pdf.

Farnam, Yaghoob, Bochen Zhang, and Jason Weiss. 2017. “Evaluating the Use of Supplementary Cementitious Materials to Mitigate Damage in Cementitious Materials Exposed to Calcium Chloride Deicing Salt.” *Cement and Concrete Composites*, 81: 77–86. https://doi.org/10.1016/j.cemconcomp.2017.05.003.

Federal Aviation Administration. 2018. “Advisory Circular 150/5370-10H Standard Specifications for Construction of Airports.” Accessed August 2, 2020. https://www.faa.gov/documentLibrary/media/Advisory_Circular/150-5370-10H.pdf

Girshick, Ross. 2015. “Fast R-CNN.” *Proceedings of the IEEE International Conference on Computer Vision* 2015 Inter: 1440–48.

Girshick, Ross, Jeff Donahue, Trevor Darrell, and Jitendra Malik. 2014. “Rich Feature Hierarchies for Accurate Object Detection and Semantic Segmentation.” *Proceedings of the IEEE Computer Society Conference on Computer Vision and Pattern Recognition*: 580–87.

Hackley, Vincent A., Lin-Sien Lum, Vadas Gintautas, and Chiara F. Ferraris. 2004. “Particle Size Analysis by Laser Diffraction Spectrometry: Application to Cementitious Powders.” *Aiche Journal*. https://www.nist.gov/publications/particle-size-distribution-laser-diffraction-spectrometry-application-cementitious.

Harris, Nathan J., Kenneth C. Hover, Kevin J. Folliard, and M. Tyler Ley. 2008a. “The Use of the Foam Index Test to Predict Air-Entraining Admixture Dosage in Concrete Containing Fly Ash: Part II—Development of a Standard Test Method: Proportions of Materials.” *Journal of ASTM International* 5 (7): 101603.

———. 2008b. “The Use of the Foam Index Test to Predict Air-Entraining Admixture Dosage in Concrete Containing Fly Ash: Part III—Development of a Standard Test Method: Proportions of Materials.” *Journal of ASTM International* 5 (7): 101603.

———. 2008c. “The Use of the Foam Index Test to Predict Air-Entraining Admixture Dosage in Concrete Containing Fly Ash: Part I—Development of a Standard Test Method: Proportions of Materials.” *Journal of ASTM International* 5 (7): 101603.

Jewell, Robert, and Robert Rathbone. 2009. “Optical Properties of Coal Combustion Byproducts for Particle-Size Analysis by Laser Diffraction.” *Coal Combustion and Gasification Products* 1 (1): 1–6.

Klobes, P., K. Meyer, and R. G. Munro. 2006. *Porosity and Specific Surface Area Measurements for*

Solid Materials. Washington, DC: National Institute of Standards and Technology. https://tsapps.nist.gov/publication/get_pdf.cfm?pub_id=854263.

Ley, M. Tyler, Nathan J. Harris, Kevin J. Folliard, and Kenneth C. Hover. 2008. "Investigation of Air-Entraining Admixture Dosage in Fly Ash Concrete." *ACI Materials Journal* 105 (5): 494–98.

Nassif, Hani, and Nakin Suksawang. 2003. *Development of High-Performance Concrete for Transportation Structures in New Jersey*. Rutgers: NJ: Center for Advanced Infrastructure & Transportation. https://www.nj.gov/transportation/business/research/reports/FHWA-NJ-2003-016.pdf.

Ren, Shaoqing, Kaiming He, Ross Girshick, and Jian Sun. 2017. "Faster R-CNN: Towards Real-Time Object Detection with Region Proposal Networks." *IEEE Transactions on Pattern Analysis and Machine Intelligence* 39 (6): 1137–49.

Stencel, John M., Haiping Song, and Federico Cangialosi. 2009. "Automated Foam Index Test: Quantifying Air Entraining Agent Addition and Interactions with Fly Ash-Cement Admixtures." *Cement and Concrete Research* 39 (4): 362–70.

Suraneni, Prannoy, Vahid J. Azad, O. Burkan Isgor, and W. Jason Weiss. 2017. "Use of Fly Ash to Minimize Deicing Salt Damage in Concrete Pavements." *Transportation Research Record* 2629 (2629): 24–32.

Tanikella, Prasanth, and Jan Olek. 2017. *Updating Physical and Chemical Characteristics of Fly Ash for Use in Concrete*. West Lafayette, IN: Joint Transportation Research Program.

Taylor, Peter, Luis A. Graf, Jerzy Z. Zemajtis, Vagn C. Johansen, Ronald L. Kozikowski, and Chiara F. Ferraris. 2006a. *Identifying Incompatible Combinations of Concrete Materials: Volume I—Final Report*. Washington, DC: Federal Highway Administration. https://rosap.ntl.bts.gov/view/dot/727.

———. 2006b. *Identifying Incompatible Combinations of Concrete Materials: Volume II—Test Protocol*. Washington, DC: Federal Highway Administration.

Tran, Quang, and Jeffery R. Roesler. 2020. "Noncontact Ultrasonic and Computer Vision Assessment for Sawcut Initiation Time." *Journal of Transportation Engineering, Part B: Pavements* 146 (3): 04020055.

———. 2021. "Contactless Ultrasonic Test System for Set Times of Mortar and Concrete." *ACI Materials Journal* 118 (2). https://doi.org/10.14359/51729328.

Tunstall, Lori E., George W. Scherer, and Robert K. Prud'homme. 2021. "A New Hypothesis for Air Loss in Cement Systems Containing Fly Ash." *Cement and Concrete Research* 142 (January): 106352. https://doi.org/10.1016/j.cemconres.2021.106352.

USACE. 2019. *Unified Facilities Guide Specification Division 03–Concrete, Section 03 30 00 Cast-In-Place Concrete*. https://www.wbdg.org/FFC/DOD/UFGS/UFGS 03 30 00.pdf.

Valenza, J. J., and G. W. Scherer. 2005. "Mechanisms of Salt Scaling." *Materials and Structures* 38 (4): 479–88. https://doi.org/10.1007/BF02482144.

Veranth, John M., David W. Pershing, Adel F. Sarofim, and Jeffrey E. Shield. 1998. "Sources of

Unburned Carbon in the Fly Ash Produced from Low-NOx Pulverized Coal Combustion." *Symposium (International) on Combustion* 27 (2): 1737–44. https://doi.org/10.1016/S0082-0784(98)80014-3.

Wirth, X., D. Benkeser, N. N. Nortey Yeboah, C. R. Shearer, K. E. Kurtis, and S. E. Burns. 2019. "Evaluation of Alternative Fly Ashes as Supplementary Cementitious Materials." *ACI Materials Journal* 116 (4): 69–77.

Yurdakul, Ezgi, Peter C. Taylor, Halil Ceylan, and Fatih Bektas. 2014. "Effect of Water-to-Binder Ratio, Air Content, and Type of Cementitious Materials on Fresh and Hardened Properties of Binary and Ternary Blended Concrete." *Journal of Materials in Civil Engineering* 26 (6). https://doi.org/10.1061/(ASCE)MT.1943-5533.0000900.

APPENDIX A: LITERATURE REVIEW—HVFAC

HVFAC has been defined as concrete with fly ash replacement higher than 40% (Ramme and Tharaniyil 2004) or 50% (Malhotra 2002). High-volume fly ash concrete (HVFAC) with up to 50% cement replaced with fly ash has been researched for more than 80 year for mass concrete applications (Davis et al. 1937). The first significant use of fly ash concrete was for construction of the Hungry Horse Dam (roller compacted) in Montana in 1949–52 with about 2.4 million cubic meter concrete being used (Roise 2018). Dunstan (1983) in the 1980s showed that up to 70%–85% of the cementitious volume in roller compacted concrete can be replaced with fly ash, and this technology was used in the access road construction of Didcot power station in England. Wisconsin Electric also constructed HVFAC pavement using the fly ash from the Pleasant Prairie power plant (Naik and Ramme 1987), which is a largest fly ash source even today. Initial success of HVFAC in pavement construction increased the interest in HVFAC, which spurred a lot of research on HVFAC in the next two decades (Mohan Malhotra et al. 2000; Malhotra 2002; Naik, Singh, and Ramme 1998; Naik and Ramme 1989; Sivasundaram, Carette, and Malhotra 2005).

Even with multiple demonstration projects and research studies completed on HVFAC, it still has not been widely adopted for pavement construction. A fresh review of previous research is warranted to understand and identify the potential opportunities to advance a higher replacement level of cement with fly ash in concrete pavements. This literature review will particularly focus on the early-age properties of HVFAC, including hydration and air entrainment, given early-age properties will determine the viability of HVFAC pavements not long-term strength and durability performance. The goal is to link the early-age performance parameters to different fly ash characterization methods.

FLY ASH CHARACTERIZATION METHODS

The fly ash currently used as a replacement of cement can be divided into two classes based on the CaO content: (a) Class C (CaO content > 18%) and (b) Class F (CaO content <= 18%) as per the ASTM C618 (2019). However, other agencies use different criteria to classify Class C and Class F fly ash. AASHTO M295 uses the sum of SiO_2, Al_2O_3, and Fe_2O_3 content as the determining criteria, with Class C fly ash having lower than 70% and Class F fly ash having higher than 70%. There are multiple standard methods to characterize different fly ash sources as described in ASTM C311 (2018) and ASTM M295, those tests were developed with aiming to replace only up to 25%–30% of cement in a concrete mix. Because the properties of HVFAC will be more sensitive to fly ash characteristics, as it contains fly ash in higher amounts, more emphasis needs to be placed on understanding different characterization techniques. In this section, the characterization methods to measure the different oxide contents will be discussed first as it is used for fly ash classifications. Next, different methods to evaluate the different crystalline and amorphous phases present will be explored. Finally, different methods to measure fly ash particle size distribution will be discussed.

Oxide Content of Fly Ash

Determination of oxide contents of fly ash is important for its classification. Fly ash is not a homogeneous material as the different fly ash particles have different compositions and, the element quantities present on the surface of fly ash particles generally differs from the bulk oxide content.

Konarski et al. (2013) used Secondary Ion Mass Spectroscopy (SIMS) to show that the outer layer of fly ash particles is rich in carbon and calcium, whereas the inner parts is enriched in sodium and aluminum. One of the most common method to measure bulk oxide content is EDXRF, whereas XPS is used to measure surface elemental composition. SEM-EDX is between these two methods as only top ~10 μm of the sample is examined using this method. Along with the three methods, researchers have used Secondary Ion Mass Spectroscopy (SIMS) (Konarski et al. 2013; Sakamoto et al. 2004), Electron Energy-Loss Spectroscopy (EELS)(Chen et al. 2005), Auger electron spectroscopy (Lindfors and Hovland 1978), and Electron Probe Microanalysis (EMPA) (Sen, Xianming, and Yong 2017) to characterize fly ash.

EDXRF

Bulk oxide content of fly ash is generally determined using EDXRF (Energy Dispersive X-Ray Fluorescence) as it is a quick and convenient method. In EDXRF, x-ray of a fixed energy is generated in an x-ray tube and the x-ray hits an inner shell electron of an atom present in the sample and ejects the electron. The vacant electron position in the inner shell is filled by an electron from the outer shell and as the energy of an electron in the outer shell is higher than energy on an electron in the inner shell, an x-ray with energy equal to the energy difference of the two different electron shell is emitted. Thus, the energy emitted is unique for each atoms and electron transition and can be used to identify the elements present in the sample. Thus, EDXRF measures the amount of different elements present, and then those element contents are converted back to the oxide content for convenience. In some cases, the conversion may be inaccurate as there may be multiple forms of oxides present in the fly ash sample. For example, the sulfur content in fly ash and other cementitious materials can be both in SO_3 and SO_4 states, even though conventionally the sulfur content is expressed in terms of SO_3.

There are three ways to prepare samples before performing EDXRF with decreasing order of accuracy and increasing order of convenience:

- Creating a fused bead by mixing a flux with fly ash and then heating it.
- Creating a pellet by pressing fly ash powder.
- Using fly ash powder as it is.

The theory behind Quantitative EDXRF assumes that the sample is infinitely thick, i.e., all the x-rays generated by the x-ray gun get absorbed by the sample. Realistically, having a sample thicker than ~10 mm can be used as almost all the x-rays get absorbed by the sample. EDXRF generally detects elements with atomic number higher than sodium (11), however the state-of-the-art EDXRF machines can detect elements with atomic number higher than carbon (6). EDXRF should be performed in vacuum or in helium environment to improve its accuracy especially for the light elements.

SEM-EDX

Scanning Electron Microscope (SEM) with an Energy Dispersive X-Ray Spectroscopy (EDS) analysis attachment can be used to visualize the morphologies of fly ash particles along with determining the oxide contents. SEM uses electrons instead visible light to obtain an image, and as the wavelength of

electrons are much smaller than wavelength of visible light, the resolution of SEM can be multiple times higher than that of an optical microscope. There are different properties of a SEM such as voltage, current, working distance, brightness etc. that controls the resolution, magnification, and depth of field of the images taken.

In SEM, the incident electrons from the electron gun interacts with the atoms in the samples and the different electrons ejected from the sample are measured by the different electron detectors. If the incident electron collides elastically with a sample atom at an angle close to 180°, the incident electron changes direction and leaves the sample. This is called Backscattered Electron (BSE). If the incident electron collides inelastically with an electron present in the sample, some of the energy of the incident electron gets transferred to the electron in the sample atom and the sample electron may get ionized and leave the sample. This ionized electron has a low kinetic energy and is called Secondary Electron (SE). Due to the nature of the collision, backscattered electrons have higher energy than secondary electrons. Because of its lower energy, only the secondary electrons generated near the surface of the sample can get out of the sample and be detected by the detectors. As secondary electrons reaching the detector originates near the surface (interaction volume ~10 nm), the images obtained in the secondary electron imaging mode provides information about surface topographies. On the other hand, the backscattered electrons generated relatively deep inside the sample (interaction volume > 1 μm) can also potentially leave the sample and be detected. The number of backscattered electrons reaching the detector depends on the atomic number, with higher atomic number elements having a brighter image. The different brightness can then be used to identify the location of different phases with different average atomic numbers, and if the phases present in the sample is known, it is possible to locate them individually in a sample.

In SEM-EDX system, the incident electron source hits the inner shell of an atom, and the inner shell electron of the atom goes out of the atom. An electron from the outer shell moves to the inner shell to fill the vacancy and as the energy of an outer shell electron is higher than the energy of an inner shell electron, a characteristic x-ray with energy equal to the electron energy difference of the inner and outer shell electron is generated, similar to EDXRF systems. The EDX detector collects the x-rays emitted and provides the quantitative details of the different elements present in the sample. The interaction volume of SEM-EDX is even higher than backscattered electron as x-rays generated in any part of the sample can potentially reach the detector.

As the SEM-EDX system can provide elemental composition at a particular point (resolution up to 1 μm), an automated SEM-EDX system (ASEM) can measure the elemental composition and diameter of each individual particles, if the particles are larger than 1 μm (Aboustait et al. 2016). Researchers have shown that the different types of fly ash particles can be divided into a number of classes and the amount of fly ash particles in each of those classes control different fly ash concrete properties such as compressive strength, electrical resistivity, and dissolution and leaching rates (Kim et al. 2019, 2020).

XPS

X-ray Photoelectron Spectroscopy (XPS) or Electron Spectroscopy for Chemical Analysis (ESCA) is one of the methods that measures the elemental composition on the surface (depth ~5–10 nm) of the fly

ash powders. Along with elemental composition, XPS also provides information about the chemical/oxidation state of those elements present in the sample.

XPS involves shooting x-rays to the sample, and when an atom in the sample absorbs an x-ray photon, electrons from the atom can be ejected (called photoelectrons) depending on the energy of the x-ray photon and the binding energy of the different electrons in the atom. The photoelectrons are then collected, and the kinetic energy of the photoelectrons ejected are measured. As the source x-ray photons have a fixed energy, the binding energy of the collected photoelectron will be equal to the difference between the source x-ray photon energy and the kinetic energy of the collected photoelectron. The potential energy of an electron in an atom depends on the chemical environment of the said atom, and the electron shell where it belongs. Thus, each atom in each chemical environment has an unique potential energy, which can then be used to trace back the different elements and their chemical environments present in the sample.

As XPS measures the amount of different materials on the surface, compared to EDXRF that measures the amount of different elements in bulk, the oxide contents obtained from XPS differ widely from the oxide contents obtained from EDXRF (Deng et al. 2016). Currently, the standards do not use XPS or any other methods that measure oxide contents. However, XPS has been used to predict the leaching characteristics (Hirokawa and Danzaki 1984) and air entraining performance (Chen et al. 2003) of fly ash.

Crystalline Phase Characterization of Fly Ash: XRD

Physical separation of crystalline and amorphous materials inside fly ash is not possible, and thus any characterization method used will characterize both the crystalline and amorphous materials together. Thus, to characterize only the crystalline part of the fly ash, a method needs to be chosen that is extremely sensitive to the crystalline phases present in the materials and not to the amorphous phases. X-Ray Diffraction (XRD) using Bragg's Law is one such crystalline detection method.

XRD involves shooting x-rays of a fixed wavelength to the sample with the x-rays diffracted by the sample, and then collection by a detector. If the sample has crystalline materials, the x-rays are diffracted with constructive interference at some angle given by Bragg's law:

$$n\lambda = 2d \sin\theta$$

Here, n is an integer, λ is the wavelength of the x-ray source, d is the distance between two planes in the crystal, and θ is the angle of incident x-ray on the sample. Different crystals have different d values, and thus, we can observe constructive interference at different θ values, and thus the crystals present in the system can be identified.

Fly ash generally contains multiple crystalline phases. Based on 18 Class F and 12 Class C fly ash studied from different locations over the US, Sutter et al. (2013) found that the major phases in Class C ashes are quartz, lime, tricalcium aluminate, periclase, and anhydrite, whereas the major phases in Class F ashes are quartz, mullite, hematite, and different ferrites in spinel group of minerals.

The intensity of diffracted x-rays increases in proportion to the amount of crystalline material present and can be used for quantification purposes. There are two major methods for quantification using XRD—(1) Relative Intensity Ratio method (RIR), and (2) Rietveld method. The RIR method uses the peak height and assumes that the peak height is directly proportional to the concentration of different crystals present in the sample. The Rietveld method, on the other hand, assumes that the peak area is directly proportional to the concentration of different crystals present in the sample. In general, Rietveld analysis is more accurate as the peak area does not change with particle size, whereas the peak width increases with decreasing particle size, leading to a decrease in peak height. Moreover, peaks from two different samples can overlap causing significant error in RIR method. Deconvolution is used in Rietveld analysis to separate the two peaks to obtain a more accurate quantitative information. However, direct use of both the Rietveld and RIR methods ignores the amorphous phases present in the sample and provides the concentration of each crystalline phase with respect to the total crystalline materials present in the sample. As fly ash can contain as much as 90% amorphous content (Nathan et al. 1999), it is important to determine the total amount of amorphous materials available in the fly ash to quantify the different crystalline phases with respect to the total sample mass.

There are multiple methods to determine amorphous content in a fly ash sample from the XRD data. The first method is the simplest and involves measuring the area of the broad hump in between 2θ = 15° and 54° created by the amorphous or glassy phases (Tanikella and Olek 2017). The peak area under this hump with respect total XRD area can be taken as the amorphous content in the fly ash. The second method is the internal standard method where a fixed amount of standard crystalline material, that is not present in the sample, is added to the sample and the XRD data is collected for the mix of the sample and the standard crystalline material. Comparing the crystalline phase composition obtained from the pure sample and the mix using RIR or Rietveld method can give amorphous phase content. Other methods such as the external standard method, or matrix flushing method can also be used to quantify the amorphous content. Hubbard et al. (1985) proposed that the ratio of K_2O and Al_2O_3 content in the bulk fly ash correlates with the amorphous glass content based on 26 fly ash collected in the UK.

Amorphous Phase Characterization of Fly Ash

Fly ash generally contains a higher amount of amorphous materials than crystalline phases, but there is no standard method available to characterize and quantify amorphous phases. SEM-EDX, described above in section titled “SEM-EDX”, is the most used method (Chancey 2008; Durdziński et al. 2015; Hemmings and Berry 1987; Kutchko and Kim 2006) in research to investigate glassy phases in fly ash. SEM-EDX is used to make maps of the different elements, and then the crystalline phases present in the ash can be identified using the ratio of different elements. The rest of the materials that are not crystalline can be taken as amorphous phases. As the resolution of SEM-EDX is around ~1 μm, it cannot accurately detect phases that are less than 1 μm in size. In some cases, some of the crystalline phases can be embedded in the amorphous phases making them hard to detect. As a result, the quantitative crystal phase information obtained from SEM-EDX generally varies from XRD analysis (Chancey 2008; Durdziński et al. 2015).

Most of the SEM-EDX analysis to evaluate the amorphous phases present in fly ash involves clustering. Chancey, (2008) used SEM-EDX and on a Class F fly ash and found that there are 3 different types of calcium aluminosilicate, one sodium aluminosilicate, and one potassium aluminosilicate glass phases are present. However, using the similar method on three Class C ashes showed that the glasses present in Class C ash is much more complicated than Class F ashes and classifying the different glassy phases were not possible. Oey (2019) found that for some fly ash samples (both Class C and F) it's not possible to make a cluster mapping due to high heterogeneity within particles. Durdziński et al. (2015) proposed to 4 main groups of amorphous phases present in the fly ash: (1) mostly silicates, (2) calcium silicates with low to moderate amount of aluminum, (3) alumino-silicate with low to moderate amount of calcium, and (4) calcium rich aluminosilicates. Oey (2019) divided the amorphous phases into 5 board clusters: (1) low calcium glass (< 15% CaO), (2) medium calcium glass (15% to 35% CaO), (3) high calcium glass (35% to 60% CaO), (4) low aluminum glass, and (5) amorphous silica. Most of the calcium aluminosilicate glass present in Class F ash had a low calcium content, whereas for Class C ashes it had a higher calcium content.

All the different research works focused on clustering different glassy phases present in the fly ash found that none of the clusters are narrowly defined. As a result, attempts have been made to characterize the glassy phase as a whole. Oey et al. (2017) used an unitless parameter called network ratio (N_r) to represent the network behavior of the glassy phase present in the fly ash. The higher the network ratio, the lower is the stability of the glass molecules. Network ratio was defined using this formula:

$$N_r = \frac{2\times(X_{Ca}+X_{Mg})+X_K+X_{Na}-X_{Al}}{X_{Si}+X_{Al}} \text{ for } \left[\frac{Al_2O_3}{M_2O+M'O}\right] < 1$$

$$N_r = 0 \text{ for } \left[\frac{Al_2O_3}{M_2O+M'O}\right] > 1$$

where X_{Al}, X_{Si}, X_K, X_{Na}, X_{Ca}, and X_{Mg} are the mole fraction of aluminum, silicon, potassium, sodium, calcium, and magnesium in the amorphous phases, respectively. $M_2O + M'O$ represents the mass fraction of alkali (M) and alkali earth metals (M') present in the glass, which is balanced by nonbridging oxygen or aluminum tetrahedra. The mole fraction of different elements present in the glass can be calculated from the overall oxide content obtained from EDXRF, and the quantitative crystalline composition data obtained from XRD with Rietveld analysis.

N_r can be correlated with different fly ash hydration physical properties. An increase in N_r generally involves a higher calcium content in the glassy phase which leads to an increase in the amorphous XRD hump discussed in section titled "Crystalline Phase Characterization of Fly Ash: XRD" .Moreover, as an increase in N_r decreases the stability of glass network, the glass transition temperature also decreases. For a 50-50 fly ash cement blend, the 7-day heat evolution increased with increasing network ratio, but no apparent effect of networking ratio was observed on the peak heat flow rate. The strength gain per unit heat release also decreases with increasing network ratio. This is because a higher network generally implies a calcium rich glassy phase, which in turn liberates more heat for C-S-H formation with a high Ca/Si ratio.

Particle Size Distribution of Fly Ash

Measuring particle size distribution of fly ash is important as a lower particle size generally accelerates hydration process. Three major ways to measure particle size distribution includes Laser Diffraction Spectrometry (LDS), x-ray sedigraph, and SEM will be discussed next. Out of these three methods, LDS and x-ray sedigraph performs a volumetric sampling, i.e., the probability whether a particle will be inside the test sample is proportional to the volume of that specific particle compared to the volume of the total sample used in the testing. On the contrary, SEM use a surface area based sampling, i.e., the probability whether a particle will be inside the test sample is proportional to the surface area of that specific particle compared to the surface area of the total sample used in the testing.

Laser Diffraction Spectrometry (LDS)

Laser Diffraction Spectrometry is one of the most used and convenient method to measure particle size distribution on a volumetric basis. In this method, the fly ash particles are dispersed in a solvent such as isopropyl alcohol that does not react/dissolve the fly ash particles. A laser light is passed through the dispersion and the transmission and the angular distribution of the laser light scattered by the fly ash particles are measured to determine the particle size distribution. Beer-Lambert law in conjunction with an optical model of light diffraction is used to convert the angular distribution to particle size distribution. Two optical models, namely Fraunhofer approximation and Mie scattering theory can be used and both have certain limitations. Fraunhofer approximation assumes that all particles present in the sample scatter light with same efficiency, the particles do not transmit light through them, and that the particle size is significantly larger than the wavelength of the source laser light used. Generally, the laser source has a wavelength <1 μm (most common is 633 nm), and Fraunhofer approximation does not provide accurate particle size for particles below 25 μm.

Mie scattering theory assumes that the particles are spherical, and each laser light photon gets scattered by only one particle. A very dilute dispersion can be used for fly ash particle size measurement using Mie scattering theory as most of the fly ash particles are spherical in shape. However, using Mie scattering theory requires optical properties (refraction index, and absorption index) of the sample and the dispersion medium. It is extremely difficult to measure the refractive index of the fly ash particles as all the particles are not similar and each particle have multiple phases present in them. The particle size distribution is sensitive to the refractive index especially for particle size less than1 μm. In practice, an approximate value of refractive index is used, which can potentially cause error in the particle size distribution (Cyr and Tagnit-Hamou 2001; Hackley et al. 2004).

X-ray Sedigraph

X-ray sedigraph method uses Beer-Lambert law combined with Stoke's law that determines the terminal velocity of a spherical particle through a medium. The terminal velocity is dependent on the viscosity and density of the dispersing medium, and the density of the sample. This method involves preparing a dilute dispersion of the sample similar to the laser diffraction spectroscopy, and then the particles are allowed to settle down in the dispersing medium under the effect of gravity. An x-ray beam of fixed height is passed through the dispersion and the transmittance of the x-ray beam is measured over time at multiple different heights, which is can then be converted back to

concentration of particles at different heights with respect to time. Using Stoke's law, the larger particles settle faster than the smaller particles as a result of the larger particles having a higher terminal velocity. Thus, the change in concentration of particles at different height with respect to time can be converted back to particle size distribution. However, this method underestimates the particle size of the large particles accurately as those particles may not reach the terminal velocity under gravitational force due to the limited length of the sample tube (Buchan et al. 1993). Moreover, if the sample particles have low density, the effect of random Brownian motion becomes significant for submicron particles leading to a wider particle size distribution compared to the true particle size distribution (Chung and Hogg 1985). Another limitation of using x-ray sedigraph for measuring fly ash particle size distribution is that the density of different fly ash particles from the same fly ash sample can vary widely due to presence of cenospheres, leading to inaccurate particle size distribution.

SEM

Using SEM for particle size distribution involves taking images of many fly ash particles and then use image analysis to find the particle size distribution. Fly ash particles are dispersed in a medium so that the particles are not agglomerated. A drop of the dispersion is then placed and dried on a slide. Many particle diameters are measured to obtain a proper sample size for the particle size distribution. In general, SEM images are taken at a magnification to measure the particle size distribution within a fixed size-range (Kim et al. 2019; Sutter, Hooton, and Schlorholtz 2013).

EARLY-AGE PROPERTIES OF HVFAC

The application of 40% or higher replacement levels of cement with fly ash will affect the fresh and hardened properties of concrete. In terms of fresh properties, the workability (Siddique 2004; Yoon et al. 2014) and water demand (Jiang and Malhotra 2000) of HVFAC is generally higher and lower respectively than conventional concrete with the same water to binder ratio because of the spherical shape of the fly ash particles. The water demand of HVFAC is lower than that of conventional concrete for three possible reasons (Mehta 2004):

- Fine particles present in the fly ash surround the cement particles because of their opposite surface charges and prevent cement particles from flocculating.
- Fly ash particles are spherical in nature which reduce inter-particle friction
- In some cases, fly ash particles help in providing proper particle packing and provide plasticity in the concrete mix.

The hydration reaction, setting time, plastic shrinkage, early-age strength gain, and air entrainment of HVFAC can be significantly different than conventional concrete. The hydration reaction directly controls the setting time, strength gain, and plastic shrinkage, whereas the amount and type of carbon present in the fly ash particles mostly affects the air entraining performance.

Hydration of HVFAC

The hydration reaction of HVFAC can differ significantly from the conventional concrete mix design. The degree to which it affects the HVFAC properties depend mainly on the chemical composition of amorphous and crystalline phases, chemical composition of the specific fly ash-cement blend, and particle sizes of the cement-fly ash blend. Coupling the hydration reactions and heat evolution with the chemical compositions of the cement-fly ash blend can provide insight into strategies to achieve setting times and strength gains more similar to 100% Portland cement or lower volume fly ash mixtures. Fly ash generally has a higher Al_2O_3 and SiO_2 and lower CaO content than typical cement. Moreover, fly ash also has significant amount of amorphous aluminosilicate phases that take part in pozzolanic reaction in the later stages of hydration. Fly ash also contains some nonreactive materials like carbon and quartz. HVFAC may also have an increased tricalcium aluminate to sulfate ratio leading to sulfate imbalance (Thomas 2007) and variable setting times depending on the fly ash content and cement source.

The next section will discuss how fly ash addition changes the heat of hydration, and then sulfate imbalance, and setting time of HVFAC will be reviewed. Moreover, the effect of limestone addition, type K cement, and type III cement for potential acceleration in setting time and early strength development will be discussed.

Heat of Hydration in HVFAC

The peak heat flow rate of HVFAC is significantly lower than conventional concrete because fly ash contains high amount of aluminosilicate glass content, which does not react at the beginning of the hydration reaction. The fly ash addition also affects the hydration of major hydrating phases (C_3A and C_3S) present in the cement. HVFAC may have a sulfate imbalance affecting the C_3A hydration, whereas the C_3S hydration may be delayed leading to an increase in the setting time.

Sulfate Imbalance

In Portland cement, calcium sulfate, generally in the form of gypsum, is added to delay the hydration rate of tricalcium aluminate (C_3A) (Minard et al. 2007; Quennoz and Scrivner 2012). Calcium sulfate also influences the tricalcium silicate hydration rate as calcium silicate hydrate precipitation is accelerated with the abundance of Ca^{2+} ions dissolving from calcium sulfate (Li et al. 2019). In general, fly ash has a negligible amount of calcium sulfate present, but it may have a significant amount of C_3A, especially in Class C fly ash. Thus, HVFAC reaction kinetics, setting time, and strength gain can vary significantly with the specific cement-fly ash interaction.

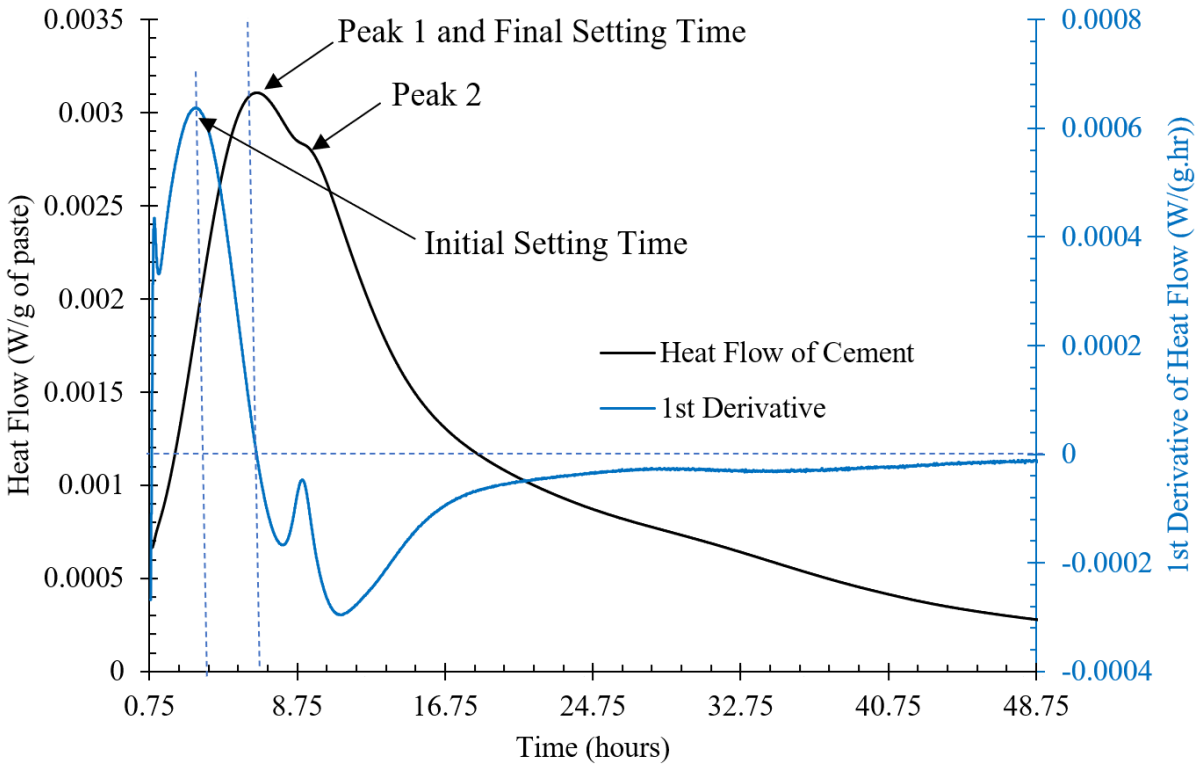

Figure 43. Graph. Isothermal calorimetry results for a sample Portland cement with initial and final setting time of 3.3 hours and 6.7 hours, respectively.

Isothermal calorimetry is a convenient tool to detect whether the cement-fly ash system is properly sulfated. Figure 43 shows a typical heat flow versus time curve normalized to the mass of paste obtained from a calorimeter test of a Portland cement. In Figure 43, Peak 1 represents the alite (C_3S) hydration peak, Peak 2 is the secondary ettringite formation, and the small valley between Peak 1 and Peak 2 is called sulfate depletion point (Bullard et al. 2011). The relative closeness and position of Peak 1 and Peak 2 of pure cement indicates a well-sulfated system. When the peaks are extremely close to each other or merged, the system is considered optimally sulfated.

Chemical admixtures, especially the polycarboxylate-based high range water reducing admixtures, have been shown to affect the dissolution of gypsum, leading to more severe sulfate imbalance in under-sulfated systems (Pourchet et al. 2006; Taylor et al. 2006) such as the case with HVFAC and Class C fly ash (Bentz 2011). Even though it is known that chemical admixtures affect the dissolution rate of calcium sulfates, there is limited research on how different types of chemical admixtures affect calcium sulfate dissolution rates (gypsum, hemihydrate, anhydrite) and potential sulfate imbalance. High volume fly ash replacement of cement is expected to further magnify chemical admixture interactions with cement-fly ash systems and thus, testing like isothermal calorimetry are important for the mix design process to identify early on potential adverse reactions.

Setting Time

The initial and final setting times of concrete very important for efficient construction of concrete pavement as the curing, tining, and saw cutting are dependent on the setting times. Moreover, a very long setting time can cause plastic shrinkage cracks as amount of plastic shrinkage is directly proportional to the final setting time (Gołaszewski et al. 2017). There are multiple methods to measure setting times such as vicat needle test (ASTM C191 2019), ultrasound wave propagation (Öztürk et al. 2006; Reinhardt, Große, and Herb 2000), calorimetry (Hu, Ge, and Wang 2014), noncontact ultrasound (Tran and Roesler 2020) etc. Calorimetry is one of the most convenient lab methods to estimate setting time.

Isothermal calorimetry can also be used to predict the trends in the initial and final setting times. As shown in Figure 43, the initial inflection point of the heat flow curve (2^{nd} derivative set to zero) has been defined as the initial setting time, whereas Peak 1, the C_3S hydration peak, has been previously defined as the final setting time (Hu, Ge, and Wang 2014). The lower amount of gypsum present in the under-sulfated system lowers the amount of Ca^{2+} dissolving from gypsum which in turn decreases the C-S-H precipitation rate and delays the C_3S peak hydration time. Thus, moderately under-sulfated systems have a longer final setting time compared to a well-sulfated system. However, a significant deficiency in sulfates in the HVFAC can potentially lead to flash setting and a very short set time (Beckemeier 2012). The setting times obtained from calorimeter data should not directly compare with the setting times obtained from ASTM C403 (2016) penetration tests, but the trends in setting time among different mixes observed from calorimeter data is similar to the trend observed from the standard ASTM tests (Hu, Ge, and Wang 2014).

Plastic Shrinkage

Plastic shrinkage could potentially be a concern for HVFAC because of its longer setting time. Elevated air temperatures can accelerate the setting time of HVFAC. However, higher temperature and wind speed, and low humidity increase evaporation of water and increase plastic shrinkage potential. The Canadian standards CSA 23.1 require that HVFAC with fly ash content more than 30% and 40% by mass should have a maximum w/b of 0.35, and 0.40 respectively for pavement mixtures exposed to freeze-thaw conditions. Moreover, a 7-day wet curing is recommended for HVFAC with more than 40% fly ash, whereas even a dry curing at higher than 10°C is sufficient for HVFAC with 30-40% fly ash. There have not been significant research findings on plastic shrinkage of HVFAC pavement.

Air Entrainment of HVFAC

Two-thirds of concrete in the United States is air-entrained for freeze-thaw durability (Dolch 1996). Air entrained concrete has well-distributed, small air bubbles that relieve the hydrostatic stress developed during ice formation. The concrete mixing process generates the air bubbles in the paste, which may not be stable depending on the density and surface tension of the paste, the air bubble radius, and the hydrostatic pressure on the air bubble (Du and Folliard 2005; Nagi et al. 2007). AEA used in concrete typically decreases the surface tension by as much as 20 mN/m (Mielenz et al. 1958), which prevents smaller bubbles from coalescing (Şahin et al. 2017) as the pressure difference between them decreases with a decrease in the surface tension of the medium. Additionally, larger air bubbles decrease compressive strength and are not effective in improving freeze-thaw resistance.

Air-entraining admixtures are have varying effectiveness in reducing surface tension of the medium. Ansari et al. (1999) showed synthetic resin for AEA in concrete produced larger air voids than Vinsol resin because of the lower surface tension of Vinsol resin.

Air entrainment of high-volume fly ash concrete create additional challenges. In general, the carbon content of fly ash has been increasing because of the introduction of low NO_x burners (Diaz-Loya et al. 2019). Additionally, use of powdered activated carbon for NO_x absorption also increases activated carbon content in fly ash. These carbon particles present in the fly ash provide a high surface area on which AEA can be adsorbed, and thus less AEA is available to stabilize air bubbles. The Ca^{2+} and Mg^{2+} ions present in the paste may also cause the AEA to precipitate, which reduces the amount of available AEA. The types of carbon in fly ash and Ca^{2+} and Mg^{2+} ions present in the pore solution are discussed next with respect to its effect on air entrainment.

Types of Carbon in Fly Ash

The effect of carbon on air-entraining performance is well-documented with the ASTM C311 method (ASTM C311 2018) created to limit the amount of carbon present in the fly ash through the Loss on Ignition (LOI) test. ASTM C618 (2019) limits the LOI to less than 6% for Class C fly ash and LOI up to 12% for Class F fly ash with air content performance test verification. However, the ASTM C311 LOI test overestimates the fly ash carbon content as the mass loss up to 750°C includes any bound water or other phases along with carbon.

The majority of researchers agree that air entrainment of fly ash concrete cannot be adequately predicted from the amount of carbon present in the system in bulk because the interaction of carbon and AEA depends on the different types of carbon (Freeman et al. 1997; Külaots, Hurt, and Suuberg 2004). Carbon present in fly ash can be divided into organic and inorganic parts. It is generally accepted that only organic carbon takes part in AEA adsorption, whereas inorganic carbon is essentially inactive (Pedersen et al. 2008). Multiple researchers (Chen et al. 2002, 2003; Gao et al. 2001) have shown that oxidizing fly ash samples using ozone that transforms the organic carbon into an oxide form dramatically reduces the AEA adsorption capacity. Similarly, removing the organic carbon through heating the fly ash sample at 600°C also reduces the potential for AEA adsorption. Thus, measuring and quantifying the organic carbon is more advantageous when considering the air-entraining dosage of HVFAC. There are three distinct forms of organic carbon in fly ash: Volatile Organic Compounds (VOC), soot, and charcoal. Fan and Brown (2001) quantified the VOC content by the color change after mixing fly ash with benzene and found that about 15 to 80% of unburnt carbon present in fly ash was VOC. Fan and Brown (2001) hypothesized that VOCs in fly ash are aromatic carbons and come from volatilization of tar.

The second type of organic carbon is soot particles, which are generated because of partial combustion of hydrocarbons in a low oxygen environment. Soot particles are extremely small with an average size of 40 nm. The amount of soot particles in fly ash is difficult to measure using a conventional LOI test because oxidation of soot occurs slowly at 750°C and may not be effective at all. Soot particles can also adsorb AEA and decrease available air entrainment significantly if present in large amounts (>10% of total carbon content). Gao et al. (1997) examined the presence of soot using high-resolution Transmission Electron Microscopy and found only trace amounts of soot in all their fly

ash samples, which did not affect air-entrainment. To quantify soot particles in fly ash, Gao et al. (1997) recommended an "Optical Fine Particle Test" which involved dispersing fly ash in a colloidal 40 nm silica solution and then putting it in a centrifuge to remove all the larger particles of fly ash. Finally, absorbance at 500 nm is measured to obtain a qualitative measure of the amount of soot in the sample. This test is useful to confirm absence or significant presence of soot particles in fly ash.

The third type of organic carbon is charcoal or "char". In general, the char particles are large enough to be seen by an optical microscope (Külaots, Hurt, and Suuberg 2004). Most of the organic carbon in typical fly ash is in the form of charcoal. However, char does not contribute to AEA adsorption in proportion to its weight because of the relatively lower specific surface area compared to the other forms of carbon. Activated carbon used in low NO_x emission coal power plants is also a type of charcoal and is one exception because it has an extremely high specific surface area. Thus, activated carbon contaminated fly ash may have a very high AEA absorption capacity even if LOI is not high (Freeman et al. 1997).

Even though it is agreed that carbon present in fly ash affects air-entraining performance, there are only a few studies systematically investigating the types of carbon and their effect on air entrainment. The types of AEAs (ionic and nonionic) chemically interact with the types of carbon in different manners because of a carbon's specific surface area and surface charge density. The conventionally used LOI test only provides an approximate bulk carbon content but does not measure the soot particles or capture the effect of different types of carbons present in fly ash. A better understanding of soot, charcoal, and VOC contents in fly ash sourced from different power plants should provide more insight toward the effect of different coal-burning processes and coal sources on the fly ash quality and interaction with AEA.

Effect of Ca^{2+} and Mg^{2+} in Pore Solution

Replacement of cement with fly ash changes dissolution rates and thus affects the concentration of ions present in the solution. Anionic air-entraining agents are precipitated with increasing Ca^{2+} and Mg^{2+} concentrations (Baltrus and LaCount 2001; Bruere 1970; Jolicoeur et al. 2009). Divalent ion concentrations affect the AEA precipitation more than monovalent ions because of the higher charge density of the divalent ions (Somorjai and Li 2010). The divalent cation concentration generally affects the performance of anionic air-entraining agents more than divalent anion concentration affects cationic air-entraining agents because the anions are larger in general, leading to a lower charge density.

Tests for Evaluating Air Entrainment

Many performance-based tests exist to quantify the air-entraining performance of concrete. As the properties of fly ash are important in the air-entraining of HVFAC, the relevant quality control tests are discussed next.

Concrete-Based Air Tests

The total air content and its distribution in a concrete mixture are the main ways to determine the performance of AEA. There are several standard methods to evaluate total air content in concrete in both the fresh and hardened state. Measuring bulk air content in fresh concrete can be done using

three different methods: gravimetric (ASTM C138 2017), pressure (ASTM C231 2017) and volumetric (ASTM C173 2016) with the pressure method the most common. Determination of the optimum AEA dosage to achieve the specified air content requires multiple mixtures for the standard mixing procedure. Ley (2010) developed a more efficient method to determine the target air-entraining dosage from a single concrete mix by combining air content measurement through volumetric and pressure methods. In case of hardened concrete, ASTM C457 (2016) prescribes three standard test methods to evaluate the total air content and the air void distribution, i.e., linear-traverse method, modified point count method, and contrast-enhanced method. Recently, Ley et al. (2017) developed a test that can predict the freeze-thaw performance and air voids distribution of concrete by applying sequential pressure on fresh concrete, i.e., Super Air Meter, which is currently a provisional AASTHO TP 118 standard being used by multiple state DOTs.

Foam Index Test

One common test method to understand the change of cementitious materials on the required AEA dosage is the Foam Index test. This test adds prescribed dosages of AEA to a diluted mix of water and cementitious materials until stable bubbles are formed. The stability of the bubble is assessed by the operator and thus, test variance is expectedly high. As the foam index test is not a standard test, researchers have used different conditions to perform it since its introduction (Dodson 1990). Harris et al., (2008a, 2008b, 2008c) studied the different test parameters, such as the container capacity versus amount of solution, mixing procedure, time of test, water to binder ratio, fly ash to binder ratio, etc. and proposed guidelines for a standardized test method given its known repeatability issues (Taylor et al. 2006). Stencel et al. (2009) developed an automated foam index test that measures the number of acoustic events and thus determines the foam stability, which can then be related to foam index. Recently, Watkins et al. (2015) proposed using a mechanical shaker to reduce the operator variability in the foam index test proposed by Harris et al. (2008a, 2008b, 2008c). Although the adsorption equilibrium between fly ash and AEA may take over an hour (Yu et al. 2000), the test duration was fixed to be 15±3 minutes to make the test results more rapid. Even with these modifications, the foam index and LOI could not be correlated, especially at LOI less than 5% (Watkins et al. 2015), because of the limitations in the LOI test. The foam index test still can provide for fly ash quality consistency but a standardized, simple, and rapid quality control test for fly ash is especially needed for evaluating air systems in HVFAC.

Foam Drainage Test

Foam drainage test is a test similar to the foam index test, but it is a quantitative test, first proposed by Gutmann (1987). This test involves mixing the air entrainer with the binder at a very high w/b ratio (~20) in a container, and then shaking the mix. After shaking, the liquid along with the foam generated is poured out to a one-liter graduated cylinder, and the change in volume of the liquid due to the foam bubbles popping is monitored over 60 minutes. The decrease in volume after 60 minutes and the rate of decrease in volume over time can be used to evaluate the stability of the air-void system, even though the air content in hardened concrete does not correlate with the foam drainage (Taylor et al. 2006). This test can potentially be used to evaluate compatibility between different admixtures (Wang et al. 2019) as well.

Iodine Number Test

Iodine number test is an experiment that measures the absorption of iodine by the fly ash. Fly ash added to an iodine solution of known concentration, and after certain time, the amount of iodine left in the solution is determined using a thiosulfate-based titration. This test, however, is not very sensitive compared to foam index test for low LOI ashes (Sutter, Hooton, and Schlorholtz 2013). Moreover, this test only examines the fly ash, and not the interaction between the air entrainer and the fly ash (Sutter, Hooton, and Schlorholtz 2013).

HARDENED PROPERTIES OF HVFAC

Hardened properties of HVFAC includes different mechanical and durability properties. Important mechanical properties include compressive strength, flexural strength, tensile strength, and modulus of elasticity, whereas durability properties include alkali silica reaction, salt scaling, freeze-thaw durability, and corrosion.

Compressive and Flexural Strength

The compressive and flexural strength of HVFAC is generally lower than conventional concrete in early ages, but it is still possible to attain the required strength for concrete pavement applications. The strength development of HVFAC is slower than conventional concrete, especially for the first 7 days. However, the strength gain increases after that as the pozzolanic materials in fly ash start to hydrate and contribute to the strength gain.

Current IDOT policy requires Class PV concrete to achieve 3500 psi compressive strength in 14 days, whereas Class PP concrete (used for patching) must have 3200 psi strength within 48 hours. Based on tests performed on four Class C and one Class F ash sourced in the Midwest with 625 lbs/yd^3 binder content with 40% fly ash replacement and 0.45 w/b ratio, all 4 HVFAC with Class C ash attained 3500 psi strength after only 7 days, whereas the Class F ash took 28 days (14-day strength was 3300 psi, 28-day strength was 4500 psi). Given that the current IDOT specification mandates a w/b ratio within 0.32-0.42 for pavement concrete mixes, a lower w/b will help the HVFAC with Class F ash reach 3500 psi strength in 14 days. Thus, HVFAC can meet Class PV concrete criteria without any significant modification. On the other hand, attaining 3200 psi strength in 48 hours is challenging for HVFAC, and adjustments are need to accelerate the strength gain.

Freeze-Thaw Durability

Freeze-thaw durability is extremely important for concrete pavement mixtures used in the Midwest. Properly air-entrained HVFAC with either Class C (Ramme and Tharaniyil 2004) or Class F ash (Bisaillon, Rivest, and Malhotra 1994) shows freeze-thaw performance similar to conventional concrete.

Alkali-Silica Reaction (ASR)

Fly ash replacement in concrete generally reduces the alkali-silica reaction, and HVFAC is expected to have better ASR durability compared to conventional concrete or concrete with low fly ash replacement. There are multiple mechanisms proposed in the literature to explain the effect of fly

ash replacement on reducing the ASR potential (Shafaatian et al. 2013). They are discussed briefly below:

- Alkali Dilution : The alkali content in the pore solution of fly ash concrete is in general lower than the concrete without any fly ash because only a portion of the fly ash is soluble, and the dissolution rate of alkali from fly ash is also slower. This effect is expected to be more dominant and improve ASR durability with increasing fly ash replacement.
- Alkali Binding: The C-S-H generated by the pozzolanic reaction improve the volume fraction of C-S-H in the cement paste. C-S-H generated by pozzolanic reaction has a lower Ca/Si ratio due to lower availability of Ca. C-S-H with a lower Ca/Si ratio has a higher alkali binding capacity because of the increasing acidity of the Si-OH and the negative (alkali attractive) surface charge. This is one of the reasons why Class F ash performs better in limiting ASR compared to Class C ash as the Ca/Si ratio in pozzolanic C-S-H is much lower than in Class C ash. Increasing fly ash replacement is expected to improve the alkali binding property.
- Modification of ASR Gel: Composition of the ASR gel can also affect its ability to swell and cause pressure. ASR gel with very low CaO/Na_2O_{eq} can diffuse through the concrete easily and apply very low swelling pressure (Bleszynski and Thomas 1998). Increasing fly ash replacement will decrease the CaO/Na_2O of the ASR gel formed, especially for Class F ashes.
- Soluble Aluminum Source: Fly ash can provide soluble aluminum that can get incorporated into the C-S-H formation to form C-A-S-H, which has higher ability of alkali binding (Hong and Glasser 2002). Thus, increasing fly ash replacement will increase C-A-S-H formation and alkali binding leading to ASR mitigation.

Phillips (2015) showed that replacing cement by 40% Class C ash satisfies the ASTM accelerated mortar bar test expansion limit even when using a highly reactive aggregate. However, fly ash containing more than 5% MgO (current ASTM C618 limit) content was susceptible to ASR expansion. Mehta (2004) also recommended using HVFAC for enhancing ASR durability based on field tests. Thus, the existing literature and research findings suggest HVFAC should exhibit good ASR durability all things equal.

Salt Scaling

HVFAC salt-scaling performance can vary, i.e., it may have worse salt-scaling performance than conventional concrete without any fly ash replacement, but it is possible to obtain satisfactory salt scaling performance. Salt scaling is dependent on my factors including concrete mixture design, curing, bleed rate, degree of over finishing concrete surface, volume of salt applied, and placement season.

The Scherer research group performed salt-scaling experiments at many different conditions and proposed a glue-spalling mechanism to explain all the observations (Valenza and Scherer 2005; Valenza and Scherer 2006, 2007b, 2007a). Glue spalling is a technique used in glass decoration industry where epoxy is spread on a sand-blasted glass surface. After the epoxy is cured, the glass-epoxy composite is cooled down, which creates tensile stress at the boundary of the glass-epoxy interface as the epoxy contracts more than the glass substrate. This tensile stress creates a

characteristic cracking pattern through the glass surface because of the strong interfacial bond between the epoxy and glass.

The coefficient of expansion of ice is much higher than concrete; thus, the ice works similar to epoxy in the glue spalling technique in the glass decoration industry. When salt is applied to the concrete, it melts the snow and creates liquid brine water. However, as temperatures decrease below the freezing temperature, ice is formed, and the brine becomes more concentrated as the salt ions do not penetrate the ice. As more and more ice is created, the concentration of salt in the brine water becomes higher. With decreasing temperature, most of the concrete surface is covered by ice with certain pockets of brine water. The presence of the brine water pockets creates a weakness in the ice sheet leading to cracking of the ice. This crack in the ice transfers through the surface of the concrete and removes flakes of concrete progressively, causing salt-scaling.

Valenza and Scherer (2006) proposed that increasing the toughness of the surface helps in reducing salt-scaling. Reducing bleed water using air-entrainer also creates a tougher surface with better salt-scaling resistance. Many lab experiments have shown that conventional concrete without fly ash has better salt-scaling performance than HVFAC (Bilodeau and Malhotra 2000; Mohan Malhotra et al. 2000). However, field studies have shown that salt-scaling performance of HVFAC is acceptable (Malhotra and Mehta 2012; Thomas 2007) even after 15 years of service, and the severity of the lab-based ASTM C672 salt-scaling test has been questioned. Recently, Jones et al. (2013), Prannoy et al. (2018), and Suraneni et al. (2017) have argued that use of fly ash decreases the amount of free calcium hydroxide, which reacts with calcium chloride (one of the commonly used deicing salt) to form expansive calcium oxychloride that reduces the strength of the concrete and creates salt-scaling damage. It is possible that the accelerated test prescribed in ASTM C672 does not allow sufficient time for calcium hydroxide to form calcium oxychloride and thus overestimates the field performance of conventional concrete without fly ash replacement. The calcium oxychloride mechanism has been a concrete pavement joint damage issue and has been shown to be improved with fly ash (Farnam, Zhang, and Weiss 2017; Wang 2014). Thus, general surface scaling of the concrete pavement and joint damage with calcium oxychloride are two different mechanisms and have different trends of improvements with the same variables.

As surface toughness dictates the salt-scaling performance, many different precautions can be taken to reduce the risk of salt-scaling in HVFAC. First, a curing compound should be used to reduce surface moisture loss, which should improve the surface toughness. Other material additives (e.g. nanomaterials) can also be incorporated to improve the bulk strength of concrete as surface toughness is expected to increase with bulk strength. Microfiber-reinforced HVFAC can also be potentially used to reduce scaling (Valenza and Scherer 2006). Moreover, the seasonal construction window using HVFAC may be limited or shortened relative conventional concrete mixtures to ensure that the HVFAC gains sufficient strength before it is exposed to salt-scaling. This is especially important for Class F HVFAC as the strength gain of Class F HVFAC is lower than Class C HVFAC.

Steel Corrosion

Concrete pavement generally has high exposure to chlorine ions from the deicing salts. The chlorine ions, if allowed to penetrate the concrete cover, will corrode the reinforcing steel present in different

joints leading to joint damage and reduction in the pavement's service life. Conventional concrete has free calcium hydroxide, which acts as a pH buffer (at around 12.5) and creates a passive layer on the reinforcing steel for corrosion protection. However, HVFAC does not have any significant free calcium hydroxide as it is consumed by the glassy phases present in the fly ash through pozzolanic reaction to form C-S-H. Even though HVFAC does not have a source for pH buffer, its lower permeability (Malhotra and Mehta 2012) and higher resistivity (Bentz, Tanesi, and Ardani 2013; Lloyd 2017) decreases potential for chlorine ion penetration and corrosion. Lloyd (2017) tested HVFAC with 40% replacement for 19 different fly ash (including four Class C and one Class F ash sourced from the Midwest) and found that the 90 day electric resistivity is much higher than the conventional concrete mix without any fly ash replacement. Ramme and Tharaniyil (2004) measured the chlorine ion permeability of Class C fly ash concrete with increasing fly ash replacement and reported that the 3 month permeability of fly ash concrete is lower than the control mix without any fly ash if the fly ash replacement is kept below 55% by mass.

REFERENCES

Aboustait, Mohammed, Taehwan Kim, M. Tyler Ley, and Jeffrey M. Davis. 2016. "Physical and Chemical Characteristics of Fly Ash Using Automated Scanning Electron Microscopy." *Construction and Building Materials* 106: 1–10. http://dx.doi.org/10.1016/j.conbuildmat.2015.12.098.

Ansari, F, Zhijin Zhang, Allan Luke, and ALi Maher. 1999. *Effects of Synthetic Air Entraining Agents on Compressive Strength of Portland Cement Concrete-Mechanism of Interaction End Remediation Strategy*.

ASTM C138. 2017. "Standard Test Method for Density (Unit Weight), Yield, and Air Content (Gravimetric) of Concrete."

ASTM C173. 2016. "Standard Test Method for Air Content of Freshly Mixed Concrete by the Volumetric Method."

ASTM C191. 2019. "Standard Test Methods for Time of Setting of Hydraulic Cement by Vicat Needle."

ASTM C231. 2017. "Standard Test Method for Air Content of Freshly Mixed Concrete by the Pressure Method." https://doi.org/10.1520/C0231_C0231M-17A.

ASTM C311. 2018. "Standard Test Methods for Sampling and Testing Fly Ash or Natural Pozzolans for Use in Portland-Cement Concrete." https://doi.org/10.1520/C0311_C0311M-18.

ASTM C403. 2016. "Standard Test Method for Time of Setting of Concrete Mixtures by Penetration Resistance." https://doi.org/10.1520/C0403_C0403M-16.

ASTM C457. 2016. "Standard Test Method for Microscopical Determination of Parameters of the Air-Void System in Hardened Concrete."

ASTM C618. 2019. "Standard Specification for Coal Fly Ash and Raw or Calcined Natural Pozzolan for Use in Concrete."

Baltrus, John P., and Robert B. LaCount. 2001. "Measurement of Adsorption of Air-Entraining Admixture on Fly Ash in Concrete and Cement." *Cement and Concrete Research* 31(5): 819–24.

Beckemeier, Karl Wehking. 2012. "Effects of High Volumes of Fly Ash on Cement Paste." Missouti University of Science and Technology.

Bentz, Dale P., Jussara Tanesi, and Ahmad Ardani. 2013. "Ternary Blends for Controlling Cost and Carbon Content: High-Volume Fly-Ash Mixtures Can Be Enhanced with Additions of Limestone Powder." *Concrete International* (August): 51–61.

Bentz, Dale P. 2011. "Powder Additions to Mitigate Retardation in High-Volume Fly Ash Mixtures." *ACI Materials Journal* (107): 508–14. https://www.concrete.org/publications/internationalconcreteabstractsportal/m/details/id/51663971.

Bilodeau, Alain, and Mohan V. Malhotra. 2000. "High-Volume Fly Ash System: Concrete Solution for Sustainable Development." *ACI Structural Journal* 97(1): 41–48.

Bisaillon, Andre, Michel Rivest, and V. M. Malhotra. 1994. "Performance of High-Volume Fly Ash Concrete in Large Experimental Monoliths." *ACI Materials Journal* 91(2): 178–87.

Bleszynski, Roland F, and Michael D. A. Thomas. 1998. “Microstructural Studies of Alkali-Silica Reaction in Fly Ash Concrete Immersed in Alkaline Solutions.” *Advanced Cement Based Materials* 7(2): 66–78.

Bruere, G. M. 1970. “Air-Entraining Actions of Anionic Surfactants in Portland Cement Pastes.” *Journal of Applied Chemistry and Biotechnology* 21(3): 61–64.

Buchan, G D, K S Grewal, J J Claydon, and R J Mcpherson. 1993. “A Ccomparison of Sedigraph and Pipette Methods for Soil Particle-Size Analysis.” *Soil Research* 31(4): 407–17. https://doi.org/10.1071/SR9930407.

Bullard, Jeffrey W et al. 2011. “Mechanisms of Cement Hydration.” *Cement and Concrete Research* 41(12): 1208–23. http://www.sciencedirect.com/science/article/pii/S0008884610002152.

Chancey, Ryan Thomas. 2008. “Characterization of Crystalline and Amorphous Phases and Respective Reactivities in a Class F Fly Ash.” University of Texas, Austin. http://hdl.handle.net/2152/18003.

Chen, Xu et al. 2002. “Fly Ash Benefication With Ozone: Mechanism of Adsorption Supression.” *Fuel Chemistry Division Preprints* 47(2): 843–44. https://web.anl.gov/PCS/acsfuel/preprint archive/Files/47_2_Boston_10-02_0251.pdf.

———. 2003. “Mechanisms of Surfactant Adsorption on Non-Polar, Air-Oxidized and Ozone-Treated Carbon Surfaces.” *Carbon* 41(8): 1489–1500.

Chen, Y et al. 2005. “Characterization of Ultrafine Coal Fly Ash Particles by Energy-Filtered TEM.” *Journal of Microscopy* 217(3): 225–34. https://onlinelibrary.wiley.com/doi/abs/10.1111/j.1365-2818.2005.01445.x.

Chung, H S, and R Hogg. 1985. “The Effect of Brownian Motion on Particle Size Analysis by Sedimentation.” *Powder Technology* 41(3): 211–16. http://www.sciencedirect.com/science/article/pii/0032591085800164.

Cyr, M, and A Tagnit-Hamou. 2001. “Particle Size Distribution of Fine Powders by LASER Diffraction Spectrometry. Case of Cementitious Materials.” *Materials and Structures* 34(6): 342–50. https://doi.org/10.1007/BF02486485.

Davis, Raymond E., Roy W Carlson, J. W. Kelly, and Harmer E Davis. 1937. “Properties Of Cements And Concretes Containing Fly Ash.” *ACI Journal Proceedings* 33(5).

Deng, Shuang et al. 2016. “Chemical Forms of the Fluorine, Chlorine, Oxygen and Carbon in Coal Fly Ash and Their Correlations with Mercury Retention.” *Journal of Hazardous Materials* 301: 400–406. http://dx.doi.org/10.1016/j.jhazmat.2015.09.032.

Diaz-Loya, Ivan, Maria Juenger, Saamiya Seraj, and Rafic Minkara. 2019. “Extending Supplementary Cementitious Material Resources: Reclaimed and Remediated Fly Ash and Natural Pozzolans.” *Cement and Concrete Composites* 101: 44–51.

Dodson, Vance H. 1990. “Air Entraining Admixtures.” In *Concrete Admixtures*, Boston, MA: Springer US, 129–58. http://link.springer.com/10.1007/978-1-4757-4843-7.

Dolch, William L. 1996. “Air-Entraining Admixtures.” In *Concrete Admixtures Handbook*, ed. V. S. Ramachandran. Park Ridge, NJ: William Andrew Publishing, 518–57.

Du, Lianxiang, and Kevin J Folliard. 2005. “Mechanisms of Air Entrainment in Concrete.” *Cement and Concrete Research* 35(8): 1463–71. http://www.sciencedirect.com/science/article/pii/S0008884604003369.

DUNSTAN, M R H. 1983. “DEVELOPMENT OF HIGH FLYASH CONTENT CONCRETE.” *Proceedings of the Institution of Civil Engineers* 74(3): 495–513. https://doi.org/10.1680/iicep.1983.1407.

Durdziński, Paweł T., Cyrille F. Dunant, Mohsen Ben Haha, and Karen L. Scrivener. 2015. “A New Quantification Method Based on SEM-EDS to Assess Fly Ash Composition and Study the Reaction of Its Individual Components in Hydrating Cement Paste.” *Cement and Concrete Research* 73: 111–22.

Fan, M., and R. C. Brown. 2001. “Comparison of the Loss-on-Ignition and Thermogravimetric Analysis Techniques in Measuring Unburned Carbon in Coal Fly Ash.” *Energy and Fuels* 15(6): 1414–17.

Farnam, Yaghoob, Bochen Zhang, and Jason Weiss. 2017. “Evaluating the Use of Supplementary Cementitious Materials to Mitigate Damage in Cementitious Materials Exposed to Calcium Chloride Deicing Salt.” *Cement and Concrete Composites* 81: 77–86. http://dx.doi.org/10.1016/j.cemconcomp.2017.05.003.

Freeman, Elizabeth, Yu-Ming Gao, Robert Hurt, and Eric Suuberg. 1997. “Interactions of Carbon-Containing Fly Ash with Commercial Air-Entraining Admixtures for Concrete.” *Fuel* 76(8): 761–65.

Gao, Y. et al. 2001. “Ozonation for the Chemical Modification of Carbon Surfaces in Fly Ash.” *Fuel* 80(5): 765–68.

Gao, Yu Ming et al. 1997. “Effects of Carbon on Air Entrainment in Fly Ash Concrete: The Role of Soot and Carbon Black.” *Energy and Fuels* 11(2): 457–62.

Gołaszewski, Jacek, Aleksandra Kostrzanowska-Siedlarz, Tomasz Ponikiewski, and Patrycja Miera. 2017. “Influence of Cements Containing Calcareous Fly Ash as a Main Component Properties of Fresh Cement Mixtures.” *{IOP} Conference Series: Materials Science and Engineering* 245: 22099. https://doi.org/10.1088%2F1757-899x%2F245%2F2%2F022099.

Gutmann, Paul F. 1987. “Bubble Characteristics as They Pertain to Compressive Strength and Freeze-Thaw Durability.” *MRS Proceedings* 114: 271.

Hackley, Vincent A., Lin-Sien Lum, Vadas Gintautas, and Chiara F. Ferraris. 2004. *Particle Size Analysis by Laser Diffraction Spectrometry: Application to Cementitious Powders*. https://www.nist.gov/publications/particle-size-distribution-laser-diffraction-spectrometry-application-cementitious.

Harris, Nathan J, Kenneth C Hover, Kevin J Folliard, and M Tyler Ley. 2008a. “The Use of the Foam Index Test to Predict Air-Entraining Admixture Dosage in Concrete Containing Fly Ash: Part I—Development of a Standard Test Method: Proportions of Materials.” *Journal of ASTM International* 5(7): 101603.

Harris, Nathan J, Kenneth C Hover, Kevin J Folliard, and Tyler M Ley. 2008b. “The Use of the Foam Index Test to Predict Air-Entraining Admixture Dosage in Concrete Containing Fly Ash: Part II—Development of a Standard Test Method: Proportions of Materials.” *Journal of ASTM International* 5(7): 101603.

———. 2008c. “The Use of the Foam Index Test to Predict Air-Entraining Admixture Dosage in Concrete Containing Fly Ash: Part III—Development of a Standard Test Method: Proportions of Materials.” *Journal of ASTM International* 5(7): 101603.

Hemmings, R T, and E E Berry. 1987. “On the Glass in Coal Fly Ashes: Recent Advances.” *MRS Proceedings* 113: 3. https://www.cambridge.org/core/article/on-the-glass-in-coal-fly-ashes-recent-advances/4A82EBCDE024CD85639DDC7B5BEDEFD8.

Hirokawa, K., and Y. Danzaki. 1984. “Analytical Application of XPS for Surface Characterization of Coal Fly Ash and Coal.” *Surface and Interface Analysis* 6(4): 193–95.

Hong, Sung-Yoon, and F P Glasser. 2002. “Alkali Sorption by C-S-H and C-A-S-H Gels: Part II. Role of Alumina.” *Cement and Concrete Research* 32(7): 1101–11. http://www.sciencedirect.com/science/article/pii/S0008884602007536.

Hu, Jiong, Zhi Ge, and Kejin Wang. 2014. “Influence of Cement Fineness and Water-to-Cement Ratio on Mortar Early-Age Heat of Hydration and Set Times.” *Construction and Building Materials* 50: 657–63. http://dx.doi.org/10.1016/j.conbuildmat.2013.10.011.

Hubbard, F H, R K Dhir, and M S Ellis. 1985. “Pulverized-Fuel Ash for Concrete: Compositional Characterisation of United Kingdom PFA.” *Cement and Concrete Research* 15(1): 185–98. http://www.sciencedirect.com/science/article/pii/0008884685900250.

Jiang, L H, and V M Malhotra. 2000. “Reduction in Water Demand of Non-Air-Entrained Concrete Incorporating Large Volumes of Fly Ash.” *Cement and Concrete Research* 30(11): 1785–89. http://www.sciencedirect.com/science/article/pii/S0008884600003975.

Jolicoeur, Carmel et al. 2009. “Mode of Action of Anionic Surfactants for Air Entrainment in Cement Pastes W-w/o Fly Ash.” In *3rd World of Coal Ash, WOCA Conference - Proceedings*, , 1–19.

Jones, Wesley et al. 2013. *An Overview of Joint Deterioration in Concrete Pavement: Mechanisms, Solution Properties, and Sealers*. West Lafayette, Indiana. http://docs.lib.purdue.edu/jtrpaffdocs/4/.

Kim, Taehwan et al. 2019. “Using Particle Characterization to Study Fly Ash Dissolution and Leaching in Water and KOH Solution.” *ACI Materials Journal* 116(4): 5–17.

———. 2020. “Using Particle Composition of Fly Ash to Predict Concrete Strength and Electrical Resistivity.” *Cement and Concrete Composites* 107(September 2019): 103493. https://doi.org/10.1016/j.cemconcomp.2019.103493.

Konarski, P., A. Zawada, D. Kowalczyk, and K. Juda-Rezler. 2013. “Core-Shell Structure of Fly Ash Particles - SIMS Depth Profile Analysis.” *Surface and Interface Analysis* 45(1): 592–95.

Külaots, Indrek, Robert H. Hurt, and Eric M. Suuberg. 2004. “Size Distribution of Unburned Carbon in Coal Fly Ash and Its Implications.” *Fuel* 83(2): 223–30.

Kutchko, Barbara G, and Ann G Kim. 2006. “Fly Ash Characterization by SEM–EDS.” *Fuel* 85(17): 2537–44. http://www.sciencedirect.com/science/article/pii/S0016236106001906.

Ley, M. Tyler, David Welchel, Jacob Peery, and Jake LeFlore. 2017. “Determining the Air-Void Distribution in Fresh Concrete with the Sequential Air Method.” *Construction and Building*

Materials 150: 723–37. http://dx.doi.org/10.1016/j.conbuildmat.2017.06.037.

Ley, M Tyler. 2010. “Determining the Air-Entraining Admixture Dosage Response for Concrete with a Single Concrete Mixture.” *Journal of ASTM International* 7(2): 1–11.

Li, Chuanhai et al. 2019. “The Effect of Gypsum on the Hydration of Alite–Belite–Ferrite Phase System.” *Journal of Thermal Analysis and Calorimetry* 136(2): 717–24. https://doi.org/10.1007/s10973-018-7643-7.

Lindfors, Paul A, and Claire T Hovland. 1978. “Surface Chemical Analysis of Particles by Auger Electron Spectroscopy and ESCA.” In *Environmental Pollutants: Detection and Measurement*, eds. Taft Y Toribara, James R Coleman, Barton E Dahneke, and Isaac Feldman. Boston, MA: Springer US, 349–63. https://doi.org/10.1007/978-1-4613-4033-1_20.

Lloyd, Zane. 2017. “Investigation of the Quality Control of Waste Products for Concrete.” Oklahoma State University.

Malhotra, V. M., and P. K. Mehta. 2012. *High-Performance High-Volume Fly Ash Concrete for Building Sustainable and Durable Structures*. Fourth. Ottawa, ON, Canada.

Malhotra, V. Mohan, Paul H. Read, John Ryell, and Min-Hong Zhang. 2000. “Long-Term Mechanical Properties and Durability Characteristics of High-Strength/High-Performance Concrete Incorporating Supplementary Cementing Materials under Outdoor Exposure Conditions.” *ACI Materials Journal* 97(5): 518–25.

Malhotra, V M. 2002. “High-Performance High-Volume Fly Ash Concrete.” *Concrete International* 24(7): 30–34.

Mehta, P. K. 2004. “HIGH-PERFORMANCE, HIGH-VOLUME FLY ASH CONCRETE FOR SUSTAINABLE DEVELOPMENT.” In *Proceedings of the International Workshop on Sustainable Development and Concrete Technology*, Beijing, China.

Mielenz, Richard C, Vladimir E Wolkodofu, James E Backstrom, and Harry L Flack. 1958. “Origin , Evolution , and Effects of the Air Void System in Concrete . Part 1- Entrained Air in Unhardened Concrete.” *Journal of the American Concrete Institute* 55(5): 95–121.

Minard, Helene, Sandrine Garrault, Laure Regnaud, and Andre Nonat. 2007. “Mechanisms and Parameters Controlling the Tricalcaium Aluminate Reactivity in the Presence of Gypsum.” *Cement and Concrete Research* 37: 1418–28.

Nagi, Mohamad A., Paul A. Okamoto, Ronald L. Kozikowski, and Kenneth Hover. 2007. NCHRP Report 578 *Evaluating Air-Entraining Admixtures for Highway Concrete*.

Naik, Tarun R, and Bruce W Ramme. 1987. “Low Cement Content High Strength Concrete.” *Cement and Concrete Research* 17(2): 283–94. http://www.sciencedirect.com/science/article/pii/0008884687901116.

Naik, Tarun R, Shiw Singh, and Bruce Ramme. 1998. “Mechanical Properties and Durability of Concrete Made with Blended Fly Ash.” *ACI Materials Journal* 95(4): 454–60. http://www.concrete.org/Publications/ACIMaterialsJournal/ACIJournalSearch.aspx?m=details&ID=388.

Naik, Tarun, and Bruce W. Ramme. 1989. “High-Strength Concrete Containing Large Quantities of Fly Ash.” *ACI Materials Journal* 86(2): 111–16.

Nathan, Y, M Dvorachek, I Pelly, and U Mimran. 1999. “Characterization of Coal Fly Ash from Israel.” *Fuel* 78(2): 205–13. http://www.sciencedirect.com/science/article/pii/S0016236198001446.

Oey, Tandre. 2019. “Controlling the Reactivity of Silicate and Aluminate Glasses in Aqueous Alkaline Environments.” University of California Los Angeles.

Oey, Tandré et al. 2017. “An Improved Basis for Characterizing the Suitability of Fly Ash as a Cement Replacement Agent.” *Journal of the American Ceramic Society* 100(10): 4785–4800. https://ceramics.onlinelibrary.wiley.com/doi/abs/10.1111/jace.14974.

Öztürk, T, O Kroggel, P Grübl, and J S Popovics. 2006. “Improved Ultrasonic Wave Reflection Technique to Monitor the Setting of Cement-Based Materials.” *NDT & E International* 39(4): 258–63. http://www.sciencedirect.com/science/article/pii/S0963869505001556.

Pedersen, K. H., A. D. Jensen, M. S. Skjøth-Rasmussen, and K. Dam-Johansen. 2008. “A Review of the Interference of Carbon Containing Fly Ash with Air Entrainment in Concrete.” *Progress in Energy and Combustion Science* 34(2): 135–54.

Phillips, William Joseph. 2015. “Alkali SIlica Reaction Using High Volume Class C FLy Ash.” University of Arkansas.

Pourchet, Sylvie, Cedric Comparet, A Nonat, and Philippe Maitrasse. 2006. “Influence of Three Types of Superplasticizers on Tricalciumaluminate Hydration in Presence of Gypsum.” In *8th CANMET/ACI International Conference on Superplasticizers and Other Chemical Admixtures in Concrete.*, Sorrento, Italy, 151–58.

Prannoy, Suraneni, Azad Vahid Jafari, Isgor O Burkan, and Weiss Jason. 2018. “Role of Supplementary Cementitious Material Type in the Mitigation of Calcium Oxychloride Formation in Cementitious Pastes.” *Journal of Materials in Civil Engineering* 30(10): 4018248. https://doi.org/10.1061/(ASCE)MT.1943-5533.0002425.

Quennoz, Alexandra, and Karen L. Scrivner. 2012. “Hydration of C3A-Gypsum Systems.” *Cement and Concrete Research* 42: 1032–41. https://doi.org/10.1016/j.cemconres.2012.04.005.

Ramme, Bruce W., and Mathew P. Tharaniyil. 2004. *We Energies Coal COmbustion Products Utilization Handbook*. 2nd ed. We Energies.

Reinhardt, H W, C U Große, and A T Herb. 2000. “Ultrasonic Monitoring of Setting and Hardening of Cement Mortar—A New Device.” *Materials and Structures* 33(9): 581–83. https://doi.org/10.1007/BF02480539.

Roise, Charlene. 2018. “A Mid-Century MONOLITH in Northwestern Montana: The Hungry Horse Dam Project.” *Montana: The Magazine of Western History* 68(2): 45. https://sfx.carli.illinois.edu/sfxuiu?url_ver=Z39.88-2004&rft_val_fmt=info%3Aofi%2Ffmt%3Akev%3Amtx%3Ajournal&genre=article&sid=ProQ%3AProQ%3A&atitle=A Mid-Century MONOLITH in Northwestern Montana%3A The Hungry Horse Dam Project&title=Montana%3B The Magazi.

Şahin, Y., Y. Akkaya, F. Boylu, and M. A. Taşdemir. 2017. “Characterization of Air Entraining Admixtures in Concrete Using Surface Tension Measurements.” *Cement and Concrete Composites* 82: 95–104.

Sakamoto, Tetsuo et al. 2004. “Structural Analysis of Coal Fly Ash Particles by Means of Focused-Ion-Beam Time-of-Flight Mass Spectrometry.” *e-Journal of Surface Science and Nanotechnology* 2(February): 45–51.

Sen, Du, Shi Xianming, and Ge Yong. 2017. “Electron Probe Microanalysis Investigation into High-Volume Fly Ash Mortars.” *Journal of Materials in Civil Engineering* 29(7): 4017043. https://doi.org/10.1061/(ASCE)MT.1943-5533.0001854.

Shafaatian, Seyed M.H., Alireza Akhavan, Hamed Maraghechi, and Farshad Rajabipour. 2013. “How Does Fly Ash Mitigate Alkali-Silica Reaction (ASR) in Accelerated Mortar Bar Test (ASTM C1567)?” *Cement and Concrete Composites* 37(1): 143–53. http://dx.doi.org/10.1016/j.cemconcomp.2012.11.004.

Siddique, Rafat. 2004. “Performance Characteristics of High-Volume Class F Fly Ash Concrete.” *Cement and Concrete Research* 34(3): 487–93. http://www.sciencedirect.com/science/article/pii/S0008884603003107.

Sivasundaram, V., G. G. Carette, and V. M. Malhotra. 2005. “Properties of Concrete Incorporating Low Quantity of Cement and High Volumes of Low-Calcium Fly Ash.” *ACI Symposium Publication* 4(5): 45–71.

Somorjai, Gabor A., and Yimin Li. 2010. *Introduction to Surface Chemistry and Catalysis*. 2nd ed. Wiley.

Stencel, John M., Haiping Song, and Federico Cangialosi. 2009. “Automated Foam Index Test: Quantifying Air Entraining Agent Addition and Interactions with Fly Ash-Cement Admixtures.” *Cement and Concrete Research* 39(4): 362–70.

Suraneni, Prannoy, Vahid J. Azad, O. Burkan Isgor, and W. Jason Weiss. 2017. “Use of Fly Ash to Minimize Deicing Salt Damage in Concrete Pavements.” *Transportation Research Record* 2629(2629): 24–32.

Sutter, Lawrence, R. Douglas Hooton, and Scott Schlorholtz. 2013. *NCHRP Report 749: Methods for Evaluating Fly Ash for Use in Highway Concrete*. https://www.nap.edu/catalog/22483.

Tanikella, Prasanth, and Jan Olek. 2017. *Updating Physical and Chemical Characteristics of Fly Ash for Use in Concrete*. West Lafayette, IN: Joint Transportation Research Program Publication No. FHWA/IN/JTRP-2017/11.

Taylor, P. et al. 2006. “Identifying Incompatible Combinations of Concrete Materials : Volume I, Final Report.” ed. CTLGroup. https://rosap.ntl.bts.gov/view/dot/727.

Taylor, Peter C. et al. 2006. FHWA-HRT-0 *Identifying Incompatible Combinations of Concrete Materials : Volume II — Test Protocol*.

Thomas, Micheal. 2007. *Optimizing the Use of Fly Ash in Concrete*. https://www.cement.org/docs/default-source/fc_concrete_technology/is548-optimizing-the-use-

of-fly-ash-concrete.pdf.

Tran, Quang, and Jeffery R. Roesler. 2020. “Noncontact Ultrasonic and Computer Vision Assessment for Sawcut Initiation Time.” *Journal of Transportation Engineering, Part B: Pavements* 146(3): 04020055.

Valenza, J J, and G W Scherer. 2005. “Mechanisms of Salt Scaling.” *Materials and Structures* 38(4): 479–88. https://doi.org/10.1007/BF02482144.

Valenza, John J., and George W. Scherer. 2006. “Mechanism for Salt Scaling.” *Journal of the American Ceramic Society* 89(4): 1161–79.

———. 2007a. “A Review of Salt Scaling: I. Phenomenology.” *Cement and Concrete Research* 37(7): 1007–21. http://www.sciencedirect.com/science/article/pii/S0008884607000737.

———. 2007b. “A Review of Salt Scaling: II. Mechanisms.” *Cement and Concrete Research* 37(7): 1022–34.

Wang, Xin. 2014. *Evaluation of De-Icer Deterioration of Concrete*.

———. 2019. “A Modified Foam Drainage Test Protocol for Assessing Incompatibility of Admixture Combinations and Stability of Air Structure in Cementitious Systems.” *Construction and Building Materials* 211: 174–84. http://www.sciencedirect.com/science/article/pii/S0950061819306294.

Watkins, Melanie Kueber, Zeyad Ahmed, Lawrence Sutter, and David Hand. 2015. “Characterization of Coal Fly Ash by Absolute Foam Index.” *ACI Materials Journal* 112(3): 393–98.

Yoon, Seyoon et al. 2014. “Statistical Evaluation of the Mechanical Properties of High-Volume Class F Fly Ash Concretes.” *Construction and Building Materials* 54: 432–42. http://www.sciencedirect.com/science/article/pii/S0950061813012348.

Yu, J. et al. 2000. “Adsorptive and Optical Properties of Fly Ash from Coal and Petroleum Coke Co-Firing.” *Energy and Fuels* 14(3): 591–96.

APPENDIX B: HVFAC TRIAL BATCHING AND CHARACTERIZATION

A HVFAC trial mix was batched and cast at the IDOT laboratory to demonstrate the applicability of maturity method to HVFAC, and to have a reference mix design available for proposed field test sections. The IDOT laboratory measured strength, temperature data, and fresh properties of the HVFAC. The UIUC laboratory completed XRF, calorimeter, and foam index tests of the mixes. This HVFAC trial mix was supposed to be part of a field test section that was to be instrumented but it was later cancelled.

CHARACTERIZATION

XRF data of the cement and fly ash sample to be used in this project are shown in Table 22. The foam index of the fly ash was found to be 2.5 μL AEA/gm fly ash.

Table 22. Major Oxide Composition of Cement and Fly Ash

	Cement	Fly Ash
SiO_2	19.42	35.77
CaO	65.61	27.62
Al_2O_3	3.31	17.98
Fe_2O_3	3.85	6.59
MgO	1.59	5.74
SO_3	4.33	3.34
K_2O	0.90	0.44

Calorimeter tests indicated that the water reducer dosage amount significantly affect the setting time compared to the AEA dosage (Figure 44). A noncontact ultrasound method (Tran and Roesler 2020) was used to determine the final setting time of mortar mixtures with this fly ash and cement. The comparison of the setting times obtained from the mortar based noncontact ultrasound method and the paste-based calorimeter test is shown in Table 23. Despite the setting times obtained from noncontact ultrasound differing from the setting times obtained from calorimeter, they both followed the same trend between the two mixtures tested.

Table 23. Comparison of Final Setting Time Measured by Noncontact Ultrasound and Calorimeter

Mix Name	Calorimeter Setting Time (hr)	Noncontact Ultrasound Setting Time (hr)
Cement + 40% Fly Ash + Target AEA + Target Water Reducer	13	12
Cement + 40% Fly Ash	10	8

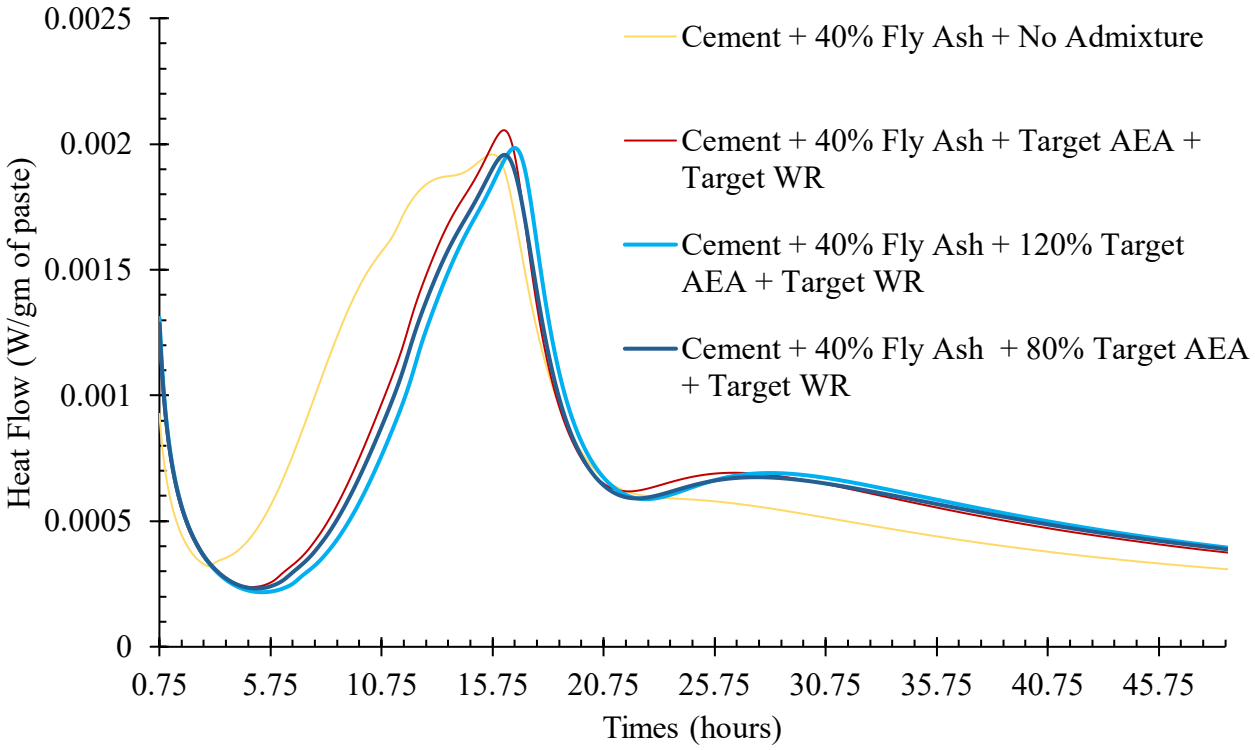

A. Effect of changing AEA dosage on HVAC hydration

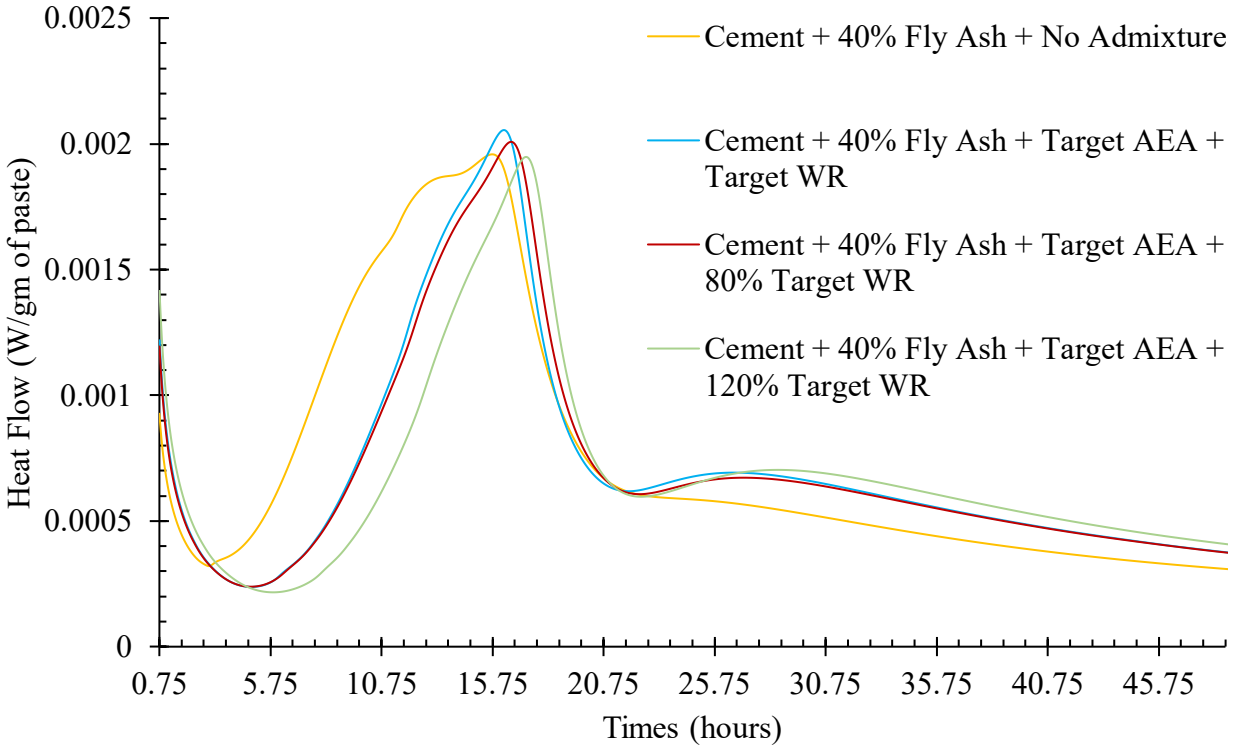

B. Effect of changing water-reducer dosage on HVFAC hydration

Figure 44. Graphs. Effect of changing AEA dosage (a) and water-reducer dosage (b) on HVFAC hydration.

HVFAC CONCRETE MIX PROPERTIES

The basic mix design was produced by Hahn Ready Mix Group (Table 24). The mix design is described as "low slump" with "optimized aggregate." The quantities for the HVFA test mix are simply based on increasing the fly ash replacement from 25% to 40% (and adjusting the sand content accordingly). Two trial batches were mixed, the first one was used to determine the AEA content to obtain ~6% air content, and the second mix was used to obtain a time-temperature-strength relationship.

The 1.25 ft^3 first trial batch was mixed without AEA, and then the AEA dosage was increased until achieving the optimum air content. The unit weight of the concrete with each AEA dosage increment was measured to roughly track the change in air content with AEA dosage increment (Table 25). After a decrease in 6-7% unit weight, the air content was verified using a Type B air meter, and six 4x8-in. cylindrical strength specimens were made to measure compressive strength at 7 and 14 days (Table 26). The concrete was re-mixed for 2 minutes after each AEA dosage increment.

Table 24. HVFAC Mix Design for Trial Batching

Mix Constituents	82PCCH935 (pcy)	HVFAC Test Mix (pcy)
Cement (3.15)	435	350
Fly Ash, Class C (2.79)	145	235
Sand (2.65)	1268	1250
¾" Cr. Stone (2.71)	1189	1189
½" Cr. Stone (2.72)	657	657
Water	225	225
w/c	0.41	0.41
Air	6.5%	6.5%

Table 25. Change in Unit Weight with AEA Dosage Increment

Unit Weight (pcf)	% Change from Initial	Total AEA (mL)	AEA Dosage Increment (mL)
152.76	–	0	3.9
150.36	−1.57%	3.9	8.0
146.68	−3.98%	11.9	8.0
143.56	−6.02%	19.9	–

Table 26. Trial Batch 1 Test Data for HVFAC Field Section

Unit Weight (pcf)	Type B Air Content (%)	SAM Air Content (%)	SAM No.	Slump (in.)	Compressive Strength (psi)
143.56	8.8	9.1	0.22	1.00	3860 @ 7d 4825 @14d

The second 1.75 ft^3 batch was mixed with 20 mL AEA dosage (1.8 oz/cwt) instead of 28 mL (2.5 oz/cwt) as used in Trial Batch 1 because of concerns regarding incremental dosage and repeated mixing overestimating the required AEA dosage. Multiple 4x8-in. cylindrical strength specimens were cast to measure compressive strength up to 56 days (Table 27). Trial Batch 2 mix had sufficient air content and strength, but not sufficient workability because water reducer was not added. One wireless thermocouple sensor was installed in the middle of two cylinders to measure the change in temperature over time as well. The evolution of temperature with time is shown in Figure 45. The Nurse-Saul Equation (Figure 46) was used for constructing the maturity calibration curve. In the Nurse-Saul equation, $M(t)$ is Temperature-time factor, T_a is the average concrete temperature in time interval Δt, T_o is datum temperature = 0°C, Δt is temperature data collection interval = 15 min. Nurse-Saul equation (Figure 47) was able to provide a maturity calibration curve which can be used for strength prediction (Figure 47).

Table 27. Trial Batch 2 Test Data for HVFAC Field Section

Unit Weight (pcf)	Type B Air Content (%)	SAM Air Content (%)	SAM No.	Slump (in.)	Compressive Strength (psi)
148.64	6.5	5.9	0.16	0.00	2760 @ 1d 5360 @ 4d 6110 @ 7d 6981 @ 14d 7831 @ 28d 8798 @ 56d

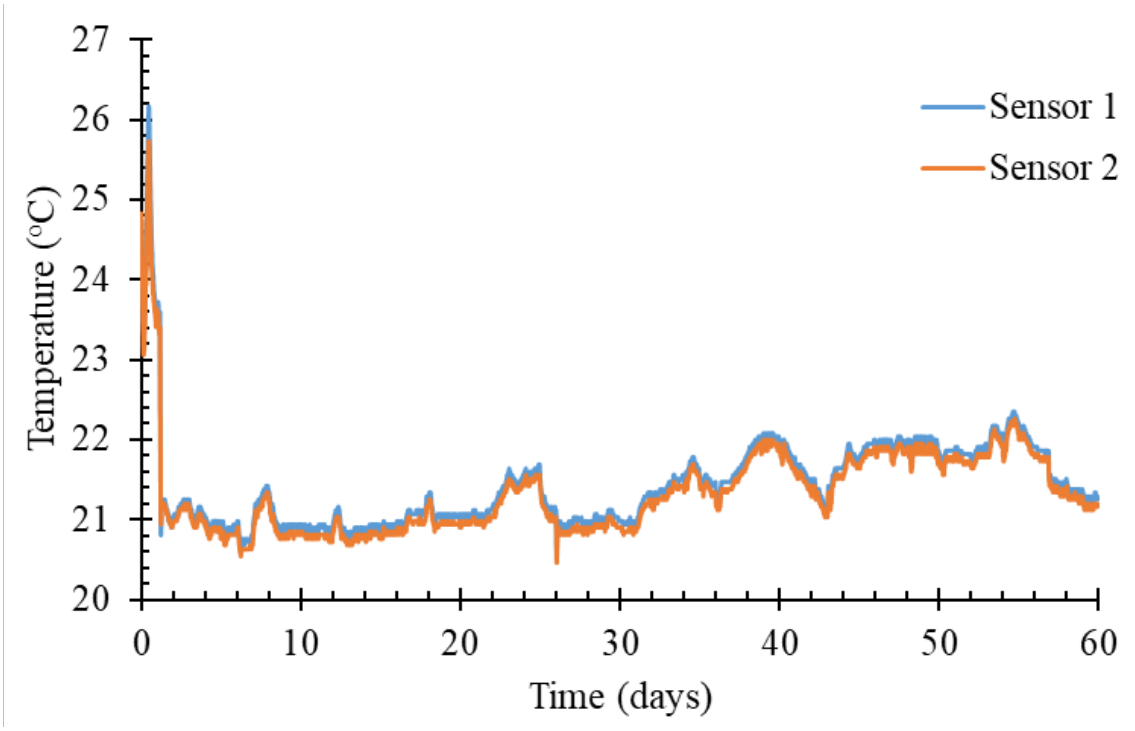

Figure 45. Graph. Change in HVFAC temperature over time.

$$M(t) = \sum (T_a - T_o)\Delta t$$

Figure 46. Equation. Nurse-Saul equation for maturity calculation.

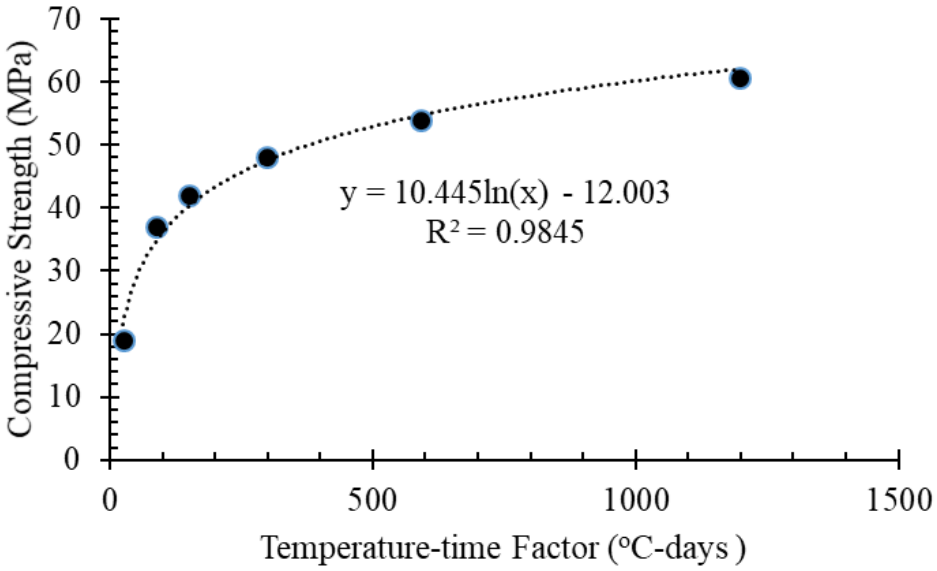

Figure 47. Graph. Maturity calibration curve for specific HVFAC mix.

APPENDIX C: CUMMULATIVE HEAT FLOW GRAPHS FOR HVFAC MIXES WITH LIMESTONE

The cumulative heat flow graphs for the some of the mixes containing micro- and nano-limestone mixes are provided below.

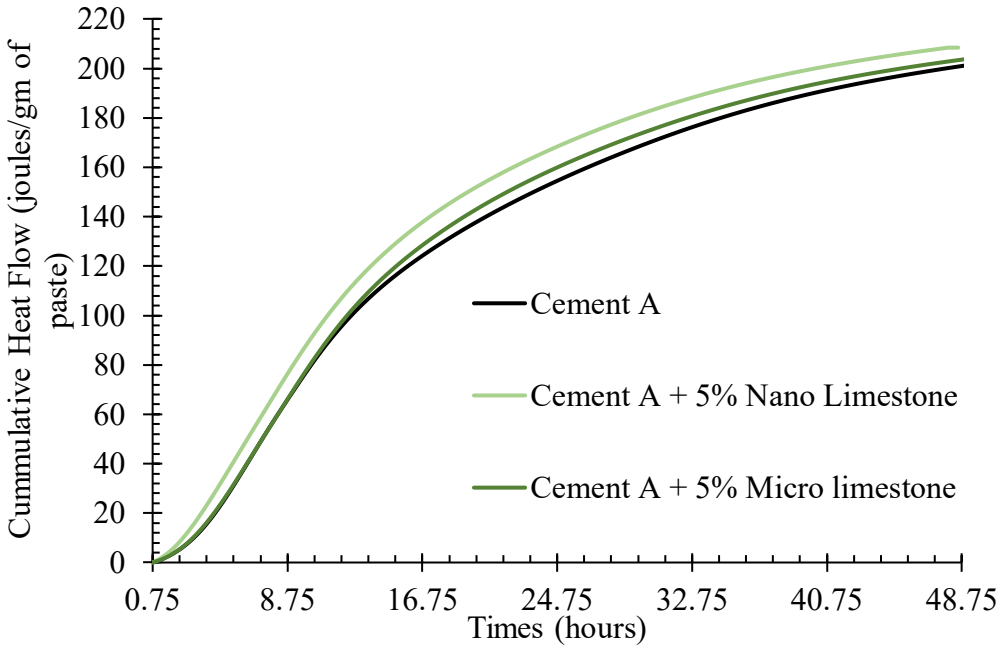

A. 5% replacement

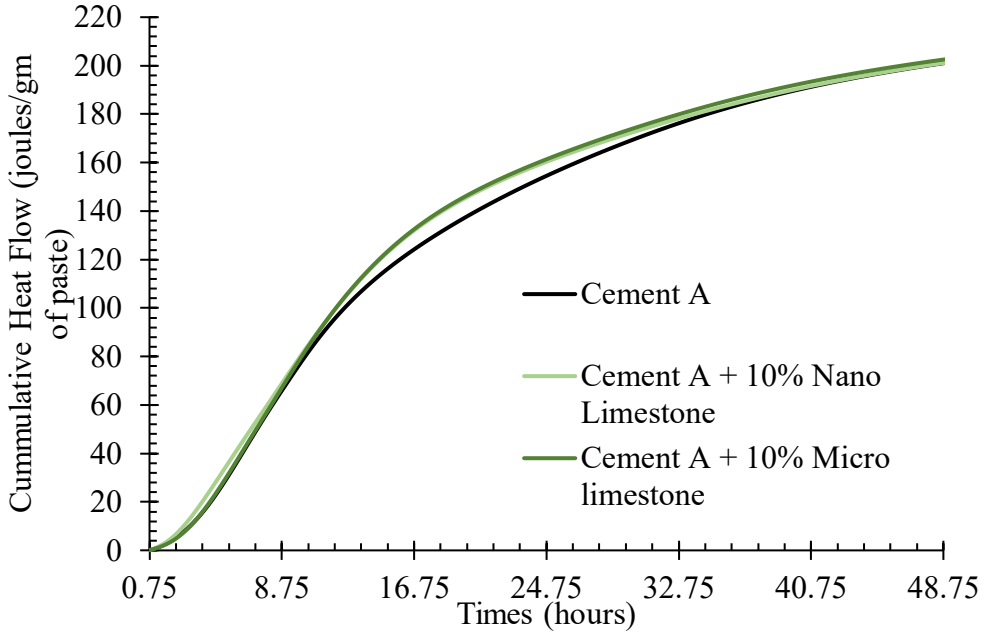

B. 10% replacement

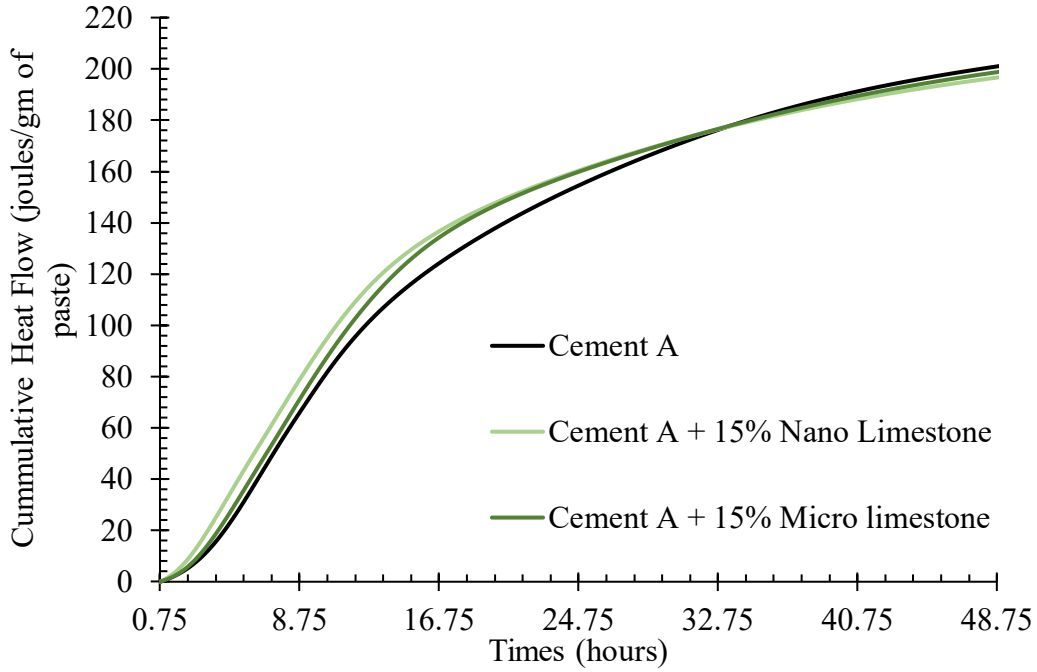

C. 15% replacement

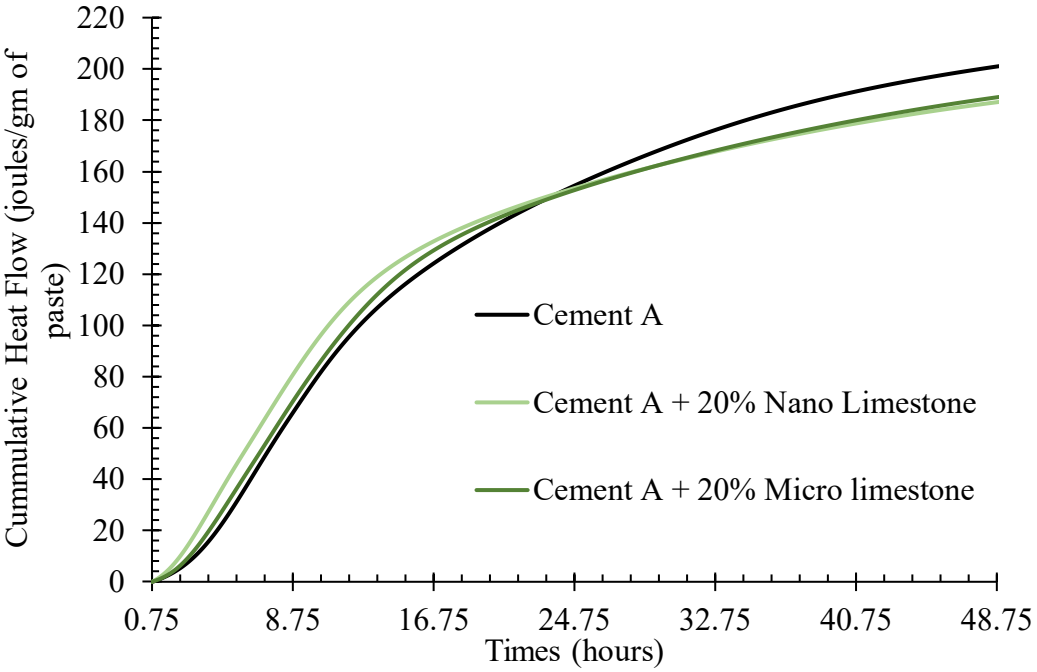

D. 20% replacement

Figure 48. Graphs. Effect of micro- and nano-limestone replacement on cumulative heat flow for different cement replacement rates of (a) 5%, (b) 10%, (c) 15%, and (d) 20%.

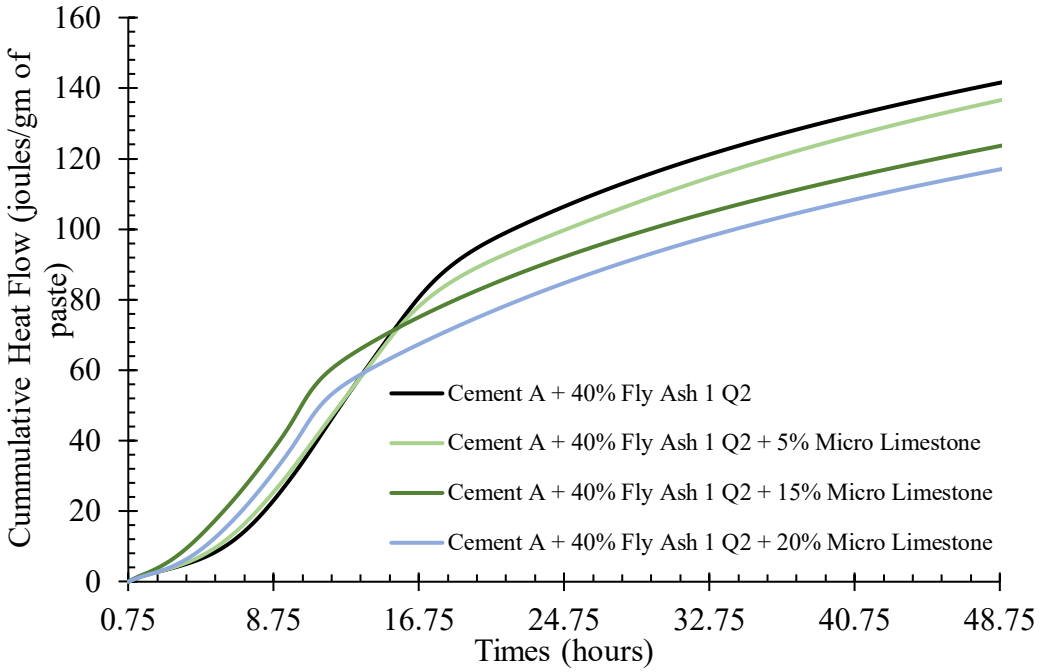

A. Fly Ash 1

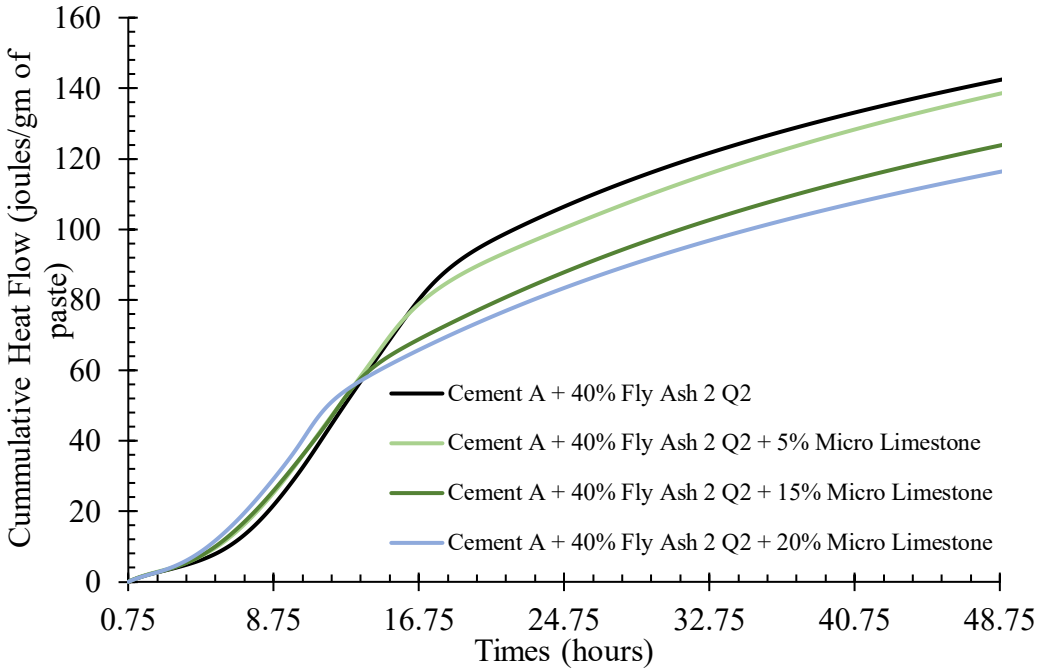

B. Fly Ash 2

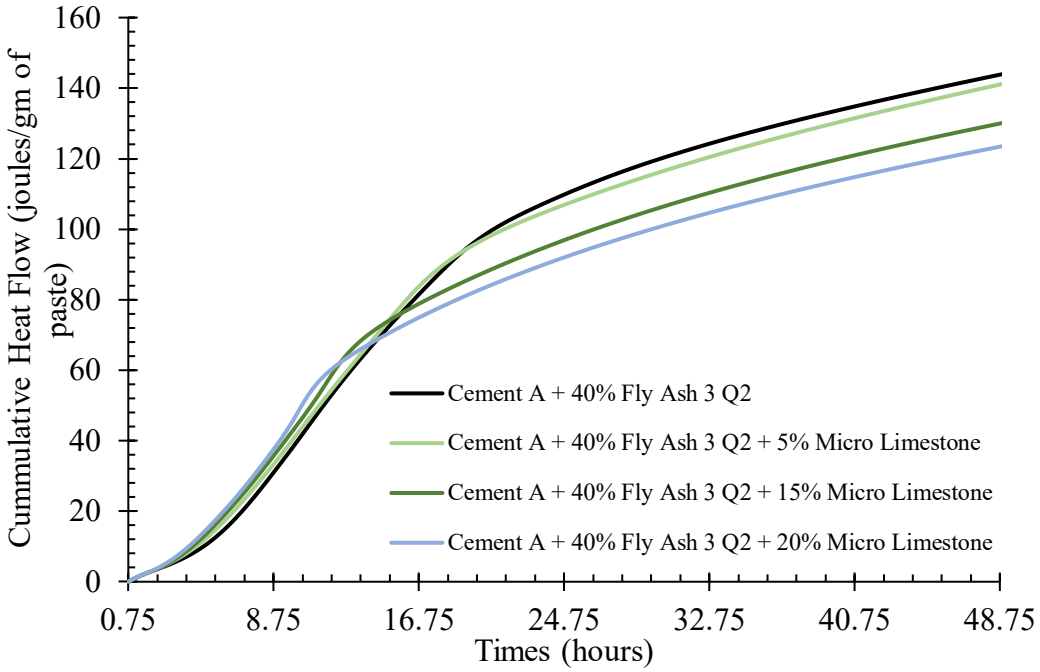

C. Fly Ash 3

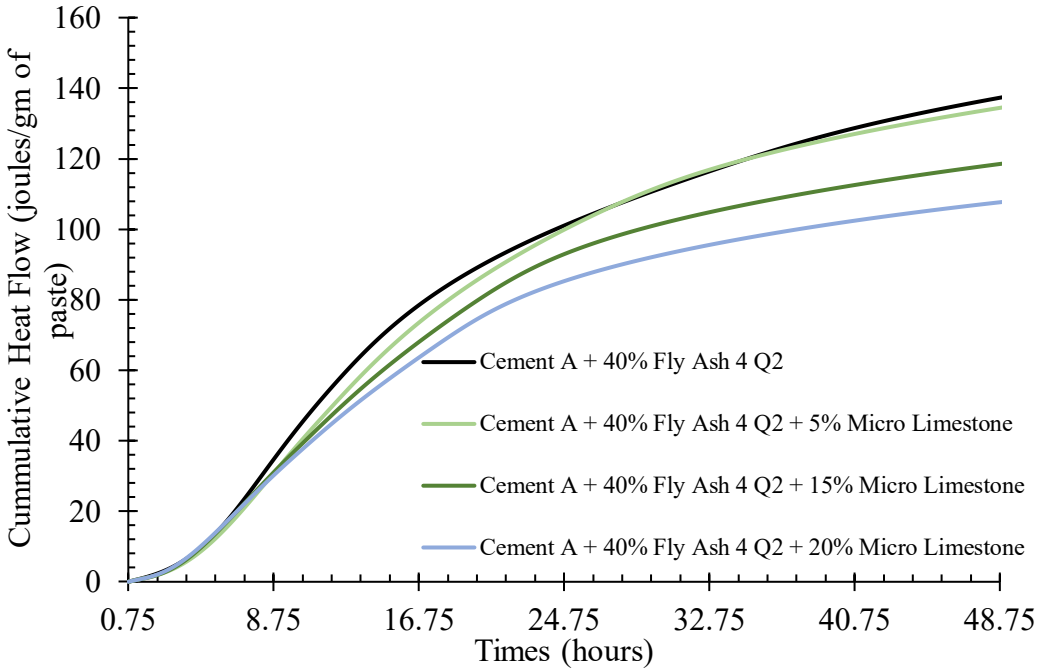

D. Fly Ash 4

Figure 49. Graphs. Effect of increasing micro-limestone replacement on cumulative heat flow for 40% weight replacement of cement with (a) Fly Ash 1, (b) Fly Ash 2, (c) Fly Ash 3, and (d) Fly Ash 4 for 2019 Quarter 2 samples.

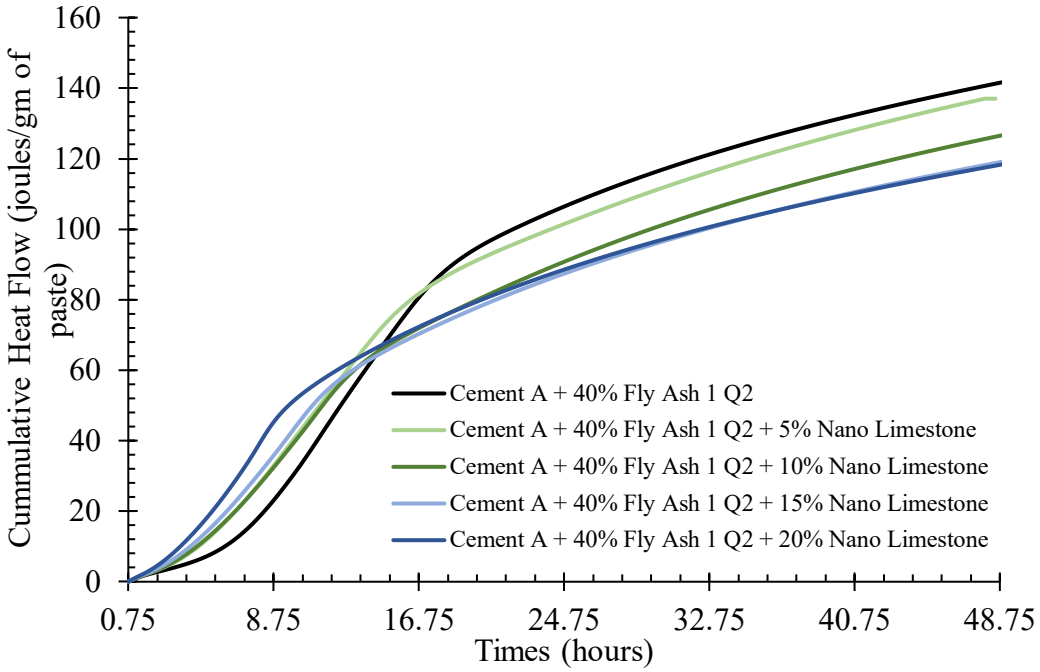

A. Fly Ash 1

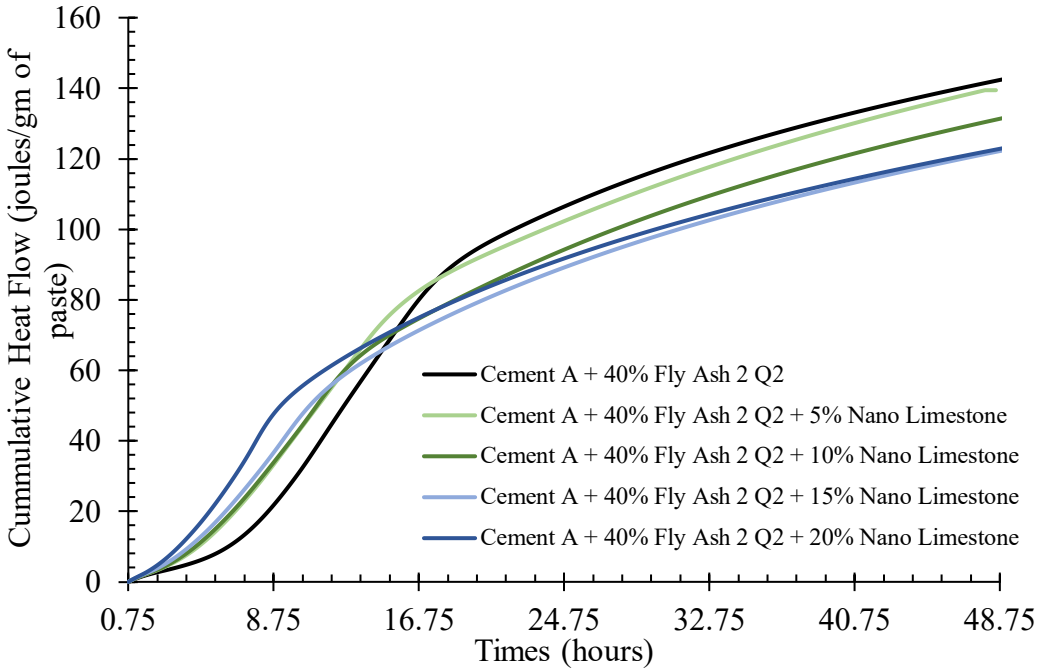

B. Fly Ash 2

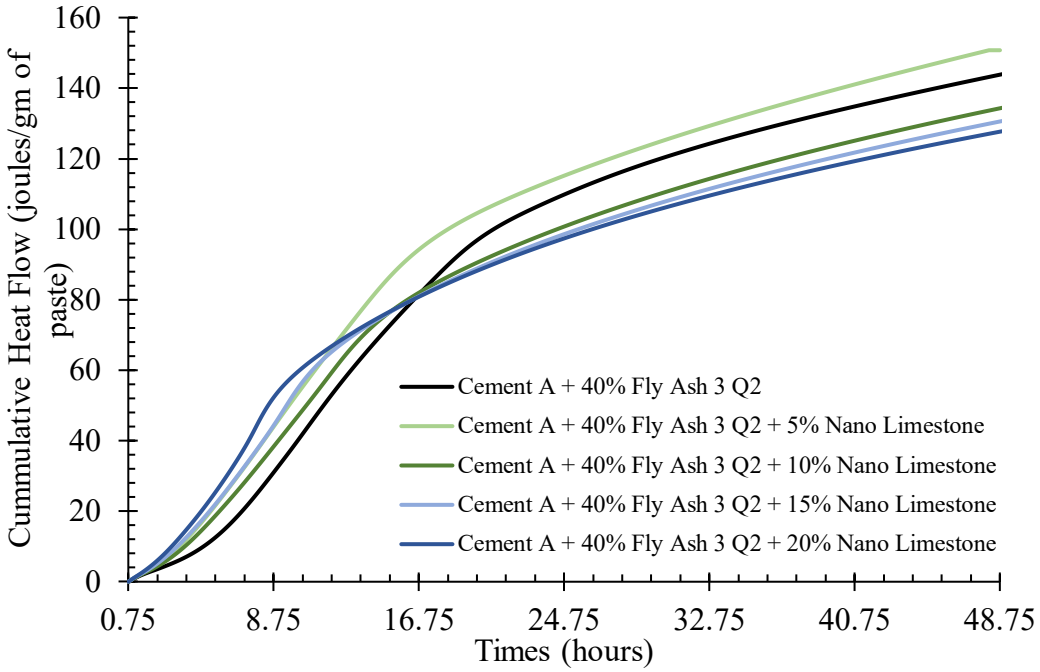

C. Fly Ash 3

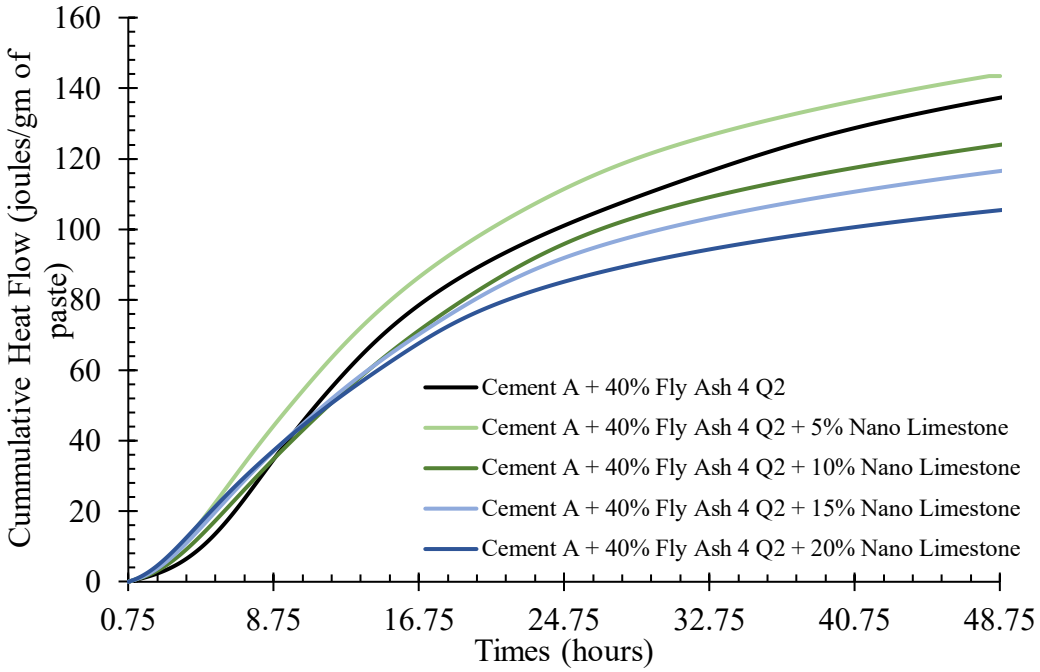

D. Fly Ash 4

Figure 50. Graphs. Effect of increasing nano-limestone replacement on cumulative heat flow for 40% weight replacement of cement with (a) Fly Ash 1, (b) Fly Ash 2, (c) Fly Ash 3, and (d) Fly Ash 4 for 2019 Quarter 2 samples.


Illinois Department
of Transportation


ILLINOIS